On the assessment of raking damage based on acceleration measurements

E.C. van Kempen

Technische universiteit Delft

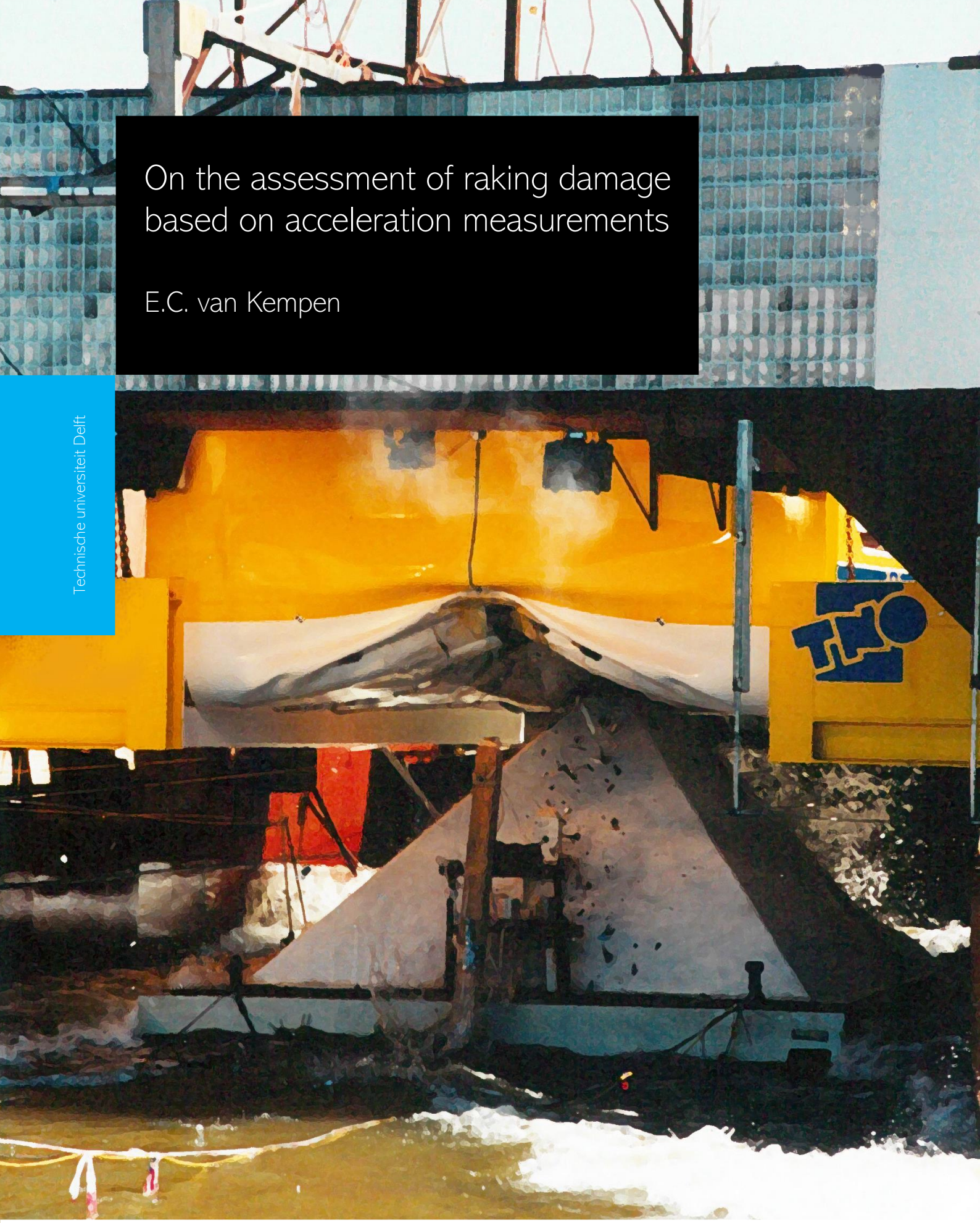

TU Delft

ON THE ASSESSMENT OF RAKING DAMAGE BASED ON ACCELERATION MEASUREMENTS

By

Elizabeth Charlotte van Kempen

in partial fulfilment of the requirements for the degree of

Master of Science
in Marine Technology

at the Delft University of Technology,
to be defended on Monday July 30, 2018.

Supervisor:	ir. M.G. Hoogeland	TNO
Thesis committee:	prof. dr. ir. M.L. Kaminski	TU Delft
	ir. R.W. Bos,	TU Delft
	dr. ir. P.T.L.M. van Woerkom	TU Delft

Preface

In front of you lies the thesis "*On the assessment of raking damage based on acceleration measurements*" by E.C. van Kempen. It has been written in partial fulfillment of the graduation requirements for the degree of Master of Science in Marine Technology at the TU Delft. The graduation project was realized in cooperation with the Structural Dynamics department at TNO.

First, I'd like to thank my supervisor at TNO, Martijn Hoogeland for the interesting graduation project and all his advice and help regarding the project. Secondly, I'd also like to thank both Mirek Kaminski, professor of Ship & Offshore Structures, and Reinier Bos, my daily supervisor at the TU. Both have given me inspiration in continuing the project and gave me a different view on how to approach the investigation. I also would like to thank Paul van Woerkom for his time and effort as a member of my thesis committee and also for the book he gave me.

Last but not least, I would like to express my thanks to a particular colleague of mine at TNO, Lex Vredeveldt, for providing me with the chance to write a paper together with Martijn and him and presenting it at the RINA Damaged Ships conference in London May 2018. He has given me advice, not only on the project itself, but also on how to approach other things. I'd also like to thank TNO for making attending the conference possible.

I am very glad I had such a great time in the last months of my study. I can count myself really lucky with the people I had the pleasure to work with and the environment I could work in.

Elizabeth C. van Kempen

Delft, July 2018

Abstract

In a grounding incident, it is important to be able to assess the severity of the situation. (Raking) damage caused by such an incident to the ship can have rupture of the hull as a consequence and subsequently this could mean flooding of compartments. Flooding of multiple compartments could threaten the ships damage stability and residual buoyancy. Short after such an incident, the officer of the watch is usually unable to assess the extent of the damage. Military ships have well-developed damage response procedures in place, where a well-trained crew, in the form of damage parties, is available to respond adequately. For non-navy ships, this is hardly possible, mostly due to crew restrictions. But even for navy vessels, underwater damage is hard to assess because of accessibility issues of flooded compartments.

This study is motivated by the following challenge: it is desired to be able to assess the damage on the bridge, without having to wait for damage reports (visual conformation of among other things the extent of the damage, flooding, loss of power, or non-visual indicators: loss of maneuverability, heel, etc.). Based on the outcome of this assessment, the officer in charge can decide whether to evacuate or to stay on board and control the situation. For establishing which compartments will flood the extent and the location of the raking damage must be known. It is proposed that the accelerations (or rather, decelerations) measured on board during a grounding incident can be used to make a prediction of the extent of raking damage. From the deceleration time-traces, the stopping distance of the ship can be calculated. Subsequently, in the case of a grounding on a rigid rock, this stopping distance could be used as a measure of the raking damage length. The study is performed in order to investigate the viability of this idea. In this thesis a study is performed in order to investigate the viability of this idea.

First, the hypothesis is tested by analysing the data (acceleration measurements, reported damage) from the TNO-ASIS large-scale grounding experiments carried out by a Dutch, German, Japanese consortium in ’94 and ‘95. This analysis shows how an acceleration signal can be related to the extent and severity of damage. After that, a three degree of freedom external dynamics grounding model for ship grounding has been made, which first uses rock location and a certain grounding force to predict the extent of bottom raking damage and associated decelerations of the ship in terms of surge, sway and yaw. This step is made first in order to validate the model. It is validated against data on ship grounding external dynamics from earlier research and data from the large-scale grounding experiment conducted by TNO-ASIS. After that, the step from accelerations to location and extent of bottom raking damage is made. The grounding simulation model is used in the opposite direction which results in an inverse calculation model. With this model, the location of the raking damage along the ship’s bottom can be calculated as well. Lastly, the model is tested with a sensitivity study.

From the validation of the external dynamics calculation model follows that the model works satisfactorily. The results of the models are that the accelerations can be used to calculate damage paths along the ship bottom. The findings of the sensitivity study of the method predicting the rock-bottom contact path are that the inertia ratios have a large influence on the predicted rock contact path in transverse direction. Also, the ratio between the measured decelerations have a large effect on the predicted damage path. The analysis of the measured accelerations from the large-scale experiment shows that acceleration time-traces indicate magnitude of deformation of the structure and time and location of rupture, giving insight into the severity of the damage.

The findings support the viability of the proposed idea: accelerations can be used to assess the raking damage. The study can be used for a calculation tool on board, which can help make an assessment of the situation just after grounding for the crew on the bridge.

Nomenclature

Symbols

A	Cross-sectional area (m^2)
A_{xx}	Added mass in surge
A_{yy}	Added mass in sway
$A_{\psi\psi}$	Added mass in yaw
E	Energy [J]
E	Young's modulus (GPa)
f	Frequency (Hz)
g	Gravitational constant ($m\ s^{-2}$)
I_{zz}	Ship moment of inertia plus added mass around vertical axis
k	Stiffness of load cell ($N\ m^{-1}$)
Kts	Knots [$nm\ h^{-1}$]
M	Ship displacement
M_{xx}	Ship mass plus added mass in surge
M_{yy}	Ship mass plus added mass in sway
μ	Rock eccentricity from centre line (m)
t	tonnes
ψ	Yaw (degrees)

Abbreviations

APP	Aft perpendiculars
CL	Centre line
CoG	Centre of gravity
CWT	Continuous wavelet transform
DoF	Degrees of freedom
FEA	Finite element analysis
FEM	Finite element method
FFT	Fast Fourier transform
FPOI	First Point of Impact
FPP	Forward perpendiculars
LCB	Longitudinal centre of buoyancy
LCG	Longitudinal centre of gravity
LNG	Liquified natural gas
PP	Perpendiculars
PS	Portside
SB	Starboard
SOLAS	International Convention for the Safety of Life at Sea
SW	South-west
VLCC	Very large crude carrier

Contents

1

Introduction

The grounding of MV Benita. June 17 2016. Mahebourg, Mauritius

1.1. Motivation

When a grounding incident occurs, the officer of the watch is usually unable to assess the severity of the damage. Military ships have well developed damage response procedures in place where a well-trained crew, in the form of damage parties, is available to respond adequately. For non-navy ships, this is hardly possible, mostly due to crew restrictions. But even for navy vessels, underwater damage is hard to assess because of accessibility issues of flooded compartments. This is undesirable because it needs to be known which compartments have flooded in order to assess the situation with respect to residual buoyancy and stability of the ship. Based on the outcome, the officer in charge can decide whether to evacuate or to stay on board and control the situation. In the case of the Costa Concordia grounding incident, this decision was made too late. Damage reports by non-well trained (hotel function trained) and non-Italian speaking crewmembers did not help in the quick assessment of the severity of the situation. The method proposed in this study is intended as an aid on the bridge for the assessment of the severity of the situation after a grounding incident, even before any damage reports have come in.

For establishing which compartments will flood the extent and location of raking damage must be known. It is proposed that the accelerations (or rather, decelerations) measured on board during a grounding incident can be used to make a prediction of the extent of raking damage. From the deceleration time-traces, the stopping distance of the ship can be calculated. Subsequently, in the case of a grounding on a rigid rock, this stopping distance could be used as a measure of the raking damage length. The method does not rely on elaborate internal mechanics calculations, which makes detailed knowledge of the ship structure necessary. Instead, the method only makes use of the decelerations measured on board during a grounding incident. Measuring ship motions with the use of accelerometers is not expensive. Nowadays, accelerometers are even used in smartphones. This means that in the most simplest of ways, the method could therefore already be applied with the use of an app on your smartphone, albeit that measurement accuracy with such a device may prove insufficient.

1.2. Research framework

The goal of the study is to investigate the viability of using only deceleration measurements to make a prediction of the raking damage extent. The study is given a stable framework by proposing a main research question and a couple of sub-questions.

Can the extent of the raking damage be assessed using the deceleration time-traces measured during a grounding incident?

Sub Q1: How can acceleration time-traces be related to damage?

Sub Q2: What is the damage path resulting from grounding force?

Sub Q3: Can the rock bottom contact path be derived using only accelerations?

The extent of the raking damage is made up of the magnitude of the damage (how the local ship structure is affected by the grounding) and the location of the damage (how the grounding affects the ship globally: the same damage in different areas can have different consequences for the ship). The first sub-question investigates this first aspect of the raking damage

extent. The question is formulated as to get a grip on how these acceleration time-traces measured on board look like in case of a certain magnitude of raking damage. It investigates in what sense accelerations and grounding damage relate through the analysis of data from the large-scale grounding experiment carried out by a Dutch, German and Japanese consortium [1].

After these accelerations are analyzed, a method is made to calculate how this information can predict the location and size of the raking damage, thus answering the main question. The method would only need to work with the least information possible, because just after grounding the location and the size of the rock is not known. The input of the model would only need to be the accelerations and the ship's main particulars. But this is too difficult to do in one step. Therefore, the goal of the second sub-question is to first simplify this problem. This is done by assuming that the size and location of the rock is known. This means that the forces acting on the ship at the location of the rock is known together with the location of the rock with respect to the ship. The second sub-question is: 'What is the damage path resulting from grounding force?' To answer this question, a three degrees of freedom (DoF) external dynamics grounding model is implemented. In this model, a certain first point of impact between the ship bottom and the rock is used to simulate the acceleration, velocity and displacement of the ship and by doing so acquiring the rock contact path along the ship bottom. This will serve as the base of the whole grounding damage calculation model.

After that, the step from grounding forces to accelerations is made. The assumption from earlier (knowing the location of the impact with the rock and the forces acting on the ship by the rock) must be forgotten, because in a grounding incident nor the shape/size of the rock nor the location of the impact with the rock is known. The only thing at ones disposal is the acceleration signal measured on board. This challenge results in the third and last sub-question: "Can the rock bottom contact path be derived using only accelerations?" For this approach the three DoF calculation model is expanded by reverse engineering the method. With this inverse method the damage path along the ship bottom is calculated using acceleration time-traces.

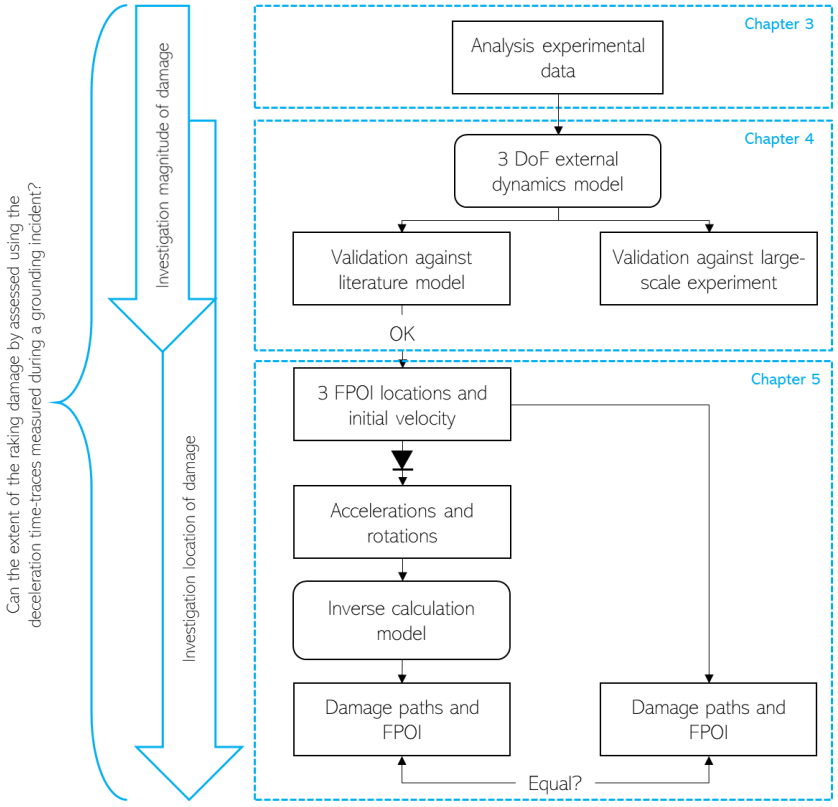

Figure 1 Flowchart visualizing the framework of the study

The discussed framework of the thesis is visualized in the flowchart in Figure 1. The investigation to answer the main question is divided in two: the investigation of the magnitude of the raking damage and the investigation of the location of the raking damage. This is depicted as the two vertical arrows showing which part of the investigation concerns what. First, the accelerations from the large-scale experiment are analyzed to give more insight in how accelerations can be related to raking damage extent. This is done in Chapter 3. The second entry shows the implementation of the three DoF calculation model. This is described in Chapter 4. The model is validated against a model from literature [2] which uses an example with a VLCC and also against the large-scale grounding experiment. This will make sure that the model is a good basis to work with for the next part of the investigation. After the validation, the example of the VLCC will be used to perform a case study. Here the behavior of the damage path when varying the grounding scenarios is looked at. The validated model will be used to simulate grounding scenarios and acquire the accelerations. The diode is used to show that the source of the accelerations is not known in the next step: some random accelerations are looked at (source unknown) as to predict only from this data the damage paths and location of this damage path on the ship bottom. These damage paths resulting from the inverse calculation model are compared to the original damage paths. This is done in Chapter 5. The investigation is concluded with a discussion and conclusions in Chapter 6.

1.3. Background information

1.3.1. Raking damage

Ship grounding damage can be categorized in two cases, as pictured in Figure 2. The first is the case where the ship is prominently vertically loaded, due to tide or heave in shallow waters with rough seabed topology. The second is the case where the ship is prominently loaded in the direction the ship is moving (raking). This thesis focusses on the last type. Also, the thesis focusses on ship bottom damage instead of side damages. Bottom damage is defined as damage with primarily vertical penetration direction [3]. The bottom of a ship is the most vulnerable/prone to raking damage, because it's the closest to the seabed. Studies and regulations on the topic of grounding damage have been instigated by past grounding incidents. When observing a double bottom/hull ship, it is very important to know if both the outer and inner hull is breached when damaged. Double bottom height regulations by SOLAS, such as presented in Table 1, for passenger and cargo vessels provide a standard level of safety in case of grounding [3]. This table, for example, describes the required minimum double bottom height of passenger ships and cargo ships other than tankers. This minimum double bottom height is regulated as to ensure safety against, for example, consequences from a grounding damage [3]. Studies, as will be discussed in Chapter 2, provide new insights to come up with a new standard level of safety in case of grounding. But in case a grounding incident does happen, the watertight compartment zones ensure that if a compartment is flooded the ship cannot sink by just the flooding of one compartment. The design of the watertight compartment zones are even safer on board of passenger ships. These are designed such that two adjacent compartments can be flooded before the vessel may sink.

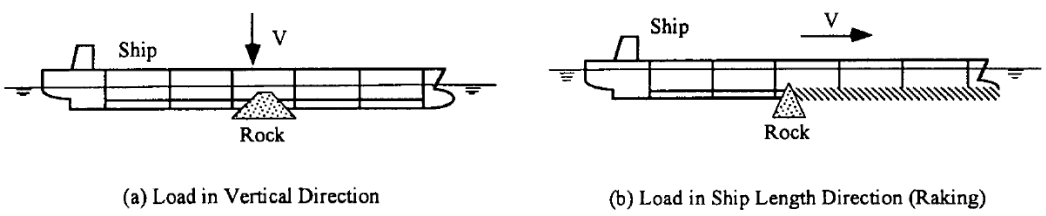

Figure 2 Grounding types (Fig. 1 in [4])

Table 1 Minimum height of double bottom – SOLAS Ch.II-1, Part B-2, Regulation 9. [3]

Required standard minimum double bottom height (h)
$h = \frac{B}{20}$ (where B is the ship breadth) In no case is the value of h to be less than 760 mm, and need not be taken as more than 2 000 mm
In case of large lower holds in passenger ships, the Administration may require an increased double bottom height of not more than B/10 or 3 m, whichever is less, measured from the keel line. Alternatively, bottom damages may be calculated for these areas, in accordance with paragraph 8 [of Reg.9, i.e. *damage characteristics to be taken into account for alternative calculations in case of unusual bottom arrangements in a passenger ship or a cargo ship*], but assuming an increased vertical extent.

1.3.2. Present damage assessment

In order to point out the attractiveness of implementing a model which is able to assess the raking damage extent with the use of acceleration data only, the current assessment of the damage during a grounding event will be discussed. This is explained by using the grounding accident of the Costa Concordia, at Giglio island, Italy, as an example. The ship fell victim to a total of two grounding events in a short time. The first event happened at high speed (16 kts) south of the harbor of Giglio, resulting in the damage seen in Figure 3 and Figure 4. The second happened after drifting away on the current and wind, after experiencing a loss of propulsion and maneuverability by the first event. Finally, the ship came to a complete standstill during the second grounding and heeled over to its starboard side until a heel angle of 80°. [5]

In chronological order of events, the assessment of the situation is listed. Indicators of raking damage and the actions undertaken are marked in bold lettering.

First grounding

The crew realized that something very serious had happened. The ship **violently heeled** and the **speed immediately decreased**. The crew gave a warning that the left side has gone aground and report to have **heard a loud crash.**

The grounding results in the **immediate loss of propulsion** and the ship was consequently effected by a **black-out**. All the **officers are ordered to go to the bridge**. The **rudder was blocked** to remain in starboard position and could no longer be handled. **Alarms** started for rudder failure, propulsion failure and the balancing system of the ship.

Moments after the first grounding

Assessment of the damage was continued by the **crew. They go to the lower decks** and found that, after only six minutes after the impact, there is **water in two adjacent compartments** which affects the workshop, the engine room, the main switchboard and the emergency switchboard. The flooding of these two compartments already represented the limit condition for stability for the purpose of safe abandon ship. At this point in time the ship lists to portside.

The ship is equipped with trim and stability software called "NAPA" approved by the Italian Naval Register (RINA). It is not working at this point in time and the crew tries to re-activate it. This is crucial, for the software is able to rapidly model various types of damages and progressive flooding in case of damage and can simultaneously do an analysis of recovery strategies. The software also gives decision support and flooding control (time to flood/sink) on board [6].

Alert phase

The captain has **first telephone contact with the company** (Costa Crociere) and **reports to the Fleet Crisis Coordinator** that the ship hit a rock at the port side towards the stern. There is no distress signal given because the **Global Maritime Distress and Safety System (GMDSS)** was not activated immediately after the impact. This system incorporates satellite systems to ensure that no matter the ship's position in distress, assistance can be sent globally [7].

Drifting of ship and second grounding

The NAPA is running again, however, not constant. The ship is practically motionless (0.3 knots), but begins to drift. The bow shifts to starboard, heading SW because of the combined influence of wind and the rudder (which is stuck in the position all the way to starboard). The **list goes from port to starboard side,** this due to the flooding of more adjacent compartments. This resulted in a huge free liquid surface, because some compartments had few machines that could break the continuity of the liquid surface. This affected the conditions of residual stability of the hull. The **free liquids surfaces**, therefore, had determined the first prominent heel to starboard.

Alert phase

Sometime during the inspection by the crew, the 1st Deck Officer and the Deputy Chief continue the **inspection of the watertight compartments**. They verify that there is a leakage of water from a water-tight door and also deduce that now four adjacent compartments are flooded (compartments 4, 5, 6 and 7). The ship, in accordance with SOLAS requirements, can withstand flooding of two adjacent main compartments.

Uncertainty phase

The uncertainty phase starts on account of the local coast guard, because they were not convinced the situation was under control. This uncertainty phase is according to standard procedures.

Distress phase

The ship was taking even more water and **started listing even more**. This was an **indication of rupture and water ingress** for the local coast guard. The list of the ship increased over time. At this moment the abandon ship order was given.

Evacuation

At about 24:00 the **list of the vessel seriously increased reaching a value of 40°.** During the **rescue operations it reached a final 80°.**

Figure 3 Damage to the hull

Summarizing, the first indicators of raking damage was the large deceleration that was felt by the people on board. Other indicators of the extent of the damage are sound (from the crash) and light, or actually the lack of it after lights went out, for the grounding happened at dusk. This black-out (and also the loss of propulsion) were the consequence of failing machinery and systems. This serves as an indication of flooding of compartments containing this machinery and systems and thus indicating breaching of the hull. The next determination of the damage is done both visually, by having a look in the part of the ship where impact took place and consulting the stability and safety programs on board: check up on system warnings. In this case, warnings indicated that there was a complete loss of propulsion and maneuverability. Some pumps and other auxiliary equipment were also lost due to the flooding of compartments. Also, the heel of the ship is an indication of water intake and therefore rupture.

Extent of the damage

The impact with the rock led to the release of 215 MJ of kinetic energy (equivalent to 250 Tons of thrust) due to the ship's 56,600 tons weight and speed of over 16 knots. The stern also experienced an advancement towards portside due to the sudden turn to starboard (ordered 22 seconds before impact). This has resulted in a disruptive contact with the rock, which weakened the side and tore it due to the ship's movement (tear is visible in Figure 3). The speed was almost halved, from 16 to 8.3 kts. The hole on the left side stretches over 60 m and is located too far above the double bottom (over 2 m above the keel line). This was crucial in terms of the severity of the accident, because rather than creating a rupture in the bottom structure the rock ruptured the compartments above the double bottom directly. This led to the flooding of two watertight compartments in just minutes. Adjacent watertight compartments were initially partially flooded, becoming dangerous free liquid water surfaces and then completely flooded after about 40 minutes from impact. [5] Figure 4 gives an overview of the flooded compartments.

In reference, the high energy impact test during the TNO-ASIS large-scale grounding experiments dissipated around 5 MJ and came to a complete stop afterwards. The mass involved, however, was around 100 times less and at around half the speed of the Costa Concordia's before the grounding. Also, the damage length in the case of the experiment is around 10 times shorter than that of the accident.

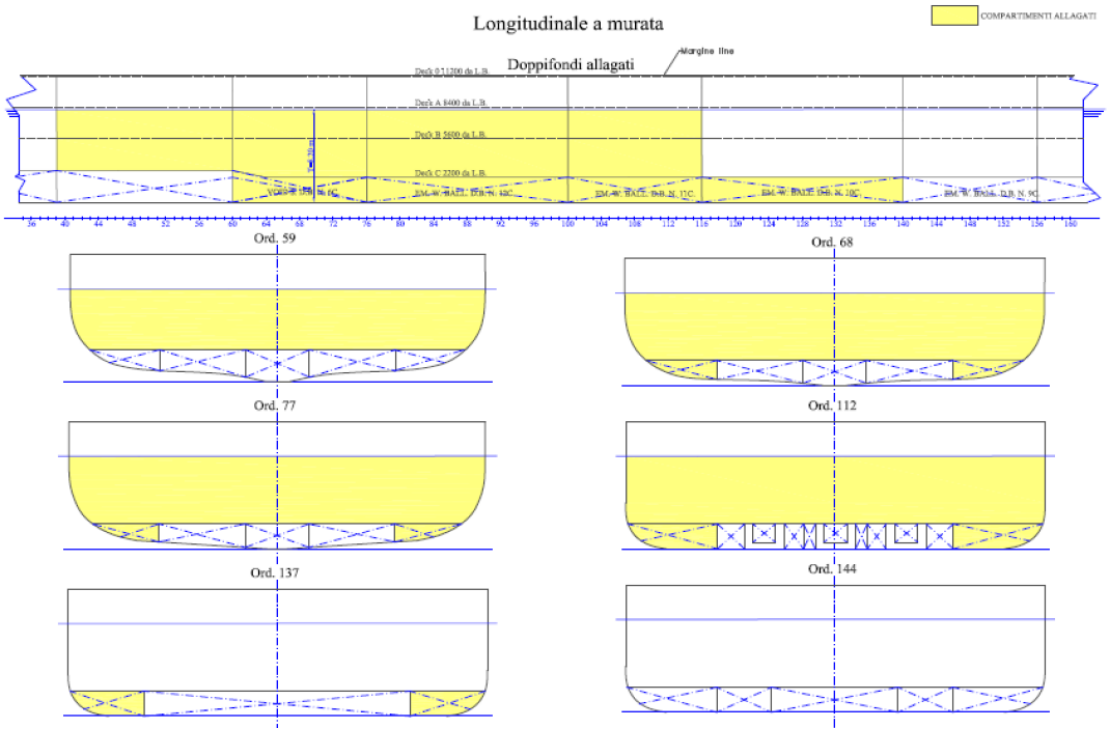

Figure 4 Flooding of compartments. Yellow represent flooded compartments and side double bottoms. From p. 105 [5].

2

Literature study

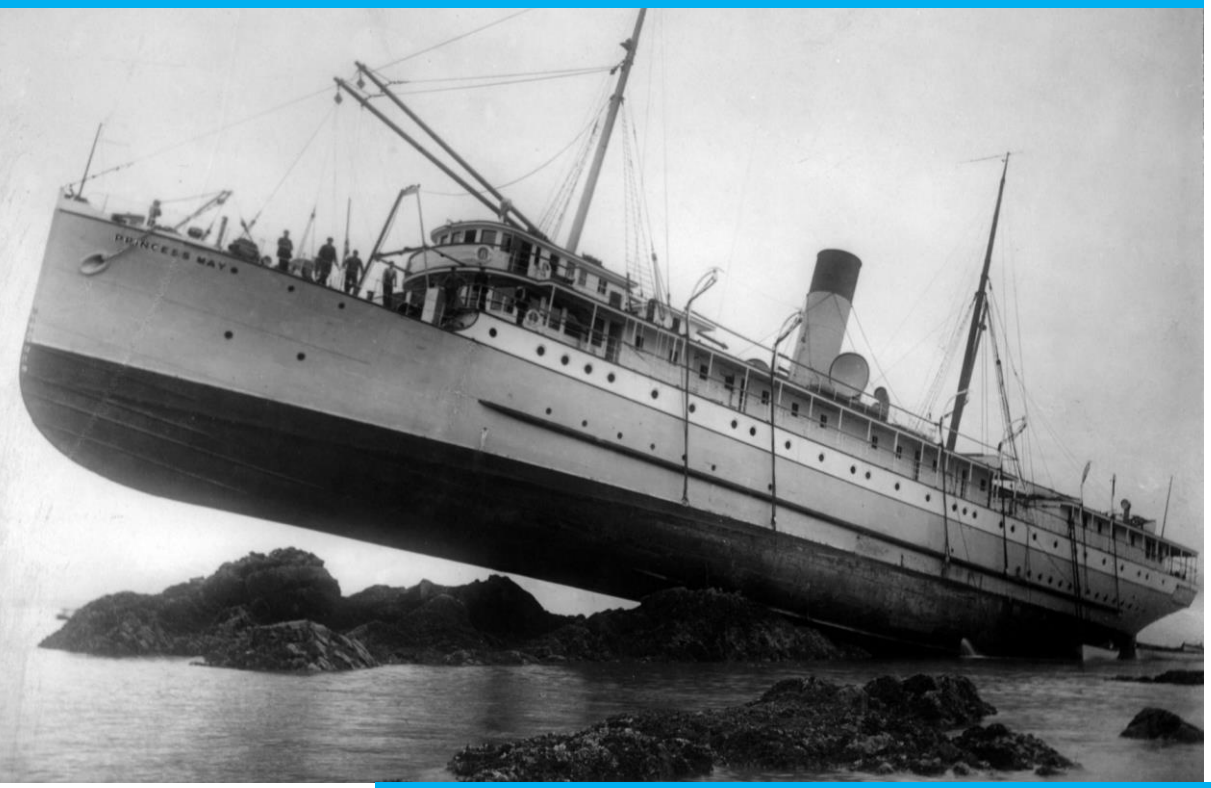

The grounding of the Princess May. August 5, 1910. Sentinel Island, Alaska.

2.1. Introduction

In order to get a better view of research performed on ship grounding and collision, a review of experiments and a literature study have been done. For this thesis is searched for literature which focusses on certain topics which fall under ship grounding. These are most importantly on the topic of external dynamics. This part of the problem of ship grounding takes into account how the ship behaves under a certain grounding load as a whole. Ship motions under a certain load plays an important role in the determination of both the magnitude and location of the raking damage. A study on this topic will also make clear as to what other grounding models have been made already. In order to investigate the magnitude of the raking damage and to get to know more about the energy dissipation mechanisms in ship grounding, a study on the topic of the external mechanics part of ship grounding is performed as well. This part of the problem of ship grounding is explained by how the local structure responds to a certain grounding load. Experiments are found which combine the two parts of the problem of ship grounding. Summarizing, the literature study is divided into three topics: internal mechanics, external dynamics and analytical models. The parts in the literature which serves the most useful for this thesis have been summarized.

It is important to note that studies performed on the topic of ship grounding and collision may be performed with a different goal:

1. **Prevention** - First, one can investigate a certain problem in order to make sure that this problem will never have to occur again. Of course, ship accidents will keep happening due to weather, technological and human errors, etc.
2. **Accident resistant design** - But some studies investigate ship grounding in order to make sure this knowledge can be used next time in the design phase of ships. This way they mean to serve the goal that the next time an accident happens, the consequences are smaller.
3. **Post-process** - Another type of goal could be not to prevent, but to post-process. The goal of the study is to learn from an incident. The next time such an incident occurs, it is known what exactly happened.
4. **Predict** - The last goal, and also the goal of this thesis, is to predict: if something does go wrong, how can be made sure that the consequences are understood and it is known how to act in such a situation.

Because of this each of the studies discussed in this chapter is categorized in not only *how* the study was performed and *what* they found, but also *why* they performed the study. The *why* for each study is indicated by one of the four points in the list above. This is done, because research with a shared goal with this thesis are interesting for the investigation.

2.2. Large-scale experiments

All different kinds of small-scale experiments have been performed on the topic of ship grounding and collision, but only a small number of large-scale experiments. Even though scaling laws should ideally be avoided on this topic, for they don't have good agreement, small-scale experiments are favoured among researchers due to lower cost and reproducibility. But for this study it is important to look at how both the local and global structure behaves on impact and which accelerations are the response of this. Next, a short description of two large-scale experiments is given.

2.2.1. TNO-ASIS large-scale experiment

How In 1994 and 1995 a series of tests were carried out by a Dutch, German, Japanese consortium [8]. Tests were performed using a 600 t inland waterway ship with a double bottom test-section mounted between its H-shaped

hull. The test-section was run into a rigid artificial rock mounted on a submerged pontoon (Figure 5). The double hull test-sections were 1:4 scale with respect to VLCC's, for coastal and inland shipping the scale is 1:1. All motions in six degrees of freedom were considered and measured using gyros and accelerometers. A couple of tests were carried out. Some tests represented light energy and others high energy grounding scenarios. In the high energy grounding tests also the inner shell was ruptured. A lot of data was acquired from these tests, such as the forces of the rock on the ship, the accelerations of the ship and the strains on all kinds of locations throughout the test-section were measured in time. Figure 5 shows the experimental set-up. Figure 6 shows the ship and test-section for one test just before and just after the grounding. An elaborate photographic overview of the test can be found in Appendix A. Appendix B shows the measurement equipment on board and Appendix C gives some general information on the support ship and test-section: dimensions, masses, etc.

Why This experiment was performed on **accident resistant design**. The motivation for large-scale testing was because of the interest in prevention of outflow of hazardous cargo. Another reason for interest is the validation of damage prediction calculations using FEA, which became more available during that time. There was a main interest in the crash behaviour of the test-sections (extent of damage, if inner hull was rupture).

What The experiment was reproduced using FEA, in order to calculate the grounding forces by the rock on the ship and try to understand what energy dissipation mechanisms occur during the grounding. Of the total energy dissipation around 50% of the initial energy is dissipated by membrane deformation, ±30% by in-plane stress shear deformation and ±15% by bending deformation. The vertical motion was restrained in the FEA model, which resulted in a larger force than was actually measured during the experiment. This is because in reality the ship was able to pitch and heave.

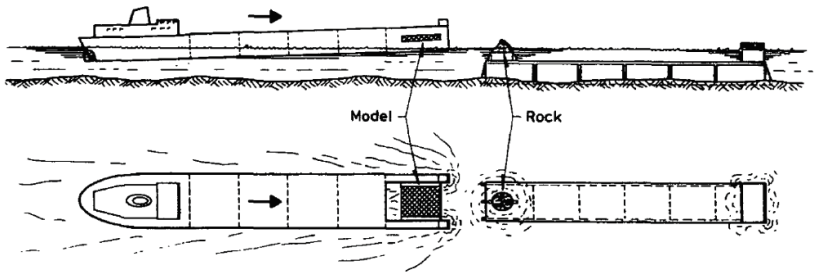

Figure 5 Experimental set-up of the TNO-ASIS large-scale grounding experiment

Figure 6 Left: just before grounding, approaching the rock at approximately 7 kts. Right: Just after grounding. Rock stuck in buffer.

2.2.2. NSWC double hull grounding experiments

How Large scale experiments were conducted by the Carderock Division of the Naval Surface Warfare Centre (NSWC) in the united states [9], [10]. A test-section of the bottom structure of an oil tanker with scale 1:5 was mounted on top of a sled. Multiple tests were performed using different double bottom sections with different types of bulkheads. The sled rolled down a rail which made the test-section collide with a rock (Figure 7). Using high speed cameras the failure mechanisms which can lead to the rupture of the inner shell was studied.

Why This experiment was performed on **accident resistant design.** The experiments were motivated because of the growing concern of oil and hazardous cargo spills resulting from tanker hull rupture during grounding and stranding accidents. The overall objective was to understand the structural failure mechanisms associated with grounding events for double hull structures. Their goal is to come up with a tanker design with enhanced crashworthiness in grounding events to **prevent** hazardous cargo spills.

What In the experiment the focus was on initiation of inner shell rupture and structural failure mechanisms which precipitate the rupture. Therefore high speed photography was used to capture detailed failure mechanisms leading to inner shell rupture initiation. It is seen that at smaller scale, there is less tearing damage. Tearing damage does not scale by a relationship compatible with the distortion from bending, buckling and crushing.

Kinetic energy was mainly dissipated through the crushing and tearing of the hull structure and deformation of the outer and inner shell. Forces in vertical and longitudinal direction were measured. The rock force in longitudinal direction is plotted against the rock's longitudinal penetration in Figure 8. This transverse frame tearing pattern is repeated at every frame (the smaller peaks in the plot) and is even more obvious for the two bulkheads. The force signal rapidly decreases to zero after rupture occurred in the aft tank (after first transverse bulkhead).

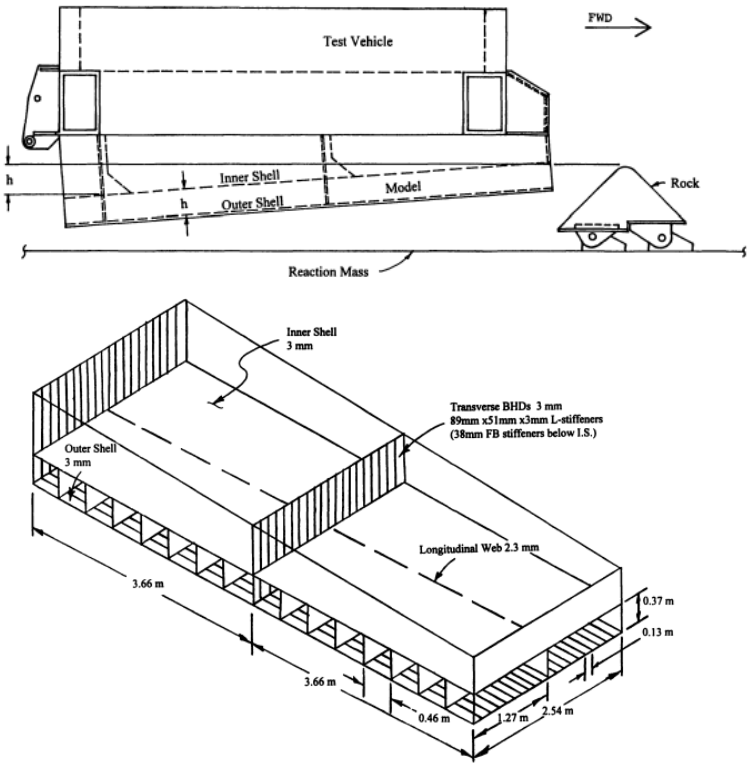

Figure 7 Model installation and 3D-view of the conventional double bottom test-section [10]

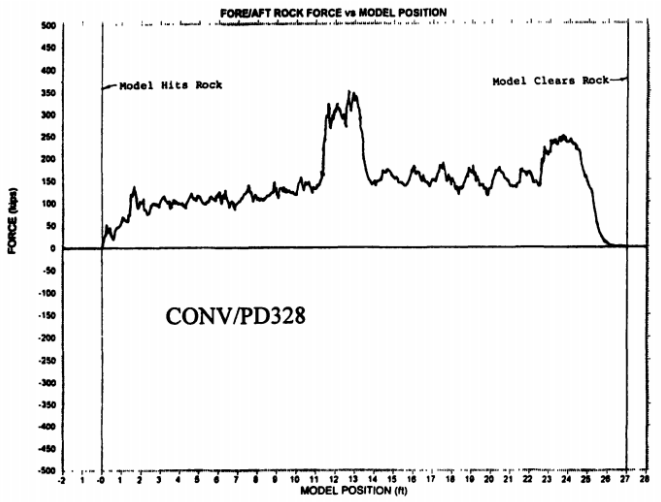

Figure 8 Horizontal force - displacement plot for the conventional double bottom test-section test [10]

2.3. Review of literature

The literature study is divided into three topics: internal mechanics, external dynamics and analytical models. But first, the first two topics, internal mechanics and external dynamics, are explained. This can be done most properly by reviewing the explanation given by Minorsky, in the following paper.

Minorsky, 1959 – 'An analysis of ship collision with reference to protection of nuclear power ships.' [11]
Minorsky divides the analysis of a ship grounding or collision into two parts: the internal mechanics and the external dynamics. Many researchers have copied this approach as to simplify the problem of ship grounding and collision. Figure 9 visualizes this division. The internal mechanics part evaluates the deformations the structure undergoes while absorbing energy from a certain impact. The external dynamics part deal with the ship motions which are the response of the impact. Minorsky has observed through data of accidents that the dissipated energy is proportional to the volume of the damaged material. He proposed an empirical formula to describe this relation. The simplicity of this method has attracted much attention through the years.

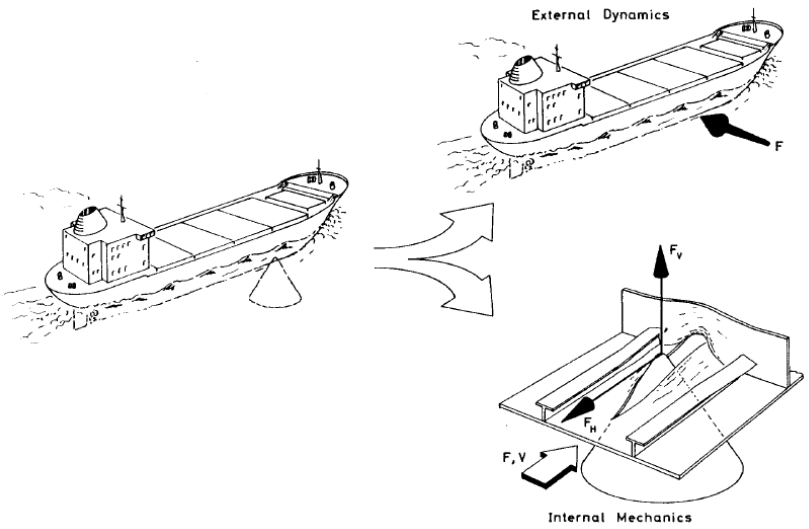

Figure 9 Dividing the problem of analysing ship grounding into the external dynamics and internal mechanics (Fig. 6.1 in [2])

2.3.1. Internal mechanics

The research on this topic mostly focusses on energy dissipation mechanisms: deformation, fracture and frictional effects on the structure's surface. Also, it deals with the size of the damage: width and length of the damage and vertical penetration of the rock. In Simonsen & Wierzbicki a good basic theory of the internal mechanics is given [12]. It is stated that the grounding problem is looked at as an external load (rigid rock) applied on a deformable structure (ship bottom). For a rigid-plastic ship structure no elastic energy can be stored so that the work of the external loads must equal the rate of energy dissipated by plastic deformation in the form of the energy dissipation mechanisms mentioned earlier. This is

$$F \cdot V = \dot{E}_p + \dot{E}_f = F_P \cdot V + \int_S p\mu V_{rel}\, dS$$

F = resistance force of the structure in direction of V [N]
V = relative velocity between ship and rock [m s^{-1}]
$\dot{E}_p$ = rate of plastic energy dissipation [J s^{-1}]
$\dot{E}_f$ = rate of energy dissipated by frictional forces on the structure's surface [J s^{-1}]
F_P = plastic resistance
μ = friction coefficient
p = normal pressure on the rock at the plate element dS
S = contact area between rock and plate
V_{rel} = relative velocity between rock and plate element dS

The rate of internal energy dissipation for a deformed plate with area S, $\dot{E}_p$, can be calculated by adding the rates of membrane energy dissipation to the bending energy dissipation. From the basic internal mechanics theory, they have derived the resistance force for the main structural members: shell plating, longitudinal members (T-stiffeners, girders and bulkheads) and transverse members (frames, floors and bulkheads). With this, they study plate deformation before fracture.

Simonsen, 1998 - Ship grounding on rock – I. Theory [13]

How The study presents analytical expressions which can be used to calculate horizontal and vertical reaction forces on a ship bottom by a conical rock. The model searches for a realistic deformation mode and can also be used to predict fracture. This can then be combined with an external mechanics model (see section 2.2.3) to calculate ship motions and damage in a given grounding scenario.

Why The purpose of the study is to present a simplified theoretical model which can predict the reaction force of an assembled ship bottom structure deformed by a conical rock with a rounded tip. The study was performed on **prediction** and **accident resistant design**. The latter because these damage prediction models can be used to model damage in an early design stage as well. It has been stated that many of the past improvements in safety of marine structure have been triggered by disasters. Examples are the grounding of the Exxon Valdez and the Estonia, which respectively caused the requirements for double hulls and reformulations of requirements for ferry design and operation.

What The average length of the deformation zone in the outer bottom is found to be about the same size as the transverse frame spacing (from the Exxon Valdez). This is for the longitudinal extent of the deformation. For the transverse extent of the deformation it is assumed that longitudinal members to the side of the rock are not deformed before they are directly pushed by the rock. After fracture, the width of the deformation is simply equal to the base of the

rock in the plane of the undeformed plating. The extent of the deformation of the inner bottom is more complex, because it is deformed by floors and girders even before the rock tip touches the plating. It is important to find when both the outer and the inner bottom shell is fractured. This due to the risk on oil spill, such as in the case of the Exxon Valdez. That is why there is a focus, not only of the deformation of the plating around the rock tip, but also when the plate is eventually fractured.

Simonsen, 1998 – "Ship grounding on rock – II. Validation and Application" [14]

How The theoretical model from part I is validated against the large-scale grounding tests performed by the NSWC. The model indicates that a large amount of energy dissipates by friction. But although the model can predict the total dissipated energy well, the energy distribution between plasticity and friction is found not to be very accurate. The primary deformation mode is as predicted by the theory. Also, the theory is validated against a real grounding accident. With this, also the external dynamics are considered. The damage length of the real accident is obtained from the theory when a rock penetration of 4.4 m is applied, which agrees well with the actual rock penetration of 5 m. Even though the shape of the rock was uncertain, there is very good agreement between the extent of the actual damage and the calculated damage.

Why Simonsen proposes that the theory can be used for a probabilistic damage assessment, which serves as **prediction** of damage. For the sake of **ship design**, it is needed to evaluate a range of impact scenarios. Using probability density functions (pdfs) of the input parameters in the proposed theory, one can arrive at the pdfs for the damage. The uncertainty of the grounding problem is primarily related to the overall impact properties, such as rock size, shape, position relative to the ship and ship draught, speed and trim.

What Simonsen shows the importance of including the external dynamics. The damage length increases when the ship is free to heave, roll and pitch. Because of the pitch motion the rock penetration is smaller and the ship needs a larger stopping distance to dissipate all the initial energy in longitudinal direction. If the ship was locked in a horizontal surge motion without heave, roll or pitch, its kinetic energy would have dissipated earlier and the damage length would be smaller. On the other hand, when the offset of the rock from centre line becomes larger, the damage length is increased by about 70%.

Alsos, Amdahl & Hopperstad, 2009 – "On the resistance to penetration of stiffened plates" [15]

How The paper focuses on the ship's structural failure mechanisms in stranding. Stranding is a different type of grounding. In stranding it is assumed that the ship settles on the sea floor without being subjected to sway or surge motions. Damage of the hull is a consequence of receding tides and wave loads. The authors prefer a small-scale test for their research instead of a large-scale test, because these are costly and are performed dynamically. Panel indentation experiments are carried out, as to model a ship's local bottom structure being loaded by the seabed. They test an unstiffened panel and a series of stiffened panels.

Why With their research they try to get a better understanding on failure mechanisms in stranding. They **post-process** in order to get a better understanding in case an incident happens again.

What From the results of these panel indentation tests, they conclude that an increase in the number of stiffeners and/or adding stronger stiffeners, yields reduced flexibility and early fracture. In ship design, in order to keep deformations small, stiff structures are generally wanted. But in accident resistant design, a more ductile design with high energy dissipation capability may be preferable. Also, they view that in all cases the fracture first occurs next to the stiffeners, but never in the welds themselves.

Heinvee & Tabri, 2015 – "A simplified method to predict grounding damage of double bottom tankers" [16]

How The paper presents analytical formulas for the calculation of damage opening sizes in tanker groundings. They propose that the longitudinal damage length depends on the average contact force and the kinetic energy of the ship. These analytical formulas are derived from a numerical study. They perform numerical simulations with models of tankers with different dimensions. These tankers are run into different sizes of rock at different penetration depths.

Why The analytical formulas can be used to **predict**, but for the approach knowledge of the size of the rock is necessary. For a prediction purpose, a rock size must be assumed. The approach is therefore more suitable to be used in **post-processing** of a grounding scenario. The approach is also very useful in analyses where not much information regarding the detailed ship structure is available.

What The damage opening widths in outer and inner bottom were derived from relative rock sizes, which have a strong influence on the deformation mode and magnitude of deformation. Figure 10 shows that the damage widths are a function of rock size, penetration depth and double bottom height. For the case of a small rock, type a, the fracture at low penetration depth is due to the very local contact of the rock tip (causing high strain concentrations in the structure). The dominating deformation mode found for this case is local tearing. The damage width in the outer plating increases nearly proportionally with the penetration depth. For a larger rock, type c, the dominating deformation mode is global crushing of the plating. The plating is torn open only for larger penetration depths. They conclude that as rock size increases, the ship structure has a gradually larger impact on the type of deformation mode.

The approach describes horizontal grounding force and damage opening and length satisfactorily above a penetration depth of 0.5 m. For smaller penetration depths the approach should be developed more.

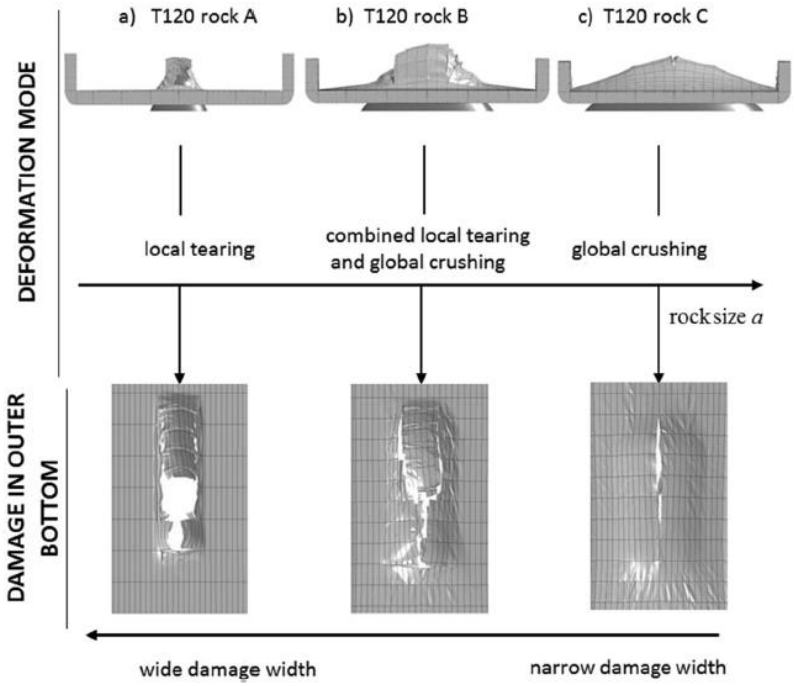

Figure 10 Dominating deformation modes depending on the rock size: a) local tearing; b) combined tearing and crushing; c) global crushing mode. (p. 31 Heinvee & Tabri [16])

Simonsen, Törnqvist & Lützen, 2009 – "A simplified grounding damage prediction method and its application in modern damage stability requirements" [17]

How They present a simplified grounding damage formula for the raking force as a function of the bottom structure and the size of the rock for typical ships. They analyze the grounding damage statistics of ships in order to determine impact scenarios, in particular in terms of impact speed, impact location, and width and height of damage. Based on this, they formulate a single parameter: the Grounding Damage Index, GDI, which includes the ship kinetic energy and its structural resistance to grounding damage.

Why Applications of the GDI parameter are simplified **prediction** tools, which can also be used for risk analysis regarding grounding damage (**accident resistant design**).

What A formula used for calculating the horizontal grounding force for prediction of raking damage to conventional ships and highspeed craft has been presented. The formula depends only on fracture strain, equivalent thickness of the bottom plate and damage width. The formula has been validated against the NSWC grounding experiments and real grounding accidents and has found to predict the horizontal force and also the length and width of raking damage with sufficient accuracy: for the large-scale experiment the prediction of energy absorption is within 5% of the measured value. For the validation against one of the accidents the damage length was predicted with an error of only 11%. This formula can be used to couple the damage width together with the formula presented in Pedersen & Zhang [18]. Both of these formulae have good agreement with the NSWC experiments.

Wang, Arita & Liu, 2000 – "Behaviour of a double hull in a variety of stranding or collision scenarios" [19]

How They propose that the shape of the rock (the sharpness of it) and the location of penetration have a strong influence on the energy absorbing capacity of the double bottom. The rock can hit the structure on three different places: on the shell plating, on a main support member or on an intersection of main support members. Some punch tests were performed on a small double hull structure. The nose radius of the indenter (different sizes of rocks) and the location (centre of plate, main support member or intersection of main support members) where the indenter hits the structure was varied.

Why A simple analytical method is proposed for primary damage mechanisms, which can be used to **predict** the damage to double hulls in various accident scenarios. Also it can be used for probabilistic evaluation of structure performance in grounding. The tests were performed to get a better understanding on the difference in behaviour of a double hull in collision or stranding (**post-process**).

What With a rock with a larger radius, there is a larger load and energy absorption on the structure. The occurrence of rupture is delayed if the nose radius increases. The placement of the rock has less influence. On the shell plating: when the radius decreases, the rupture initiates at the place where the cone tip makes contact with the plate. When the radius increases, the rupture initiates far from the contact point of the cone tip. Instead it initiates at a hard point in the structure (where the shell intersects with a main supporting member). The shell plate always has a certain capacity to carry load even after rupture. This is seen in the force indentation graphs for each test: the force starts to rise again after rupture. There was not a single instance where the load dropped to zero. The residual strength of the global structure takes over immediately.

They emphasize how important the influence of the size of the rock is on the damage to the double hull. In studies, most rocks are described as point loads, but blunt rocks are overlooked although these are very common. This tendency is too conservative.

Wang, Ohtsubo & Liu, 1997 – "A simple method for predicting the grounding strength of ships" [4]

How It is proposed that the resistance force during a grounding in longitudinal direction is periodic in this direction due to periodic spacing of the transverse structural members. This periodic behaviour is shown in a simplified way in Figure 11 and is also observed in data of actual groundings and of grounding experiments. When a rock makes contact with these transverse structural members, that structure and the plating behind it interact with each other. The transverse frame fails by in-plane stretching. The plate behind it bulges and folds even before the it makes contact with the rock tip. During the stage of bulging and folding, the resistance force increases as the longitudinal rock penetration proceeds. Eventually, rupture will occur in the plate, which precedes the rock tip and resistance will decrease again. This is repeated for the next transverse structural member and shell combination. The resistance provided by the transverse member against the intruding rock becomes negligible. The ruptured plate can bend or fold in the two ways circled in Figure 11: the left tear shows material folded outward (curling cut), the right one shows concertina tearing. These ways of tearing are shown in more detail in the photographs in Figure 12.

Why The research has two motivations. One is to be able to predict a ship's hull strength in a grounding event using only hand calculation. The **prediction** method assesses the strength of the ship's bottom against horizontal penetration in order to do a quick assessment of the danger of the situation in such an accident. Much as the thesis' goal to predict the damage to give insight in a dangerous situation. The method can also be used to give a ship **design**er a quick tool to assess his structure's resistance in an accident.

What The paper focusses on the following damage and failure modes: stretching failure of transverse structures, denting, tearing and concertina tearing failure of bottom plates. Simplified formula's to identify these modes are developed. They use the longitudinal loading to assess the horizontal penetration and denting of the plate. The longitudinal loading in a grounding is much different from a collision.

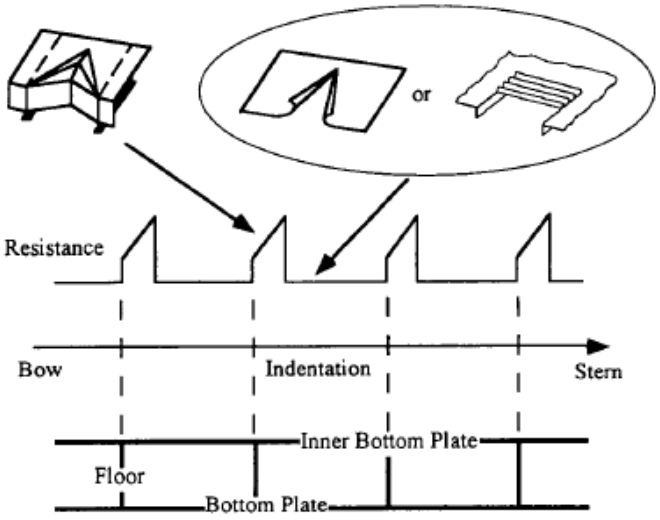

Figure 11 Periodicity of ship bottom resistance (Fig. 2 from Wang, Ohtsubo & Liu [4])

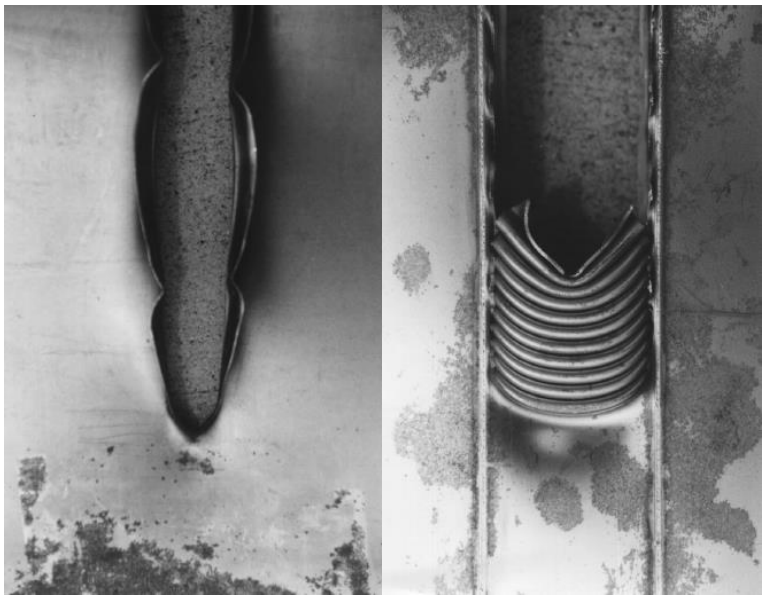

Figure 12 Left: clean curling cut. Right: concertina tearing. (Fig 8.1 from [2])

Pedersen & Zhang, 2000 – "Absorbed energy in ship collisions and grounding - revising Minorsky's empirical method." [18]

How They look at different damage modes and devise a similar formula as that of Minorsky's empirical formula. They devise these energy absorption formulas for the following damage modes: crushing, folding and tearing. After that they validate their new formulas using research from other literature and experiments, including two large scale experiments: the one performed by the NSWC and the one by TNO-ASIS. This is very interesting for this thesis. Their method performs well on the results of the TNO-ASIS experiments. For lower penetration depths the method is close to the test results, but for larger penetration depths the difference between the measured and calculated absorbed energy becomes larger. This is because other damage modes apart from tearing then take over in the outer shell. For larger penetration depths the inner shell is breached as well. The method is therefore more reliable for small penetration depths.

They also present an application of their formulas where the damage length can be estimated using the initial kinetic energy and the absorbed energy. The damage width is here estimated to be constant. The application is validated using a real grounding accident and shows satisfactory agreement. This application can also be used the other way around. The damage width can be estimated when the damage length is known. This could be used in this thesis, applied to the grounding calculation model.

Why They want to keep using the easiness of empirical formulas and avoid the use of FEA. The goal is to revise the formula of Minorsky with recent studies and experiments. This formula was initially used for **design** purposes and **prevention** of spill of dangerous cargo.

What Minorsky assumes that the added mass during a collision is constant, but Pedersen and Zhang state that this is not the case. Minorsky also states that the energy absorption by a ship during a collision or grounding is simply proportional to the volume of the destroyed material. So what this actually tells you is if you want to increase a ship's collision resistance, you should use more material. Pedersen and Zhang indicate that this is not true, because it also depends on the structure and surroundings, arrangement of structure, material properties, damage mode, etc.

Their formula is validated against the TNO-ASIS large scale grounding experiment. As is used for Minorsky's formula, the damaged volume parameter is again included in their version of the formula. For the validation against this experiment they use the energy absorption formula in the tearing damage mode. For two of the series of tests the error between the measured absorbed energy and the calculated absorbed energy is within +15.9%.

Nguyen et al., 2011 – "Understanding of ship grounding" [20]

How A simple procedure estimating the damage of a ship bottom in grounding with associated rock type is presented. Using a certain rock shape and size and a sliding/grounding force a numerical simulation is performed. The seabed is assumed rigid and has a quadratic shaped surface. For the contact forces he assumes simple formula's. Also a friction force is considered in this horizontal grounding force. For simplicity's sake the added mass and damping terms are assumed constant. The assumption of a certain added mass coefficient (surge = 10% of M) is deemed acceptable because of other uncertainties: shallow-water effects (for large sea-beds) and seabed topology (uncertainty of shape/size obstacle). Both a dynamic and a static analysis is done. The analysis of static grounding is performed quasi-statically, i.e., the inertia and damping terms are neglected in the equation of motion.

Why The main goal of the paper is to create a simple method to estimate the damage to a ship bottom and the shape of the obstacle from the results of a dynamic grounding. This can be used for **accident resistant design** purposes or for **prediction** of damage.

What The key parameters influencing the response of a ship hull in a grounding scenario are identified. These are the shape, the initial height over the keel, the penetration into the ship bottom and the contact force of the rock. In the end, the accuracy of the application is uncertain. These uncertainties are mainly related to the neglected effects in the grounding problem. The procedure is validated and it is found that the static method can be used with respect to the results of dissipated energy with reasonable accuracy. To simplify the calculations, fracture has not been accounted for. Also, the method is limited to a symmetric grounding.

2.3.2. External dynamics

Tabri, 2010 – "Dynamics of ship collision" [21]

How Tabri researches the dynamics in ship collision on a model scale. He also gives a short overview of research on external dynamics: Minorksy (1959) was the first on this, with his one DoF model based on the conservation of linear momentum. Woisin (1988) extended the model to three DoF – surge, sway and yaw. Later, Pedersen and Zhang included sliding and elastic rebounding in ship-ship collisions. These are both 2D models in the plane of the water surface and are capable of analysing the loss of kinetic energy in non-symmetric collisions (ship hitting other ship's side anywhere else than CoG) by damage to the structure.

In his research, Tabri is interested in these non-symmetric ship-ship collisions. He therefore performed model-scale experiments (because large-scale are costly). He designed and validated the set-up (w.r.t. the problem of scaling) to large-scale collision experiments. He also studied the effect of sloshing using his experiments. Sloshing is a transient fluid motion inside a tank caused by rapid movement of the ship, in the case of grounding: rapid deceleration. The effect of sloshing in such a case causes time-varying loads in the tanks and this way causes a change in energy distribution during the event. He scaled his model using the Froude scaling law. This leads to proper relations between inertia and gravity forces. However, the viscous forces are overestimated. He reasoned that these forces, however, play only a minor part in the transient character of ship collision.

Why The experiments were carried out to extend the physical understanding of ship collisions (**post-process**).

What Tabri mentions the importance of the hydrodynamic radiation force, which has a strong influence on the energy distribution. The energy corresponding to radiation force increases in non-symmetric collisions as a result of the longer contact duration (ship sliding against ship) compared to that of symmetric collisions. He states that the main components in collision dynamics are the hydromechanical forces, especially the radiation force (constant added mass times ship acceleration), the ship's inertia (ship mass times ship acceleration) and the contact force (ship-ship contact, external load). He concludes that if the interest is in the maximum collision force and penetration depth, then the approach based on the constant added mass and ignored hydrodynamic damping is still reasonable, as the error in the deformation energy is in that case about 5%.

Finally, Tabri reasons that both the internal and the external mechanics should be coupled. He finds that in the case of non-symmetric collisions, damage paths are heavily dependent on the ship motions during the collision and on the structural properties of the ship. The decoupled approach in this case predicted a penetration which was too deep and a damage path which was too short. The decoupling is only possible in symmetric ship collisions. In such a collision the ship motions are limited to a few components and the contact force as a function of the penetration can be predefined. Statistical studies (Lützen, 2001; Tuovinen, 2005) have, however, indicated that the majority of collisions are non-symmetric in one way or another. This implies the need of a coupled approach. The large-scale collision experiments reveal that the collision models from before 2000 (as he summed up in his overview) do not explain all energy-absorbing mechanisms. That is why he now wants to consider sloshing interaction in collision dynamics as well.

Pedersen & Zhang, 1998 – "On impact mechanics in ship collisions" [22]

How The authors present analytical expressions to calculate the energy loss and the impact pulse during ship collisions. These expressions are restricted to the motions surge, sway and yaw. They are based on rigid-body mechanics, where it is assumed that there is negligible energy release by deformation outside the contact region and that the contact region is local and small. This causes an impact pulse at the point of contact.

They perform time simulations to validate their presented mathematical models. They test it on three situations: ship-ship collision, ship collision on a rigid wall and ship collision against an off-shore jack-up rig.

Why Their presented expressions can be used for probabilistic calculation models for damage of ship structures caused by collision (which can be used to **predict** and for **accident resistant design**).

What The authors discuss the way Minorsky assumes his added mass coefficients, because for collisions of longer duration the constant added mass coefficient (for example, 0.4 for added mass in sway which is 40% of the ship mass) proposed by Minorsky is not accurate anymore. They state that according to Motora the added mass during collision can vary from 0.4 – 1.3. The longer the duration, the higher the coefficient. But for short duration collisions Minorsky's value can be used safely. Ultimately, Pedersen and Zhang keep using constant added mass coefficients for their model for simplicity's sake. The determination procedure on the added mass coefficients is important for this thesis.

They finally derive an analytical method for the energy released for crushing in collision. The results are mainly determined by the ship mass, velocity, the collision location and collision angle.

2.2.3. Analytical models

Simonsen & Wierzbicki, 1996 - 'Grounding bottom damage and ship motions over a rock.' [12]

How They present the analytical ship motion model (also presented in [2]). They state that for grounding on a sloping beach a three DoF model in the vertical plane is enough. But for grounding on a relatively narrow object like a rock this is not enough and all six degrees of freedom must be considered. First they look at the ship motions in the horizontal plane in order to investigate what the sway and yaw motions are in grounding.

They determine the motions and the shape of the damage path by assuming a certain damage length first (meaning a certain constant horizontal grounding force in the direction of the ship speed). This is just the reverse of what I am trying to achieve for the investigation. They propose that if the rock does not hit the ship in its symmetry plane, the ship rotates around a vertical axis at the rock, resulting in a sway and yaw motion. The simulation stops when the relative velocity between rock and ship is zero. Now the ship can rotate around the rock, but this does not increase the damage length any further in longitudinal direction.

Why After the grounding of the Exxon Valdez, more research activities in the field of crashworthiness of ships is performed. The goal of the paper is to present the basis of an analytical model for assessment of ship damage due to grounding on hard rock (**prevention** and **post-process**).

What They simulate a couple of grounding scenarios. Of the initial kinetic energy, a maximum of 3.72% goes into the rotation. This is insignificant to the longitudinal dissipated energy. The damage length is higher if the rock hits the ship at its bilge than when it hits the ship at the symmetry plane. However, the maximum penetration is the smallest here due to the reduced global stiffness and due to the roll motion. Based on the results, a simplified model can be established for the global ship motion. For this model they neglect the yaw and sway motion and calculate heave, roll and pitch from a requirement of static equilibrium. This equilibrium states that the ship's kinetic energy after the rock has penetrated a horizontal distance X_S is the initial kinetic energy minus the ship's potential energy at this distance due to trim minus the horizontal rock force over the traveled distance.

Simonsen, 1997 – 'Mechanics of ship grounding.' [2]

How Simonsen is interested in both parts of the analysis of ship grounding. External dynamics analyses the problem of ship grounding with respect to how the motions of the rigid ship are given a certain grounding force on the hull. Internal mechanics gives insight to the forces on the hull given a certain penetration of the rock into the hull. He also separates internal mechanics in two different energy dissipation systems: energy dissipation by deformation and fracture and energy dissipation by friction.

Simonsen creates two external dynamics calculation models. One in the vertical plane including the motions surge, heave and pitch. This model simulates a flexible ship grounding on a soft seabed. The seabed is wide so only these vertical plane motions are considered. He does not take into account the response of the impact on the local structure, but only the flexibility of the ship as a whole. He verifies his model with a small- and large-scale model test.

He creates a second model in order to investigate the external dynamics of a grounding on a sharp rock. This model is the one discussed in the paper reviewed above [12].

Why The purpose of the study is to contribute to the understanding of ship grounding events (**post-process**). The study is part of a bigger study with the objective to make an **accident resistant design** for ships.

Zhang, 2001 – "Plate tearing and bottom damage in ship grounding" [23]

How In a grounding one wants to know the shape of the rock so that a good estimate of the damage can be made. It has been found that the damage width is an important factor on the effect of the steady-state cutting force. The horizontal cutting force of the rock can be presented as a force with periodic peaks as the rock impacts with transverse members in the bottom structure. The effects of the rock shape/angle/friction has been put in an empirical formula of the horizontal grounding force.

Why Semi empirical formulas for the raking damage length for certain ship types for high energy ship grounding scenarios are proposed. With these, for example, an estimate of the damage extent in ship grounding accidents can be done using only the ship's principal particulars. This is the same goal and application as envisioned in this thesis, **prediction**.

What He finds that motions such as heave, pitch and roll have some effect on the penetration depth, but it does not have a large effect on the damage length (negligible).

3

Accelerations of the grounding experiment

The grounding of Pasha Bulker. June 8, 2007. Newcastle, New South Wales, Australia.

3.1. Introduction

As discussed in the Chapter 1, the extent of the raking damage is categorized in two: the magnitude of the damage (how the local structure is affected by the grounding) and the location of the damage (how the grounding affects the ship globally: the same damage in different areas can have different consequences). The first sub-question is posed to investigate this first aspect of the raking damage extent. The first sub-question is:

How can acceleration time-traces be related to damage?

The question is formulated to get a grip on how these acceleration time-traces measured on board look like in case of a certain magnitude of raking damage and how they can be related to such damage. In order to answer this question, the accelerations measured on board during the TNO-ASIS grounding experiment are analyzed together with the resulting damage from the experiment [1]. A review of the experiment is given in section 2.2.1.

It is chosen to analyze the data of this particular experiment because of a few reasons. First, this experiment is performed with all ship motions: surge, sway, heave, roll, pitch and yaw. For example, the test-section used in the NSWC experiments ([9], [10]) could only move in longitudinal direction while making contact with the rock. For this analyses, however, I am interested in the external dynamics of the grounding as well. How does the impact with the rock have influence on the ship as a whole? Another reason this experiment is used is because the experiment is performed at large-scale. More experiments on both external dynamics and internal mechanics have been performed, but most of them are small-scale experiments. The large-scale grounding experiment will agree more closely to data from a realistic grounding while having the benefit of being in a controlled environment.

3.2. Acceleration signals explained

3.2.1. Location of the accelerometer

One of the first questions on the topic of using real-time acceleration measurements is how big the influence of the placement of the accelerometers is on the measured acceleration signal. In this paragraph it is investigated if the response of the rock damaging the ship structure is measurable and observable even while the accelerometer is 30 m away from the impact location. The accelerations of the large-scale experiment are measured using the motion pack, which is placed amidships. The placement of this motion pack is shown in a top view of the support ship in Appendix B.

During the experiment, the ship is slowed down by the grounding force. The measured surge acceleration signal is therefore actually the surge *deceleration*. Figure 13 shows this deceleration in this direction. The figure shows the behavior of the rock ripping through the five floors. In the figure which plots the deceleration against longitudinal penetration the spacing in between transverse frames of 1250 mm is observed clearly. The same effect is observed in the NSWC experiment data in Figure 8 which has been discussed in the experimental study. The effect is also observed in the drop-tower experiment data performed at TNO [24] in Figure 14, where the colliding with a trimmed plate (green dashed line) and sequential rupture (red dashed line) is detected.

The effect is also described in literature, in a paper by Wang, Ohtsubo & Liu [4]: the structural resistance builds up by the bulging and folding of the plating in front of the rock. After rupture of the plating the resistance drops to a lower level than just before. Figure 13 even shows that the deceleration becomes negative after rupture, meaning that the support ship/test-section is not slowed down anymore but even regains speed again. This will be elaborated on in section 3.2.3. Unlike discussed in [4], it is not expected that these resistance periods reoccur in the same magnitude exactly, because through the pitch and heave motion of the support ship the test-section is loaded less or loaded more. Figure 17 shows energy dissipation mechanisms such as folding, denting and tearing, just as predicted by [4] and shown in Figure 11.

The time interval between acceleration peaks due to the resistance of the transverse floors is becoming larger as the ship is slowed down by the rock. The final large positive acceleration (t = 3.3 – 5 s) is due to the rock colliding into the buffer, which is depicted in Figure 15 and Figure 16. The buffer is installed as a precaution: it absorbs the residual kinetic energy of the ship in case there is still some left. In that case the ship is protected. The ship is slowed down by the buffer very fast resulting in high decelerations (almost as high as on the moment of first impact, around 3 m/s^2). The buffer is filled with polystyrene foam of 50 kg/m^3. The same happened in the small-scale raking damage experiment, pictured in Figure 14, where the indenter collides with rubber brake pads to dissipate residual kinetic energy and protect the test set-up.

Conclusion

The acceleration signal in surge from this experiment shows how the structure reacts to the contact with the rock. Therefore it tells that the resistance of the ship structure is still observable around L/2 m (= 30 m) away from the impact location. The signal, however, does not say anything about to what extent it is influenced by the ship structure. The acceleration signal is also influenced by the trim angle of the ship. This is discussed in section 3.2.3.

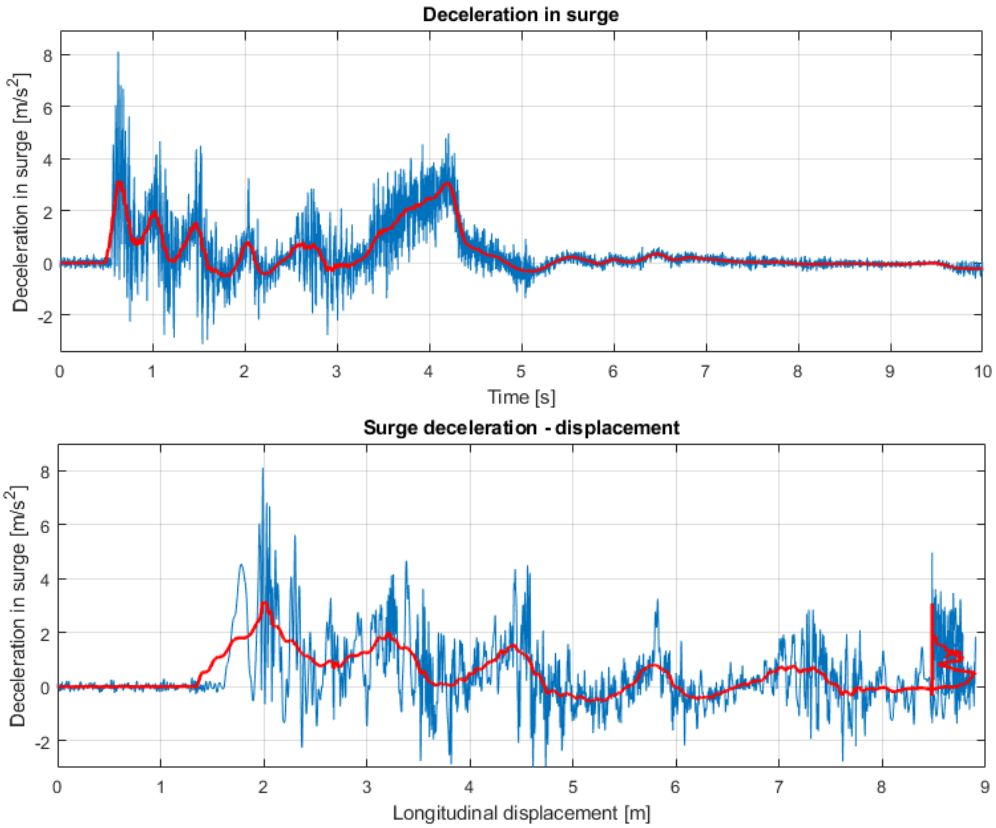

Figure 13 Acceleration in surge measured amidships in time and along longitudinal rock penetration measured by wire gauges. Blue is raw data, red is smoothed data (moving average span = 800).

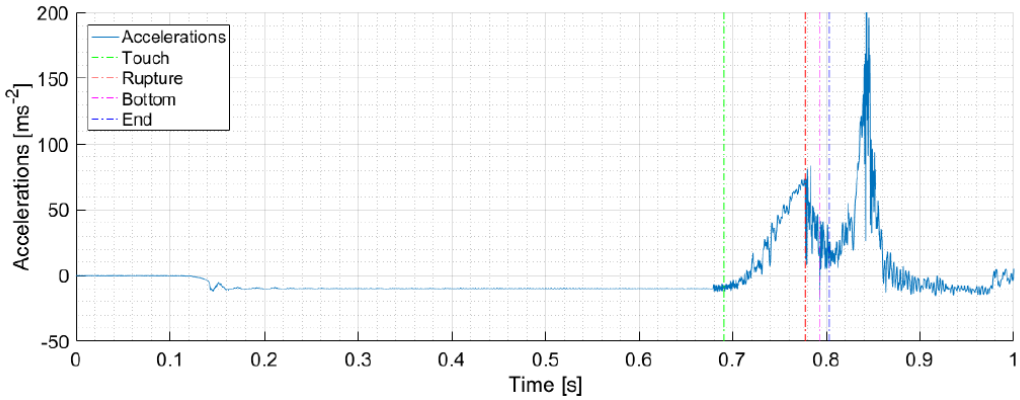

Figure 14 Acceleration signal of drop 4 [24]. Moments in the experiment are marked. The last peak is the indenter colliding with the rubber brake pads.

Figure 15 Mounting of the buffer on the Nedlloyd 57. The buffer is added as a precaution; in order to dissipate the ship's kinetic energy that is left after grounding test-section. The buffer is completely filled with foam.

Figure 16 Left: The artificial rock stuck in between the test-section and the buffer. Right: The damage to the buffer by the rock after removal of the test-section.

Figure 17 Part of the damage path to the bottom structure of the test-section. Failure mechanisms visible: folding, denting and tearing.

3.2.2. Acceleration signal and damage assessment

Since the response of the rock impact is observed in the measured acceleration signal, the question arises what exactly is seen in these acceleration signals that can be related to the reported damage. In Figure 19, measured acceleration signals are shown for each translational ship motion: surge, sway and heave. In these graphs, interesting moments during the grounding are marked with vertical dashed lines. These markers show which part of the test-section is reached by the rock in time. Green indicates the beginning of the grounding (the first moment the ship is in contact with the rock). Magenta indicates rupture of the plate behind the transverse bulkhead (to be explained). Black indicates the buffer first touching the buffer. These are marked based on changes in the surge acceleration signal. In Figure 20 the same interesting moments are marked in a simplified representation of the side view of the rock and test-section in order to give a better view on what is happening at what location based on the acceleration signals. Maximum surge acceleration levels are -5 m/s^2 (0.5 g), maximum acceleration levels for sway and heave are around 3 m/s^2 (0.3 g). These figures will be compared to the reported damage from the damage report of the experiment in Appendix A.

Start grounding

The green line, at t = 0.5 s, marks the start of the grounding. The rock is starting to ram into the front of the test-section. In surge, a positive acceleration is measured and the ship is slowed down (in the figure positive acceleration indicate deceleration). In sway, large fluctuations around zero are measured. Upon impact the measured sway accelerations are the highest (3 m/s^2), after the first impact the maximum sway accelerations are 1 m/s^2. This is explained by the denting of the bottom plate. The prominently longitudinal motion will force the test-section to slide over the rock tip. This will guide it through the dented bottom plate mostly in longitudinal direction, because of the transverse resistance of the structure (keep in mind the longitudinal stiffeners). It allows for less motion in transverse direction, resulting in lower sway accelerations. In heave, it is seen how the ship is lifted (positive acceleration), but is then dropped because the rock is tearing through the bottom plating just behind the front frame of the test-section.

First rupture

This rupture happens at the first magenta line, t = 0.6 s. In Appendix A, a simplified representation of the bottom of the test-section is shown where deformation and rupture in the bottom plating is depicted. In the sway acceleration signal it is seen that the fluctuations decrease in magnitude after passing the front of the test-section. This is because the rock is lodged in between longitudinal stiffeners and in the tear. This makes it harder for the rock to diverge from a straight path in longitudinal direction. Just after rupture it is seen that the resistance in surge direction decreases and the rate the ship is slowed down decreases as well.

First frame

The structural resistance increases again when the rock meets the first transverse frame at t = 1.0 s (for clarification: front of test piece counts as first acceleration peak + four floors in total make up for the other peaks in acceleration). But the tear is still growing until it reaches the next increase of structural resistance near the second frame.

Second frame

After passing the second frame at t = 1.5 s it is seen that the magnitude of all accelerations is small in all graphs until t = 2.6 s. In sway, the fluctuations are small and are of lower frequency. This is because now there is no rupture of the bottom plating. Instead, the front of the ship is lifted and slides over the rock (as is seen in the pitch angle alongside the surge acceleration in Figure 22). In this time span the damage path is reported being small (zone of deformation is only around the size of the tip of the rock) as is shown in the damage report.

Third frame — A tear is located in front of frame no. 3 at t = 2.1 s. This could be the late effect of the tearing in advance of the approaching rock tip from frame no. 2. The tear is most prominently in transverse direction. This is explained by the effect described by Wang, Ohtsubo & Liu [4] and is conform the rupture initiation mechanisms found in literature and shown in Figure 18 which is discussed later on. This type of rupture can be explained by the resistance of frame no. 3. The structure's weakness is here mainly in transverse direction.

Fourth frame — Rupture occurs again at t = 2.6 s, but the damage width is small. Sliding of the ship explains the tear. The ship slides over the rock, but at some point the ship becomes too heavy to balance itself on the small area of the rock tip, causing rupture of the local plating and the rock penetrating the hull. This is also supported by the declining trim angle at this point in time (Figure 22).

Buffer — The space between the end of the test-section and the buffer is empty. The acceleration signals attenuate until the rock collides into the buffer at the black dashed line at t = 3.3 s. The ship comes to a standstill very fast. The residual kinetic energy of the system is dissipated through damage inflicted to the buffer.

In the damage report (Appendix A) two types of rupture initiation mechanisms are identified: type I and type III [10]. These types of rupture initiation mechanisms are found and investigated in the other large-scale grounding experiment [10]. An explanation of these rupture initiation mechanisms: all mechanisms start with a simple longitudinal rupture at the base of the rock, because of transverse membrane stresses in the bottom plate make that the crack tip propagates in the direction of the movement of the rock. As the rock makes contact with a transverse frame, rupture initiation processes begin: Type I rupture progresses into a vertical crack up the transverse frame/bulkhead. This happens when the rock is in between longitudinal stiffeners, which also happens in the experiment. Because of the slope of the rock, this happens before the rock tip is at the location of the transverse frame. This type I rupture mechanism can be viewed at the location of the front of the test-section, the first frame until the second frame and the fourth frame. A type III rupture happens just before the third frame. At this point the ship is sliding over the rock, but the local plating cannot hold the weight of the front of the ship on the small rock area at some point. Rock contact against the transverse frame plating causes a change in the outer shell stress field. Instead of only transverse stresses the plating is now also longitudinally stressed. The rock 'falls' through the plating and causes a rupture which develops in both transverse direction and propagates to the longitudinal stiffeners. Both types of rupture mechanisms are more clearly shown in Figure 18. Although the acceleration signal can indicate rupture, the type of rupture initiation mechanism, however, cannot be observed until visual investigation of the damaged test-section.

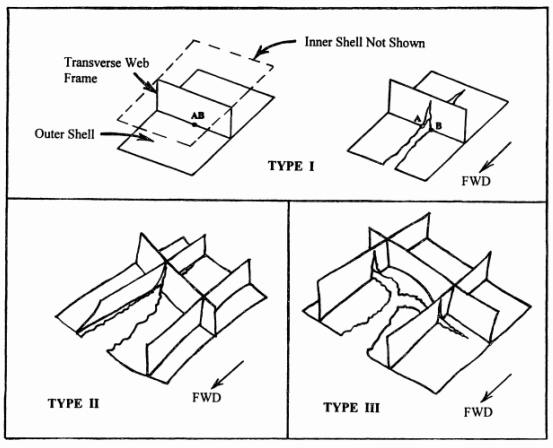

Figure 18 Rupture initiation mechanisms [10]

Conclusions

The rupture of the plate just behind the bulkhead shows the described effect from Wang, Ohtsubo & Liu [4]. Figure 19 shows that the described effect occurs periodically, every 1.25 m (transverse stiffener span). Although it is possible to observe rupture from the acceleration signal, the type of rupture initiation mechanism, however, cannot be observed until visual investigation of the damaged test-section.

Weak acceleration signal but a forward speed still could indicate that the grounding is still happening, but that the rock is just scraping the ship's bottom or denting the bottom plating a small amount. Making only a small indentation because the ship is also lifted.

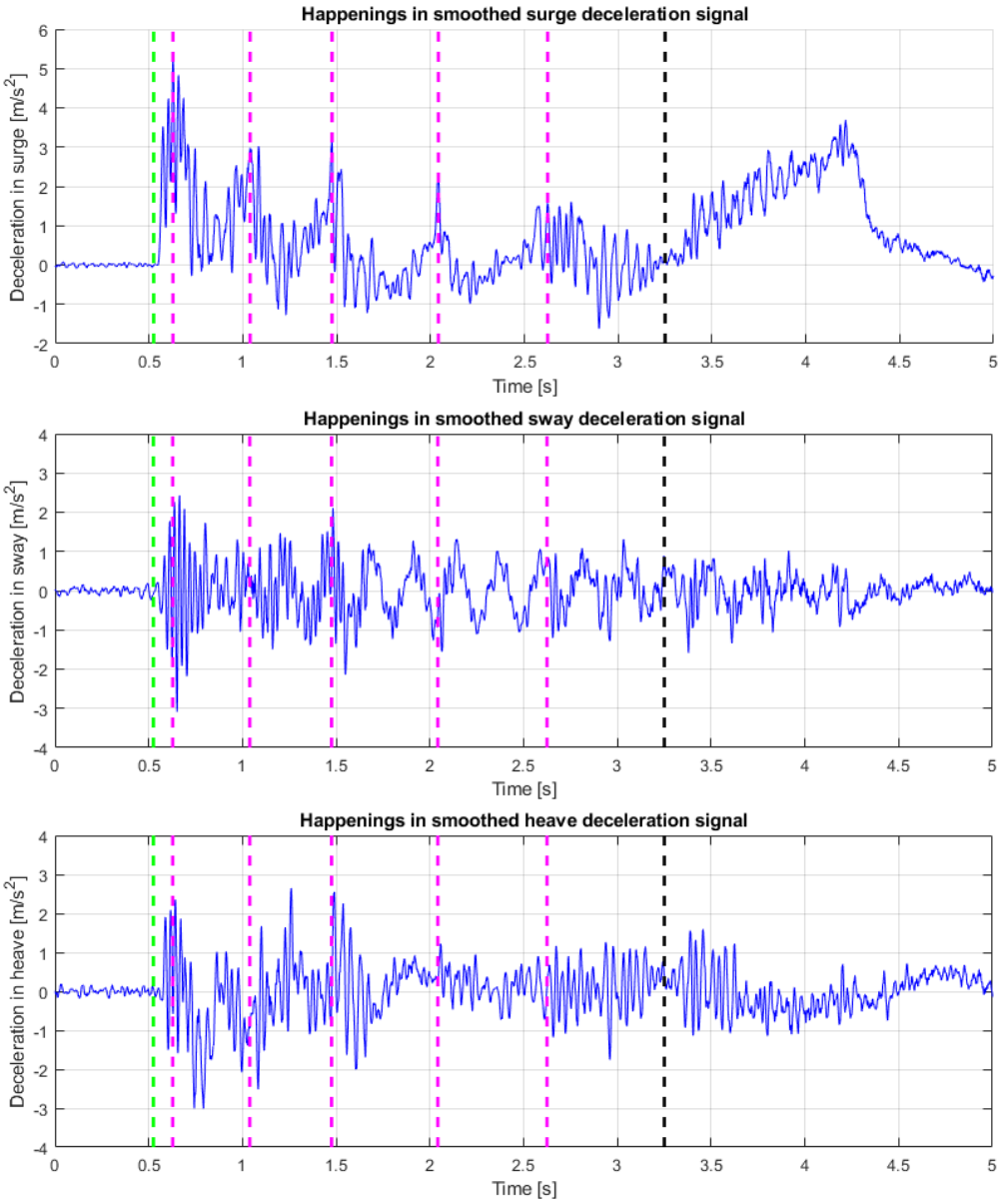

Figure 19 Interesting moments marked in smoothed deceleration signals (moving average span = 100). Green = Start grounding; Magenta = Rupture of plate in front of indenter; Black = collision with buffer.

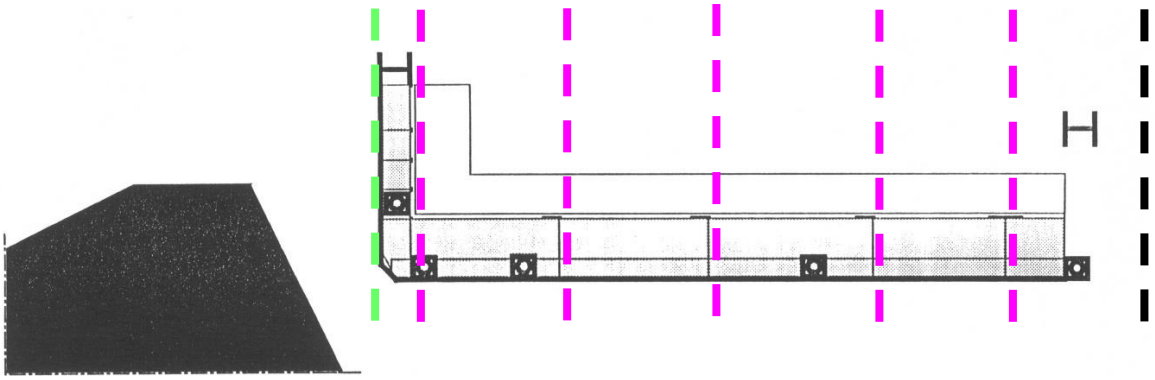

Figure 20 Interesting moment marked on the side view of the test-section. Green = Start grounding; Magenta = Rupture of plate in front of indenter; Black = collision with buffer.

3.2.3. Acceleration signal and pitch motion

Another question is how the acceleration signal in one direction of motion is influenced by another motion. It is observed in section 3.2.1 that the surge deceleration signal in Figure 13 dips below zero, meaning the ship is speeding up again. It is investigated if this is because of influence of other motion's accelerations.

The accelerations are measured with the motion pack located in the middle of the support ship (Appendix B shows a top view of the support ship and the location of the measurement systems). Therefore the signal is the least influenced by the other motions such as pitch and roll. If the accelerometer was for example placed on the front of the ship at distance *r*, the accelerometer would measure an additional $\ddot{\theta} r$ acceleration when the ship pitches (pitch acceleration times distance accelerometer to ship CoG).

However, with the motion pack located in the ship's CoG, it still experiences the effect of pitch/roll. However, because of the small measured roll motions of the ship during the test this motion is neglected. While the trim angle increases, the accelerometer also measures the gravitational acceleration, *g*. Figure 21 shows a diagram indicating the global axes x_g and z_g and the body fixed axes x_b and z_b. The body fixed system pitches positively with trim angle θ. The accelerometer measures a smaller surge acceleration than in reality because of the measurement of $-g \sin\theta$. The linear measured surge acceleration (excluding g) is larger and therefore the correction is $\ddot{x}_{corr}$. The accelerometer is vertically calibrated for -*g*. When a trim angle exists, the accelerometer measures a smaller contribution of g in the heave accelerations. The linear measured heave accelerations (excluding g) is actually smaller and therefore the correction is $\ddot{z}_{corr}$. The measured surge and for heave accelerations from the motion pack are corrected using Equation 1 and 2. Here θ is the trim angle (positive angle is right turning from x- to z-axis) and *g* is 9.81 m/s^2. The grounding experiment begins with the ship already under a certain trim angle. This is neglected, because the accelerometers are calibrated at zero in this position and measure in the ship's coordinate system. The corrected heave and surge accelerations in the coordinate system of the ship under trim angle θ are:

$$\ddot{x}_{correction} = \ddot{x}_m + g \sin\theta \quad (1)$$

$$\ddot{z}_{correction} = \ddot{z}_m + g(1 - \cos\theta) \quad (2)$$

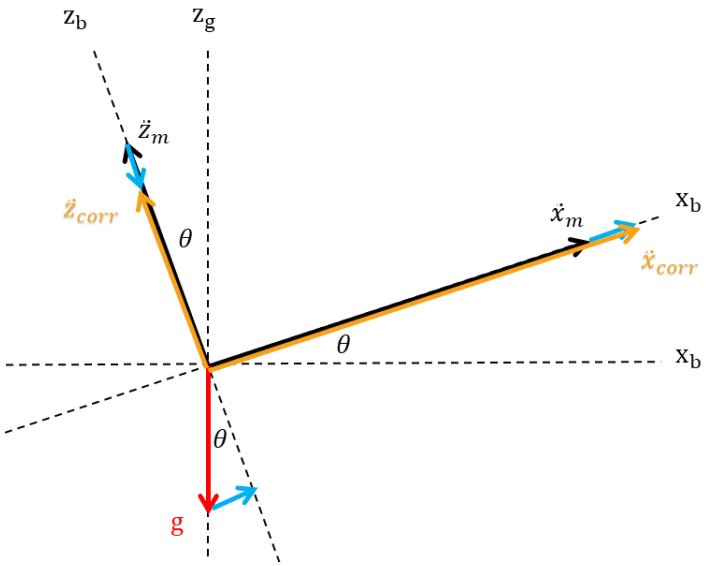

Figure 21 Overview heave and surge acceleration measurements under trim angle

In this approach the contribution of the angular velocity/acceleration is neglected, because of the small maximum angle and a measured maximum angular pitch velocity of 0.044 rad/s (= 2.5 deg/s).

In Figure 22 and Figure 23 the corrected acceleration signals are plotted alongside the actual measured accelerations signal and the trim angle. The correction is observed most clearly in Figure 22, where the trim angle is at some point in time large enough to account for an observable effect. Still, the acceleration signal is below zero after the previous peaks between t = 1.5 and 3 s. This means that the support ship/test-section still regains speed instead of slowing down. This concludes that the correction of *g* does not make up for this.

Another reason that can explain the negative accelerations is that there was still thrust created by the ship's propulsion system. The rock force is on this point of the grounding not large enough to hold back the moving ship. This is probably because of the ship sliding over the rock at this moment in time as was explained before in section 3.2.2**.** Another reason is that the volume of water moving with the ship, gives the ship at this moment of the grounding an extra push. The ship is slowed down, but the surrounding water not so much and keeps moving in this direction. Also, during the experiment, the tanks weren't filled completely. The ship was ballasted so that the ship plus test-section were positioned just right for the impact with the protruding rock above the waterline. As a result this caused sloshing of the tank contents. This can also cause the same effect as the added mass of water, giving the ship an extra push at this moment during the grounding. Another reason is the compression of the ship in longitudinal direction. The ship could act as a spring which is compressed upon impact and released once conquering friction with the rock at the moment of sliding.

Conclusion

Contribution of motions between themselves is negligible for the accelerations used in this analysis.

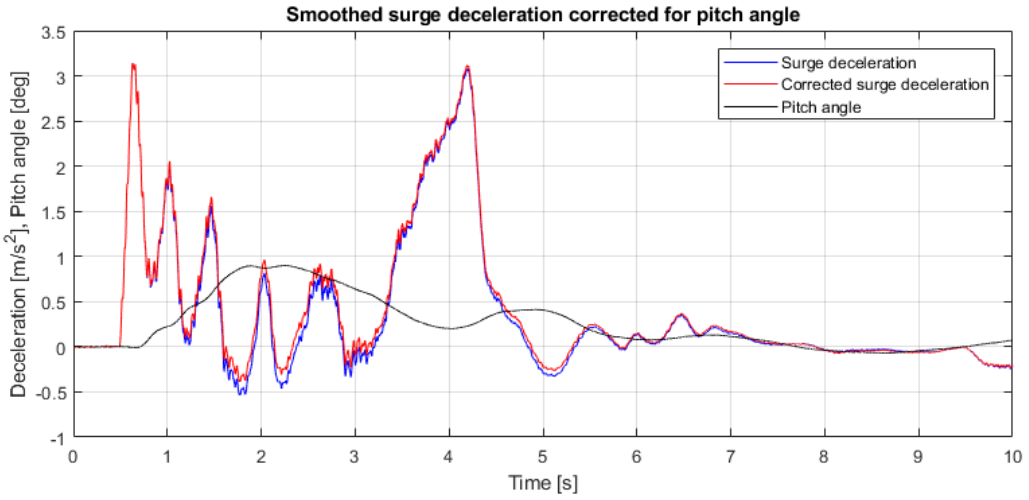

Figure 22 Pitch and smoothed acceleration in surge corrected for the trim angle (moving average span = 800)

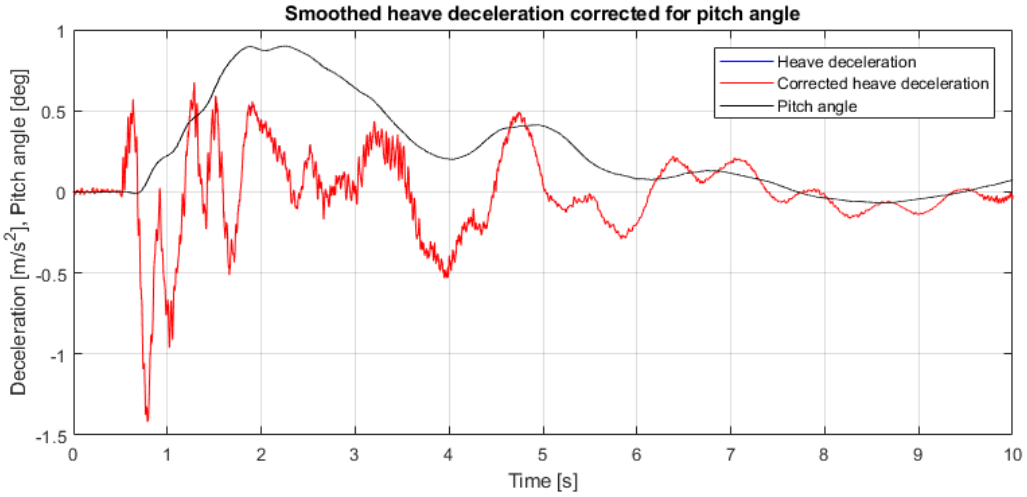

Figure 23 Pitch and smoothed acceleration in heave corrected for the trim angle (moving average span = 800)

3.2.4. Integration of acceleration signal

The acceleration signal can be used to do a quick assessment of the longitudinal damage path. Both the velocity and the longitudinal displacement derived from the acceleration signal by respectively single and double integration in time are plotted in Figure 24. Also, the longitudinal displacement measured with the wire gauges (wire in winch measuring between pontoon/rock and test-section, see Appendix B for setup of these wire gauges) is plotted. Until t = 3.3 s, these plots coincide. After the buffer is hit, the acceleration peaks and causes the extra calculation of displacement while the wire gauge measures no more displacement because the rock is stuck inside the buffer. The steep part in the wire gauge displacement plot, t = 3.3 s, is caused by the wire vibrating upon impact with the rock in the buffer. After that, the ship comes to a standstill. The velocity is a constant 3.73 m/s from t = 0 s to around t = 0.5 s when the grounding begins. The distance covered in this timespan (around x = 3.73·0.5 = 1.87 m) is subtracted in the displacement plot (starts at 0 at t = 0.5 s). This distance does not count for the damage length/longitudinal penetration. Between the third and fifth magenta line the ship regains some speed twice because of the reasons discussed earlier (why there is a positive acceleration). During the period of sliding over the rock the ship has an average speed of 2.5 m/s.

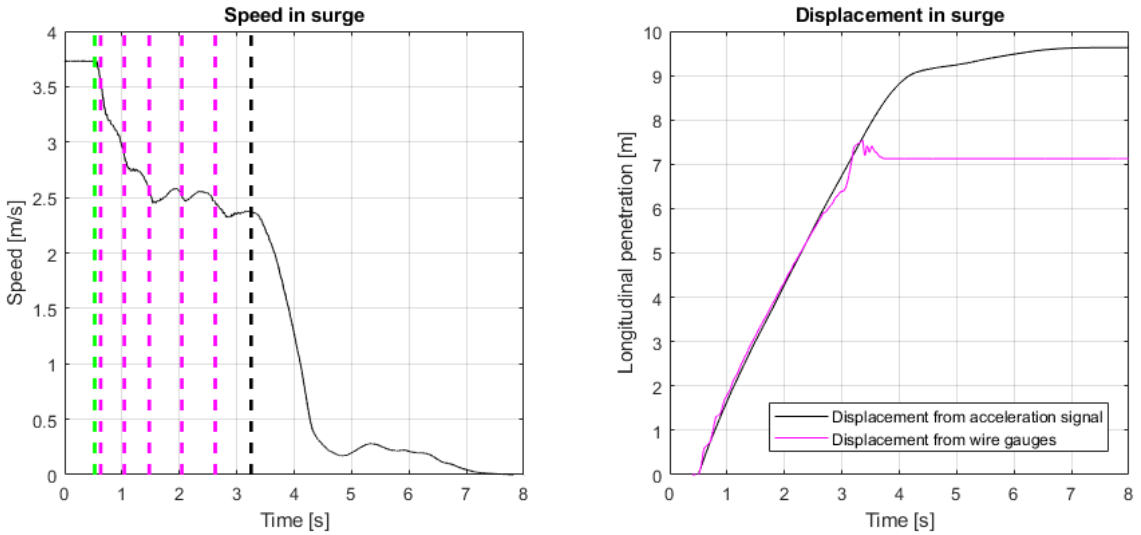

Figure 24 Speed and longitudinal displacement derived from the acceleration signal in surge. Moments during grounding indicated with vertical dashed lines. Green: first impact with rock. Magenta: rupture. Black: impact rock with buffer.

3.3. Signal identification

Now the acceleration time-traces are processed through the means of signal identification. Besides the acceleration signal the force signal is processed as well, because this shows the response of the test-section under grounding load. Through this process is investigated how both signals compare to each other and if they tell the same story (as is expected because of Newton's second law). This investigation will tell if acceleration measurements are a good replacement for measured grounding forces. Because in a real grounding incident, measuring the latter is not possible.

A short study is performed on the topic of signal identification. This is found in Appendix E. The purpose of the study is to find out how each type of transform behaves and which is used best in this situation. The types of signal identification discussed are the Fourier analysis, wavelet theory and Hilbert transform. An explanation on why these are chosen is given in their respective paragraphs and in the Appendix.

3.3.1. Fourier transform

The most widely used method of signal identification is Fourier analysis. First and foremost, a Fourier transform of a signal tells you what frequencies are present in your signal and in what proportions. The data from the large-scale experiment is subjected to this transform. The longitudinal signals are used for this, because the signals measured in this direction shows the response of the damage of the test-section due to the rock most clearly. The surge acceleration signal is multiplied by the ship mass, M, to obtain the force in time. This is compared to the longitudinal force measured with the longitudinal load cells at the ship and at the rock. Both load cell configurations (at ship and rock) are shown in Appendix B. The three signals are plotted together in Figure 25. The figure shows that the force derived from the acceleration signal is higher than the force measured with the horizontal load cells at ship and at rock. In the force derived from acceleration and the forces measured at the rock the impact with the buffer is detected, but not in the measured force signal from the test-section (between t = 3 – 5 s). This is because the buffer is not part of the test-section and these forces are therefore not registered. One would expect the same longitudinal force between the load cells at ship and rock, but the figure shows this is not the case. The force measured at the rock is smaller than the force measured at the test-section. This is probably because not all the load of the test-section on the rock was measured longitudinally, but was also measured vertically by the other load cells through a bending moment.

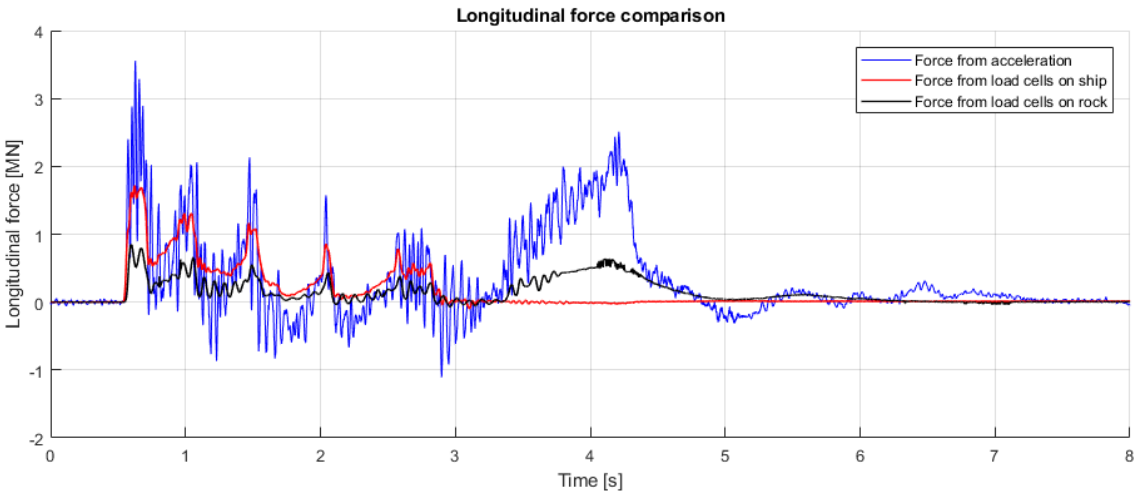

Figure 25 Forces in surge. Blue is the force derived from smoothed acceleration signal multiplied by ship mass. Red is the force measured by the load cells on the ship. Black is the force measured by the load cells on the rock.

The analysis is done by a fast Fourier transform (FFT). For more accuracy, it is only performed over the most useful part of the data: from the beginning of the grounding, at t = 0.5 s, to just before the impact with the buffer, at t = 3 s. This way the FFT's frequency spectrum is not contaminated by the frequencies caused by the response of the buffer.

The force derived from the acceleration signal shows large peaks and noise during the whole measurement. To get a more clear view of the signal a filter is applied. This is done using FFT as well. The signal is filtered using a multiplicative rectangular low-pass filter. It passes the low frequencies, but completely cuts off the unwanted higher frequencies above a certain passband (the reoccurring pattern of noise in the overall shape of the signal). To do this a cut-off frequency must be determined first. Figure 26 shows the forces and the filtered force from acceleration signal for four different cut-off frequencies. Ultimately, the cut-off frequency of 40 Hz is chosen. It leaves out all the higher frequencies and has good resemblance with the force signal measured at the ship, because the interest lies in the response of the test-section. Good resemblance with the force signal is a good indication these frequencies are because of the test-section. The two-sided spectrum is plotted in Figure 27, showing the cut-off frequency as a vertical black line. On a first look the load cell signal of the ship is far less noisy. This is confirmed in its FFT in Figure 28 for it contains less higher frequencies than the acceleration signal. No frequencies above 50 Hz exist in the signal. The signal is filtered using the same method and the result is plotted in black in the same figure (Figure 27). Comparing the filtered force with the force from load cells shows large resemblance in trend and magnitude. It seems as if the constant ship mass is an overestimation at some points in time and an underestimation at others. This can be explained by the effects discussed in section 3.2.3.

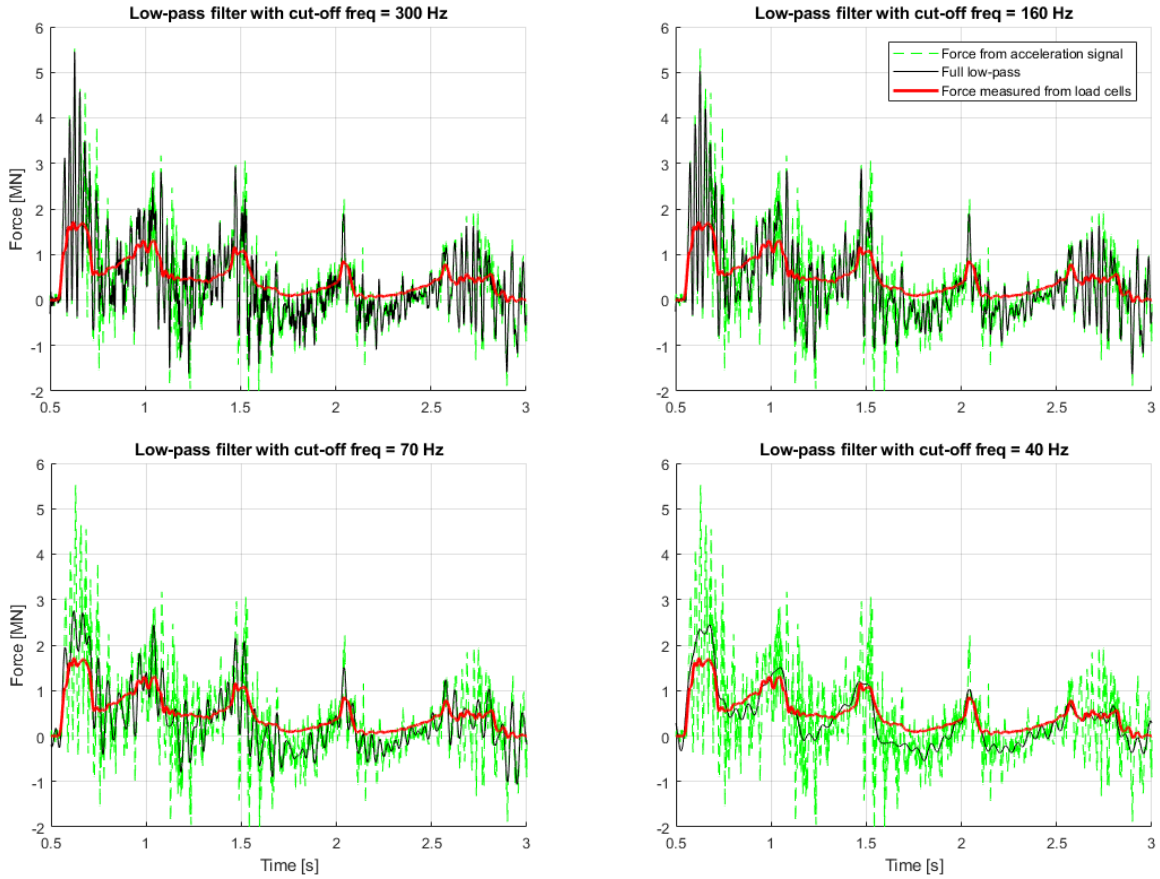

Figure 26 Low-pass filtered force from acceleration signal and force from load cell signal compared. Different cut-off frequencies used.

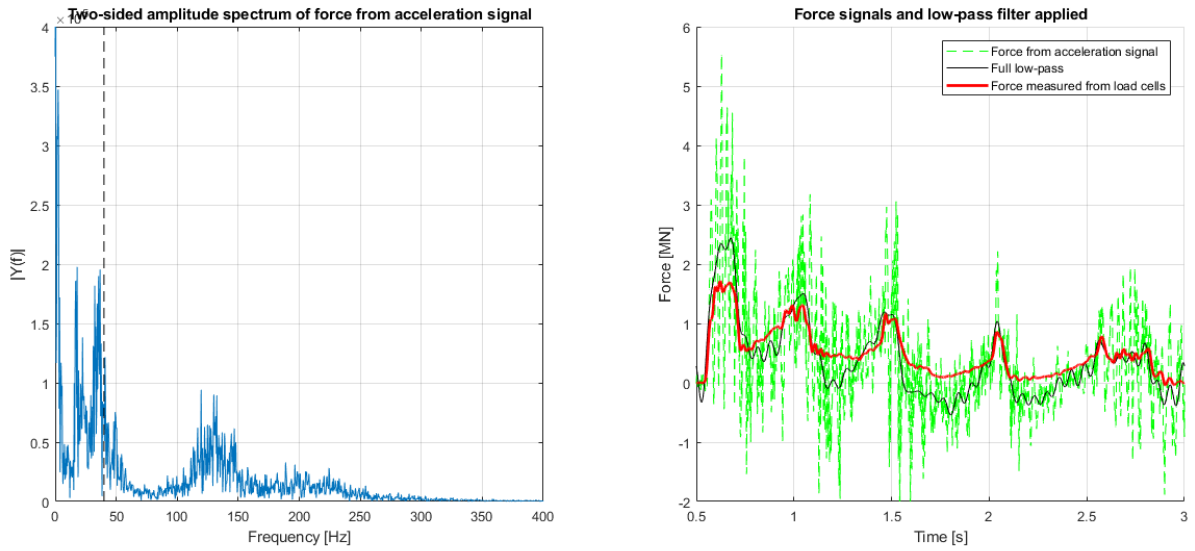

Figure 27 Left: FFT of force derived from acceleration signal. Right: Application of low-pass filter.

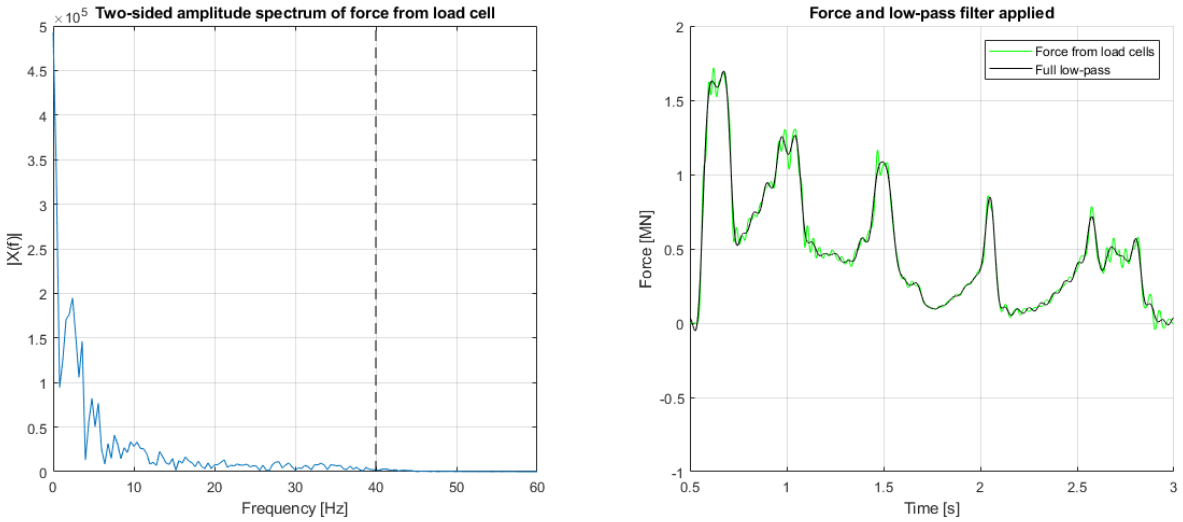

Figure 28 Left: FFT of force from load cell at test-section. Right: Application of low-pass filter.

From the amplitude spectrum in Figure 27 and Figure 28 a couple of high intensity frequencies are observed. These are summed up in Table 2. Here the range is given if there is not a clear single frequency peak. The mean is taken over this range. When there is a clear single peak, this is given in the *mean* column without a given range. A close-up of these amplitude spectra in the range of 0 Hz to the cut-off frequency is given in Figure 29. In order to see if the FFT of the force from rock reveals something interesting, it is plotted in this figure as well in black.

It is interesting to see that the same frequencies exist in all signals between 0 and 15 Hz. The peak around 0.4 Hz is the highest in intensity for all signals. The peak around 1.6-2.8 Hz (2.2 Hz) is the second highest frequency in intensity and can be explained by the five peaks resulting from the periodic impact with the transverse members: the front of the test-section and the four frames. The impact is, however, not exactly periodic in time because the ship slows down. This explains this wide frequency band instead of one single peak at 2 Hz. For both signals from the load cells there are only frequencies higher than 15 Hz with very small amplitude. But this is not the case for the acceleration signal. This signal shows higher frequencies of around 17, 23, 35 and 130 Hz. These frequencies are only registered by the accelerometer, which is around

30 m away from the impact location. This fact indicates that these frequencies are not bound to the test-section. Higher frequencies of lower amplitude indicate local vibration (tertiary structure), while lower frequencies indicate global vibration (primary and secondary structure: ship hull or the test-section as a whole). The highest frequencies (110 – 148 Hz) could therefore indicate that the accelerometer is vibrating locally.

Table 2 Observed frequencies in both amplitude spectra (from high to low intensity)

	Force from acceleration signal		Force from load cells test-section		Force from load cells rock	
	Range (in Hz)	Mean (in Hz)	Range (in Hz)	Mean (in Hz)	Range (in Hz)	Mean (in Hz)
1		0.4	0.0 – 0.8	0.4	0.0 – 0.8	0.4
2	1.6 – 2.8	2.2	1.6 – 2.4	2.0	1.6 – 2.4	2.0
3		3.6		3.6		3.6
4	4.8 – 5.6	5.2	4.8 – 5.6	5.2	4.8 – 5.6	5.2
5	6.0 – 15	10.5	6.0 – 15	10.5	6.0 – 15	10.5
6	15.2 – 19.6	17.4				
7	20.4 – 26.4	23.4				
8	30.8 – 38.4	34.6				
9	110.4 – 148.4	129.4				

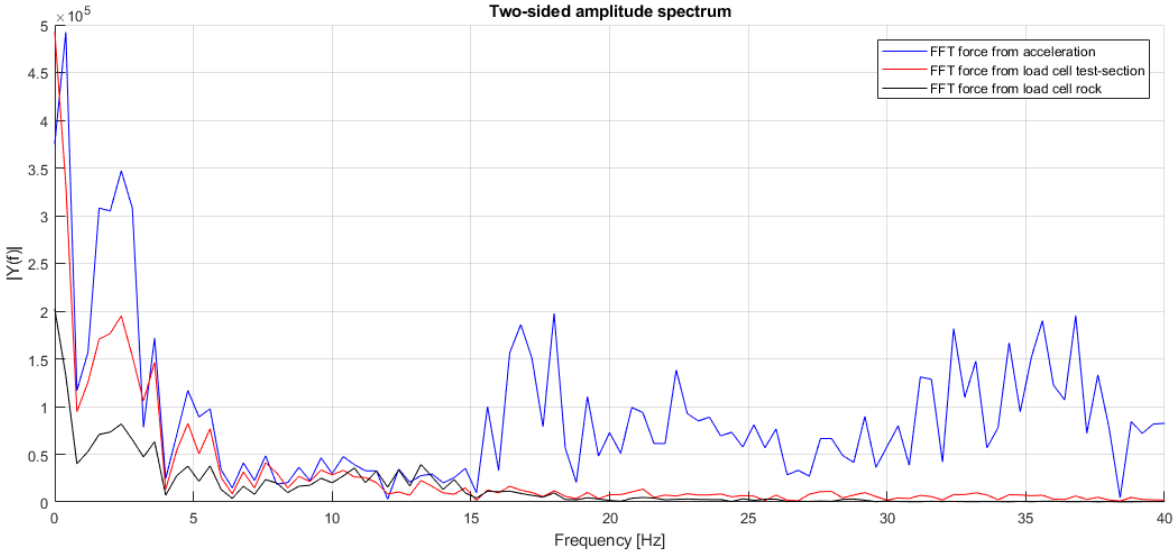

Figure 29 Close-up of the FFT amplitude spectra of the longitudinal force signals

Eigenfrequencies

In order to be sure about the frequencies higher than 15 Hz being not related to the test-section, a calculation of the eigenfrequency of the test-section is performed. The test-section is supported onto the support ship by the transducers/load cells, depicted in the top view of the test-section in Appendix B. The peaks of 17 and 35 Hz could also indicate the eigenfrequencies of the test-section, vibrating horizontally as the rock excites it. For simplification, the test-section can be viewed as a mass-spring system, connected to a rigid support ship. The mass of the test-section is 10.30 t (Table 3). The stiffness of one load cell can be simplified to Equation 3 using data on the load cells from Appendix B. The eigenfrequency of the test-section is then calculated with Equation 4. The factor 4 is used here because there are four longitudinal load cells.

$$k = \frac{EA}{L} \tag{3}$$

$$f = \frac{1}{2\pi}\sqrt{\frac{4k}{m}} \tag{4}$$

One longitudinal load cell is around 1200 mm long and has a diameter of 60 mm. An elastic modulus of 210 GPa is assumed (ASTM-A36 steel). The stiffness of one load cell is then 495 MN/m. With this data and Equation 4 the eigenfrequency of the test-section is 69.77 Hz. This can indicate a multiplication of the 17 and 35 Hz frequencies, which indicates an eigenfrequency. But in Figure 27 this frequency cannot particularly be observed. This can be because this frequency was not excited by the rock force.

The exact opposite is done using this equation: now take the mass of the ship minus the test-section, which is 670.44 t, as the vibrating mass. The eigenfrequency of this system is 8.65 Hz. This frequency is not observable in the amplitude spectrum as well, for probably the same reason.

It was assumed that the support ship was rigid, but what if the mass of the support ship has a part in the system? The supports ship plus test-section is viewed as a free (suspended in water, water neglected) two mass system connected by four springs. The added mass of the water is neglected. The eigenfrequency for such a system is calculated with Equation 5.

$$f = \frac{1}{2\pi}\sqrt{\frac{4k(m_1 + m_2)}{m_1 m_2}} \tag{5}$$

The mass of the test-section is 10.30 t (= m_1). The mass of the ship (minus the test-section) is 670.44 t (= m_2). The eigenfrequency of this system is 70.30 Hz. This is almost the same value as calculated from Equation 4 using the one mass-spring system, because the mass of the support ship is much larger than the mass of the test-section.

Of course, in the experiment it was also assumed that the rock is rigid, but in reality this is not entirely the case. Also, the pontoon on which the rock was mounted on could have moved along the waterbed on the high impact with the ship, making the rock move as well. However, making a good estimate of how the rock and pontoon behaved in the situation is more difficult. For now it is still assumed that the rock is rigid and the pontoon remained static. The former because the rock was completely filled with concrete and the latter based on the information that after finishing the tests the pontoon was very difficult to remove from the waterbed after being stuck there for over a year.

Sloshing

A quick study is done on the sloshing frequencies of the liquids in the ballast tanks. Can the effect of sloshing explain some frequencies in the frequency spectra? An overview of the masses of the liquids in the tanks is given in Table 3. The largest volumes of liquid can be found in tanks II and tanks VI. In the report only the volumes of the tanks is given and not the area nor the height. The mean volume inside the PS and SB tanks II is 23.65 m^3 and the mean volume of PS and SB tanks VI is 106.80 m^3. The dimensions of the PS and SB tanks II are 10.75x1.22 (LxB) and those of the PS and SB tanks VI are 9.5x4.7 (LxB).

The quick analytical equations for the natural frequency of the liquid in a rectangular tank in horizontal excitation is used from Li & Wang [25]. The height of the fluid column inside the tanks is estimated by taking the volume from Table 3 (mass in tonnes is volume in cubic meter for ballast water) and dividing it by the length and width of the tank. The height of the

fluid column in the PS and SB tanks II is this way estimated at 1.80 m and the height of the fluid column in the PS and SB tanks VI at 2.39 m. The first symmetric and antisymmetric natural sloshing frequencies of the tank contents in longitudinal direction are calculated for all tanks. In the paper's method, the geometry and coordinate system for the cross-sectional oscillation are taken from the middle of the tank in longitudinal direction (x = 0 at L/2), so that all modes of oscillation are either symmetric or antisymmetric in x (this is pictured in Figure 30).

The natural sloshing frequencies calculated from the analytical formulae in the case of a rectangular tank is for the tanks II: $f_{symm} = 0.34 \pm 0.02$ Hz and $f_{asymm} = 0.19 \pm 0.01$ Hz, and for tanks VI: $f_{symm} = 0.39 \pm 0.02$ Hz and $f_{asymm} = 0.23 \pm 0.01$ Hz. (The uncertainty parameter comes from a 5% accuracy. In the study the first three antisymmetric and symmetric frequencies are within 5% accuracy compared to other analytical, numerical, and experimental values.) The frequencies are almost identical because of the almost equal tank length (is the most significant parameter in a longitudinal motion). The height of the fluid column was assumed. To test how this influences the analytical solution the height is varied. An increase of fluid column height of 200% gives for the sloshing frequencies of tanks II: $f_{symm} = 0.38 \pm 0.02$ Hz and $f_{asymm} = 0.24 \pm 0.01$ Hz, and for tanks VI: $f_{symm} = 0.40 \pm 0.02$ Hz and $f_{asymm} = 0.27 \pm 0.01$ Hz. This is only a small frequency increase, so the solution of the analytical formulae would not get influenced much by a wrong assumption of the fluid column height.

The asymmetric first natural frequency of the sloshing could explain the high intensity peak around 0.5 Hz in Figure 29. The sloshing of the liquid in tanks VI would have more impact in the amplitude spectra because of its larger volume (total mass of all of its tank contents is almost a third of the light ship) than the sloshing in tanks II. But, this statement is not entirely true. Because in the report it is not specified how much the tanks are filled (i.e. partially or full). It could be that tanks VI are completely filled and tanks II are not, yielding that the sloshing effect of tanks II has more influence (because of larger free surface). The analytical formulae specify only a certain fluid column height in a tank with an unspecified height.

Table 3 Loading condition

Light ship	379.00	[t]
FW	2.80	[t]
Fuel II SB	2.70	[t]
Cofferdam	14.00	[t]
Tank VI SB	108.80	[t]
Tank VI PS	104.80	[t]
Tank II SB	22.00	[t]
Tank II PS	25.30	[t]
Portal	11.04	[t]
Test-section	10.30	[t]

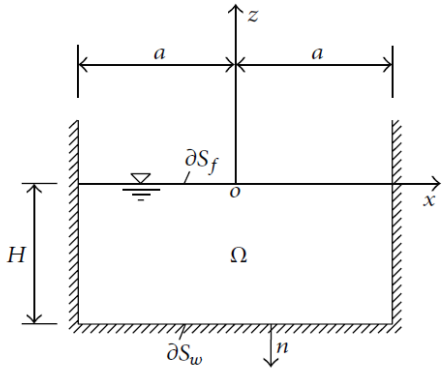

Figure 30 A rectangular tank (figure 2 of Li & Wang [25])

3.3.2. Wavelet transform

More types of signal identification besides Fourier transform have been studied. This has been done because of the nature of the surge acceleration signal. The signal is more transient, and there is an abrupt beginning and end to the signal (impact).

The whole surge acceleration time-trace and the whole surge force from load cell signal are analysed instead of just the grounding part (as is done with the FFT). This is permitted because the wavelet transform looks at the signal step by step in time, so the measurement of the impact with the buffer cannot contaminate the transform. The Fourier transform, however, looks at the signal as a whole as a sum of sinusoids. The signal has been subjected to the continuous wavelet transform (CWT). The chosen mother wavelet is a Morse wavelet. This wavelet resembles the signal. The importance of choosing a wavelet is discussed in Appendix E. The Morse wavelet also gives the best results when using CWT. The results are shown in Figure 31 and Figure 32. The left picture shows the scalogram and the right the contour map of the transformation for a clearer view of the results. The scalogram shows the frequency on a logarithmic scale and the magnitude of agreement with the signal is indicated in colour (blue is low, yellow is high). The grey area outside the dashed white line in the scalogram delineate regions where edge effects are significant (this means that wavelets of certain width cannot fit the edge of the signal nicely, that is why the grey area is wide at the bottom and small at the top). Also, the happenings during the grounding are marked in the left picture, in order to better assess when these frequencies are observed during the test. Again: green indicates the rock touching the front of the test-section, magenta indicates rupture, black indicates impact with the buffer. In Table 4 and Table 5 the frequencies from the contour plots are noted.

Surge acceleration signal

The frequencies in Figure 31 and Table 4 are compared to results from the Fourier analysis. It can be seen that the most prominent frequencies observed from the scalogram are between 29 - 48 Hz on t = 0.81 s. At t = 1.28 s the frequencies range from 29 – 41 Hz and at t = 1.68 s the frequency is 37 Hz. These agree with the range and mean frequency observed from the Fourier analysis (Figure 27 and also to the close-up in Figure 29). The higher frequencies found in these figures, in the range of 110 to 160 Hz, are recognizable in the scalogram as well. Also, now the analysis is performed in the time domain as well, it is interesting to see that the frequencies seem to occur just after plate rupture (magenta lines). A delay after rupture is seen for both the low and high frequencies and are tabled in Table 4 as well (fifth column). A delay of the >100 Hz frequencies of around 0.08 s is seen after every 35 Hz peak (sixth column). Sliding of the ship over the rock occurs between t = 1.5 s and t = 2.6. In this time span the 35 Hz seems to disappear or become less prominent with respect to earlier in the signal. This could indicate that the 35 Hz frequency can result from the structure vibrating from rupture of the hull, which does not happen during sliding. The higher frequencies indicate a very local vibration of for example the point where the

accelerometer is mounted on, which could be the response of a compression wave traveling through the ship towards the accelerometer location, hence the delay. A wave traveling through structural steel (speed of sound through steel, $V_1 = 4512$ m/s) over around a 30 m distance yields a frequency of 150 Hz. This substantiates this hypotheses.

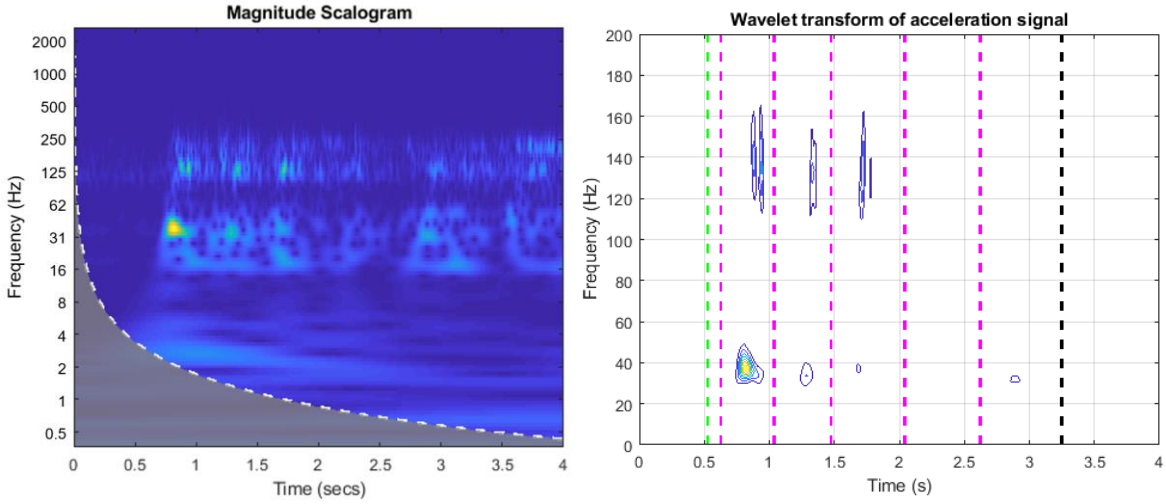

Figure 31 Continuous wavelet transform of acceleration signal and interesting moments during the grounding. Green: first contact with rock. Magenta: rupture of plate. Black: impact rock in buffer.

Table 4 Frequencies from CWT plot in chronological order

Moment of rupture [s]	Time [s]	Frequency range [Hz]	Mean [Hz]	Delay from rupture (s)	Delay from first frequency (s)
0.63					
	0.81	29-48	39	0.18	
	0.89	120-163	142	0.26	0.08
	0.95	116-165	141	0.32	0.14
1.04					
	1.28	29-41	35	0.24	
	1.33	110-154	132	0.29	0.05
1.48					
	1.68	36-38	37	0.20	
	1.72	109-165	137	0.24	0.04
	1.78	120-140	130	0.30	0.10
2.04					
2.62					
	2.89	31-33	32	0.27	

Surge force from load cells

The frequencies in Figure 32 Table 5 are compared to results from the Fourier analysis. The CWT plots show that the lower frequencies cover a large part of the time-trace (after t = 4 s the force signal is zero). This is understandable because these lower frequencies have a period in the order of seconds. The frequency with the highest magnitude (yellow) is around 3 Hz (last row in the table) and occurs just after the impact with the rock (with a delay of 0.23 s). A frequency of 10.5 Hz is observed, which is traced back to the FFT. This frequency only occurs upon first impact. Each impact with a transverse

member in the surge force signal has a smaller impact than the previous impact because the ship is decelerating. The CWT also shows a smaller magnitude as the force signal 'decays', just as is seen in the CWT contour plots for the decaying signals in Fig. 5., Appendix E.

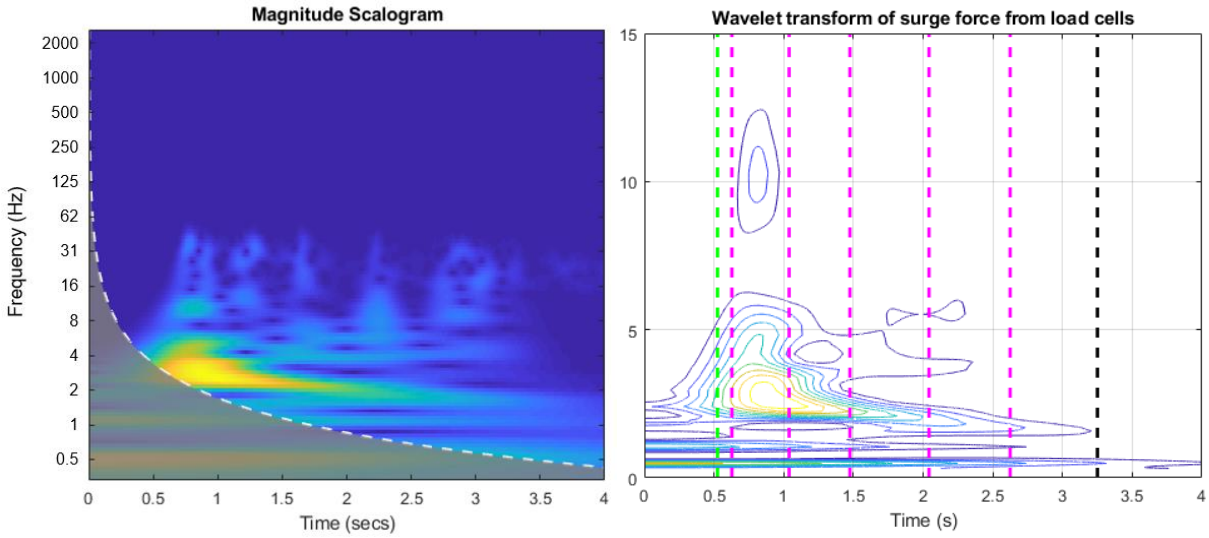

Figure 32 Continuous wavelet transform for surge force from load cells and interesting moments during the grounding. Green: first contact with rock. Magenta: rupture of plate. Black: impact rock in buffer.

Table 5 Frequencies from CWT plot in chronological order

Time [s]	Frequency range [Hz]	Mean [Hz]	Delay from rupture (s)	Comment
0.00-4.00	0.3-0.6	0.5	-	
0.00-2.80	0.9-1.3	1.1	-	
0.83	8.4-12.6	10.5	0.17	
0.89	2.0-6.3		0.23	Measured in most wide part
0.89		3.0	0.23	Measured in centre of part with largest magnitude

Bending frequency

Using the wavelet theory, the frequency of the bending of the test-section will be looked at. In order to do this, the forces measured in the four vertical load cells will be looked at. Appendix B shows that the four vertical load cells are positioned at each of the corners of the test-section. In order to investigate the bending of the test-section as a whole, the signal of the vertical force with respect to time measured by the load cells in the back of the test-section will be compared to the those measured by the ones in the front. The vertical force for each pair of load cells is plotted in Figure 33. Here the impact with the front of the section and the four bulkheads is clearly visible when the signals are combined. It is assumed that the force is proportional to the vertical displacement. The plot shows how first the front of the test-section is lifted and while the rock progresses towards the back in time, the backside is lifted. At t = 3.2 s the rock leaves the test-section.

A CWT of the vertical force signal of the back and the front load cells is created in order to investigate the frequency at which the sides go up and down. The result of the CWT is shown in Figure 34. In the left scalogram (front load cells) the frequencies are around 0.5 Hz, 1.0 Hz, and 3.5 Hz. The right scalogram (back load cells) show frequencies of around 0.5

Hz, 1.0 Hz and 1.9 Hz. This analysis could explain the low frequencies seen in the surge signal analysis. The impact with the rock could explain the low frequency: a bending motion of the test-section in its mount.

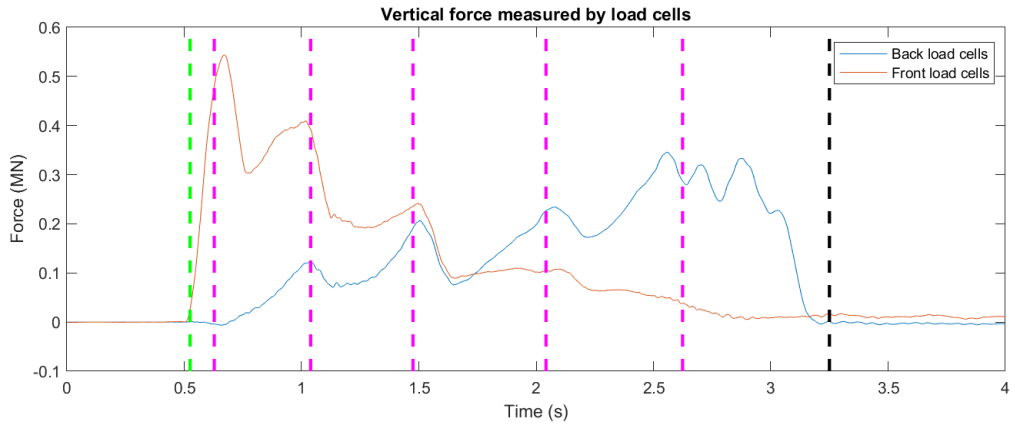

Figure 33 Vertical force measured by the load cells in the front and the back of the test-section and interesting moments during the grounding. Green: first contact with rock. Magenta: rupture of plate. Black: impact rock in buffer.

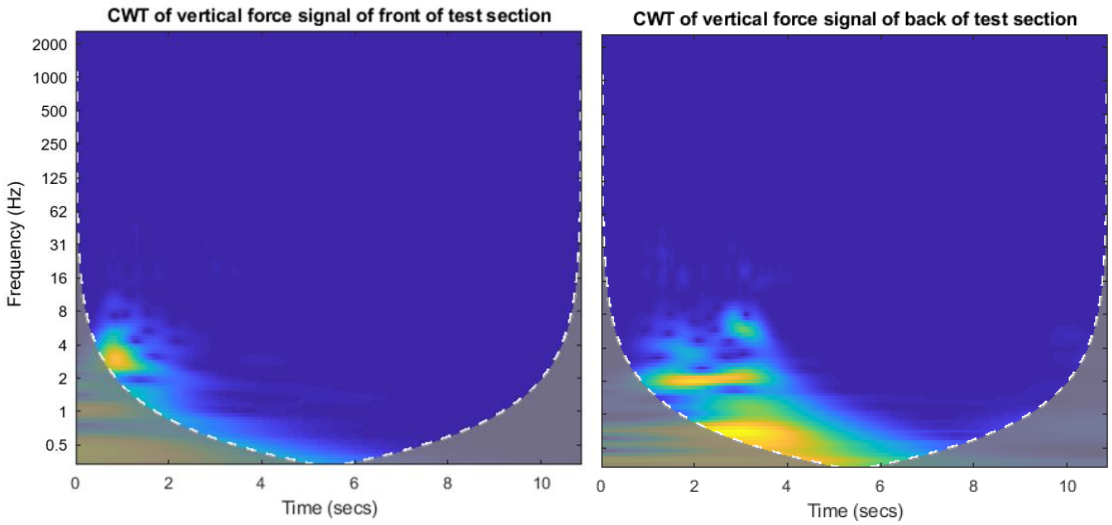

Figure 34 Scalogram of the vertical force signal. Left: Front load cells. Right: Back load cells.

3.3.3. Hilbert transform

The study in Appendix E also investigates another type of signal identification: the Hilbert transform (HT). This transform also looks at the signal in time. But unlike the continuous wavelet transform, it finds the instantaneous frequency at every timestep. In Figure 35 the transform of the acceleration signal is shown. The blue line shows the instantaneous frequency and the coloured lines show the smoothed instantaneous frequency using different window sizes in order to give a better view of the frequency at each moment in time. The left picture in this figure shows the smoothed data (with largest moving average filter span) and some extra information. Here, just as in Figure 31, the interesting moments during the grounding are indicated using vertical dashed lines. Again: green indicates the rock touching the front of the test-section, magenta indicates rupture and black indicates impact with the buffer.

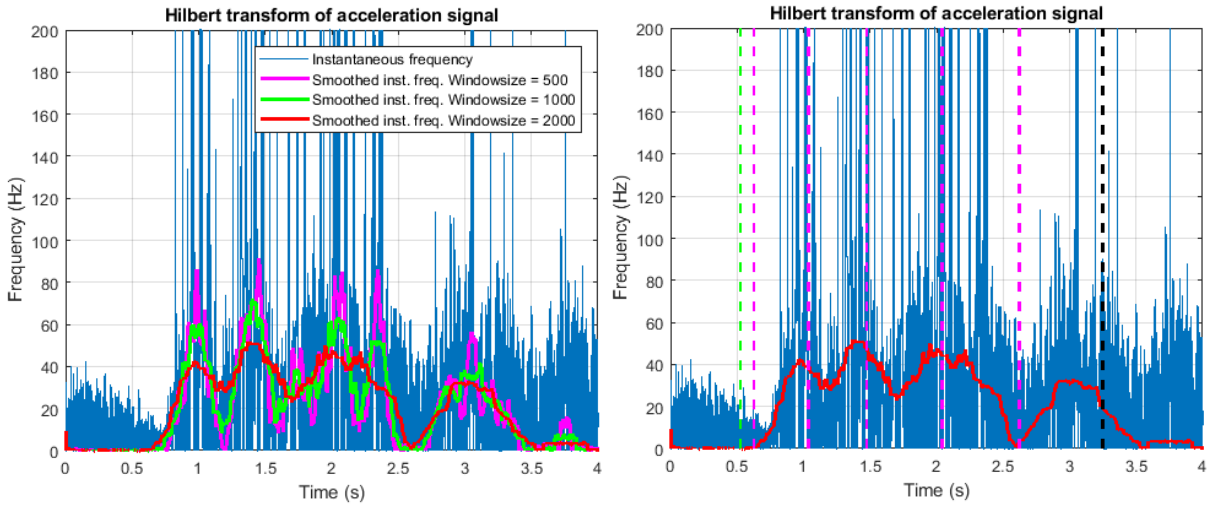

Figure 35 Left: Hilbert transform of acceleration signal. Right: same signal but indicating interesting moments during the grounding.

From the figure can be seen that pointing out the exact frequencies is harder to do using such a noisy signal than in a very clear signal as in the small signal identification study in Appendix E. The frequencies are compared to the frequencies obtained by the continuous wavelet transform in Figure 31. In Figure 31 the highest magnitude frequencies are found at t = 0.81 s with frequencies ranging from 29 - 48 Hz, at t = 1.28 s ranging from 29 - 41 Hz and at t = 1.68 s it is around 37 Hz. But the frequency in Figure 35 at t = 0.81 s is 21 Hz. At t = 1.28 s the frequency is 38 Hz, which falls in this range and lastly at t = 1.68 s the frequency is around 25 Hz.

What is more is that, using wavelet theory, one is able to distinguish multiple frequencies in a timestep. HT cannot do that because it calculates one frequency at a timestep. Therefore it is concluded that the Hilbert transform is not the most ideal way to analyze this complex signal and multi-frequency signal.

3.3.4. Conclusion

The signal identification using three different methods points out that Hilbert Transform is not the most ideal way to analyze this complex signal. Up until 15 Hz both the load cells at both rock and ship and the accelerometer measure the same frequencies. This shows that these frequencies are bound to the test-section/ship. It also concludes that the accelerometer is able to determine the same frequencies as the load cells and can be used as a replacement for the load cells. Higher frequencies and of high intensity are only visible in the surge acceleration signal. This shows that higher frequencies than 15 Hz are bound to the local structure at midship where the accelerometer is placed. The 2 Hz frequency indicates the impact with the five transverse members. This is observed by the load cells and the accelerometer.

3.4. Absorbed energy

Now it is investigated how much energy is absorbed during the test by the system. Literature shows that this method is interesting when looking at how this relates to the damage [24]. The absorbed energy is calculated by two methods: only using accelerations and using the force-path data. This investigation is performed to find out if it is possible to use the accelerations on its own as a replacement of using the force signal. The two methods are:

- Acceleration signal times the assumption of a constant ship mass during grounding (M = 680.74 t) results in a force in surge. The acceleration signal is integrated in time twice to receive the path in surge. The force signal is than integrated to this path and results in the cumulative energy in time or path. The absorbed energy function now only relies on the data acquired by the acceleration measurements. The calculation is done using Equation 6. The integration is done over the whole (time)signal.

$$E = \int M\ddot{x}\, dx \quad \text{with, } dx = \left\{\int_0^t \ddot{x}\, dt\right\} dt \tag{6}$$

- The force measured by the load cells is integrated over the path measured by the wire gauges in surge. This results in the cumulative energy in time/path and is calculated using Equation 7. The integration is done over the whole (time)signal.

$$E = \int F_x\, dx \tag{7}$$

The result of both calculation methods is shown in Figure 36 (energy - time) and Figure 37 (energy - path). This shows that the total absorbed energy computed from the acceleration signal is much higher. The figure shows that at t = 3.3 s and x = 7.5 m, the rock collides into the buffer and all the residual kinetic energy of the ship is absorbed by the foam. The initial ship speed was 3.73 m/s. The initial kinetic energy is therefore 4.74 MJ. The absorbed kinetic energy by the foam is 1.43 MJ (= initial kinetic energy – final cumulative energy from load cells). The initial kinetic energy is also observed from the energy calculation derived from the acceleration signal. This is expected, because this much energy should be dissipated if the ship was to come to a complete halt from its initial speed.

In the energy – path figure the spacing between floors can be recognized in both absorbed energy plots: every 1.25 m the energy absorption rate decreases for a moment. The length of the test-section is 5.5 m, which is also observed in the energy derived from the measured force. No more energy gets absorbed (blue line) when the rock passes the test-section and is in the free space between the test-section and the buffer (Figure 16). This is because no force is measured anymore, but the wire gauge continues to measure displacement until the rock collides into the buffer. It explains why the difference between the final value of the red and the blue line is the absorbed energy by the buffer.

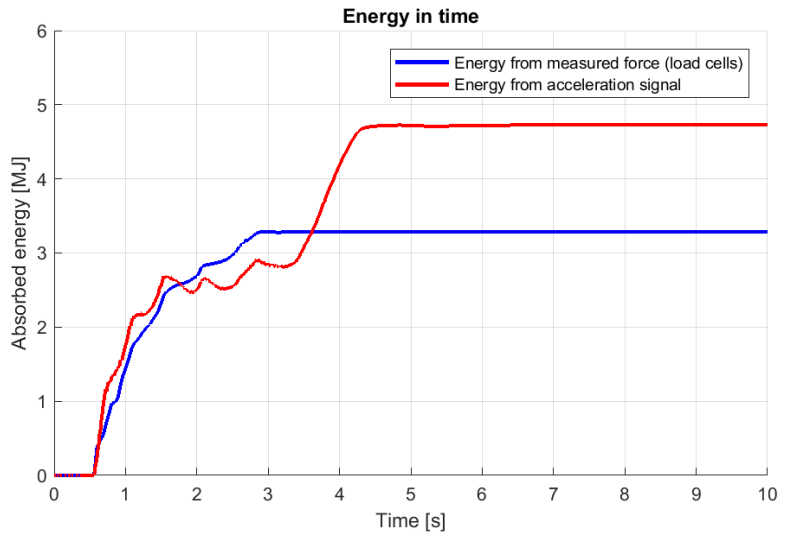

Figure 36 Energy plotted against time for both the energy derived from the acceleration signal and the measured force.

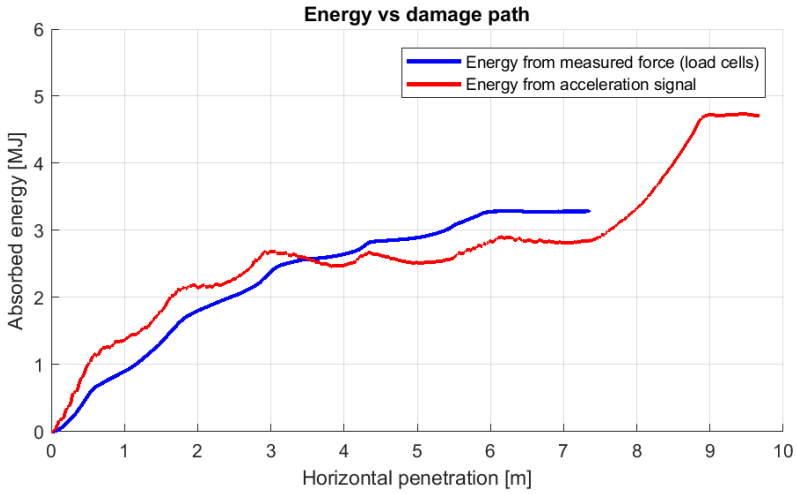

Figure 37 Energy plotted against horizontal rock penetration for both the energy derived from the acceleration signal and the measured force.

In order to make the analysis of the relation of the absorbed energy to the damage path easier, a better view of the absorbed energy is made. The same plots of Figure 37 are presented in Figure 38, but they are presented together with the bottom view of half of the test-section + buffer including the damage: the deformation and tears are pictured as well. The deformation path is shaded and the tears are outlined. This is the same bottom view as is pictured in the damage report in Appendix A. And finally the trim angle is plotted in the figure as well. The dimensions of the bottom of the test-section are 5.50x5.50 m.

The grounding starts when the front of the rock hits the front of the test-section (left side of the test-section in the picture). At this point the energy of the system is absorbed by deformation of the structure. This however already happens when the rock tip has not reached the section yet but already begins when the rock first hits the structure (that is why the front of the test-section is not set to zero). Next, the rock continues to penetrate the test-section: the energy is absorbed by the structure by deformation until rupture of the plate just in front of the rock tip. After that, the rock meets the first transverse frame and the resistance of the structure starts building up again and so does the energy accumulation (seen from the increase in energy accumulation of the blue line). This continues until rupture of the plate ensues again.

While penetrating the test-section, the ship is lifted and starts pitching. It can be seen that when the rock passes a floor it drops through the hole and the trim angle increase slows down for a moment (around x = 1 m, x = 2 m and x = 4 m). When the rock meets the second frame (x = 3 m) the ship is lifted and this causes the ship to slide over the rock. Thus, at this point rupture stops (just in front of the bulkhead because of high structural resistance) and the trim angle becomes steady. Deformation of bottom continues but is now only around the size of the rock tip as can be seen when comparing this to the rock in the picture (this can be observed in more detail in the damage report in Appendix A). Because of the sliding, the energy absorption rate is quite low at this moment during the grounding. When reaching the third bulkhead (x = 4.3 m), the ship is too heavy to be lifted by the rock on only a small area and the bottom ruptures. When this happens the trim angle also declines. The rock is free in between the end of the test-section and the buffer and therefore no energy can be absorbed. Also here the trim angle declines even more.

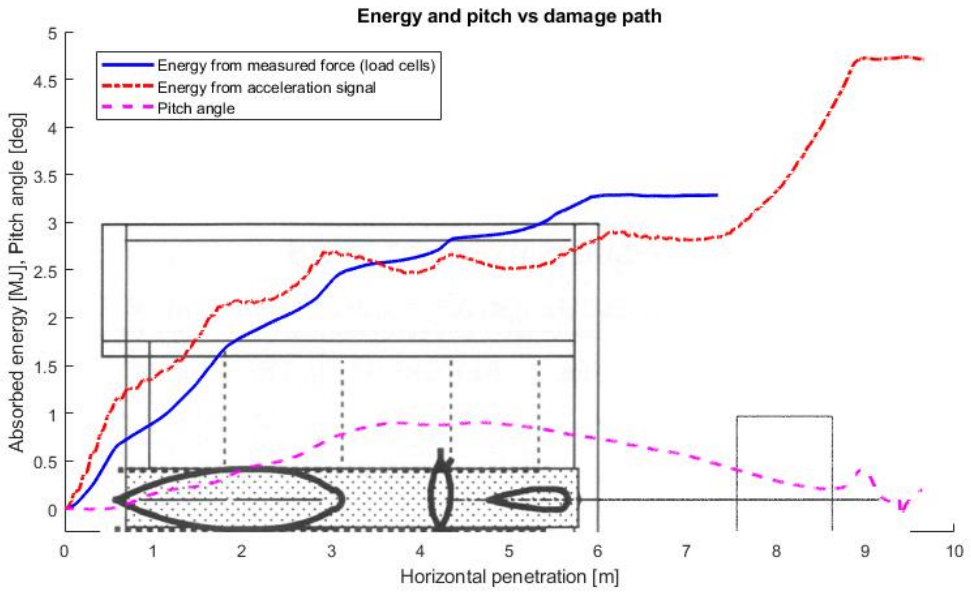

Figure 38 Energy plotted against horizontal rock penetration, the trim angle and plotted on the bottom view + buffer with damage (three tears) of Appendix A. The left side of the test-section is the front and is the location of impact.

A factor that influences the energy calculated from acceleration data is the ship's inertia. From Figure 38 is observed that the absorbed energy calculated using the acceleration signal and the absorbed energy calculated from the force do show the same trend but do not coincide completely. The total mass in surge in the experiment has been determined at 681 tonne (from the experiment's report). The line of the absorbed energy from acceleration shows an overestimation of the energy in the first half of the figure (up to 3 m) and an underestimation in the second half. The variation of estimated ship mass contributing in the ship motion can be physically explained by sloshing and hydrodynamic effects (added mass). Sloshing is present because of ballast water in the tanks that is used to trim the ship to its initial trim angle before impact and the fuel. Not all of the tank contents is initially 'felt' dynamically in the surge motion (leading to a difference in absorbed energy), because of the effect of sloshing in the partially filled tanks. From the loading data of the experiment in Table 3 it is observed that 43% of the total weight is tank contents of any sort. It is not reported which tanks were partially filled however, but a maximum weight of 291 tonne could contribute to it. A minimum of 410 tonne total effective weight in the first part of the grounding and a maximum of 971 tonne effective weight in the second part of the grounding is how large the uncertainty in the weight estimation can be. The time-varying added mass is another factor that influences the signal. The ship undergoes a decrease in speed upon impact, the added mass does not at the same rate.

3.5. Conclusion

In this chapter the following question was posed: *How can acceleration time-traces be related to damage?* In order to answer this, an analysis of the accelerations measured during TNO's large-scale grounding experiment has been carried out. Some conclusions can be drawn.

It is seen that in the case of the large-scale grounding test one is able to observe from the acceleration signal in surge how the structure reacts to the contact with the rock. The placement of the accelerometer far away from the impact location does not have a negative influence on the response. But, the signal does not say anything about to what extent the response is damped or deformed due to the ship structure. The signal in one direction is not influenced much by one in another.

When assuming the grounding as a one DoF problem, a double integration of the acceleration signal in surge serves as a quick assessment of the damage length. This assessed damage length is longer than measured by the wire gauge. This is because of the impact with the buffer. Up until the impact with the buffer, good agreement with the damage length is found. This means that the velocity up to moment of buffer impact is agreeable as well.

Up until 15 Hz both the force and acceleration signal in surge direction contain the same frequencies. This shows that these frequencies are bound to the test-section/ship. Frequencies higher than this and of high intensity are only visible in the surge acceleration signal. This shows that higher frequencies than 15 Hz are bound to the accelerometer at midship, but do not have much relevance to the response of the test-section. The analysis also shows that sloshing may have a large effect on the measured accelerations. The 2 Hz frequency indicates the impact with the five transverse members.

From the absorbed energy a lot can be learned about the raking damage. The lines of absorbed energy calculated using the force from load cells and the absorbed energy calculated using accelerations in surge are compared. While using only accelerations in surge and estimating a constant ship mass, good resemblance is found between the two methods. The absorbed energy is related to the reported damage and the trim angle. It is found that when the energy absorption rate increases, there is more deformation. And just after rupture, the energy absorption rate decreases because of lost structural integrity and resistance. This causes that no energy can be dissipated by deformation or failure. The absorbed energy figures show that the acceleration time-traces can be used to tell how much deformation is present at that moment in time relative to anywhere else in the signal, when rupture occurs and at what time and distance this happens. Using accelerations, information can be extracted on the damage and the location of the damage on the ship bottom. This information can be used to tell how many frames are met on the way of the rock penetrating the ship bottom and could serve as an indication of how many compartments are involved in the damage. In order to make a more solid assumption about this, a calculation model is made in the next chapter.

4

Damage calculation model

The grounding of the Transocean Winner. August 8, 2016. The Hebrides, Scotland.

4.1. Methodology

In Chapter 3 an analysis of the accelerations measured during TNO's large-scale grounding experiment has been carried out. Here, the sub-question elaborated on how accelerations can be related to damage in a grounding. It is found that accelerations tell something about the extent of the raking damage on the ship bottom. It shows the attractiveness of using accelerations for this damage assessment. Now, the second part of investigation is started to investigate the other aspect of the raking damage assessment: the location of the damage. In order to do this, a model will be implemented to find out if accelerations can indeed be used to make an assessment of the damage and the location of the damage on the ship bottom.

In a real grounding incident, the size of the rock and the location of the first impact with the rock is not known. This is hard to model. Also, it is hard to verify the model like that and validate its results. To make the step easier, first is assumed that the location of impact with the rock on the ship bottom is known and the forces at the rock acting on the ship are as well. This approach is visualized in Figure 39. The model relies of three input variables and generates the accelerations measured on board and the damage path resulting from this grounding force. Therefore, the sub-question that will be answered in this chapter is:

What is the damage path resulting from grounding force?

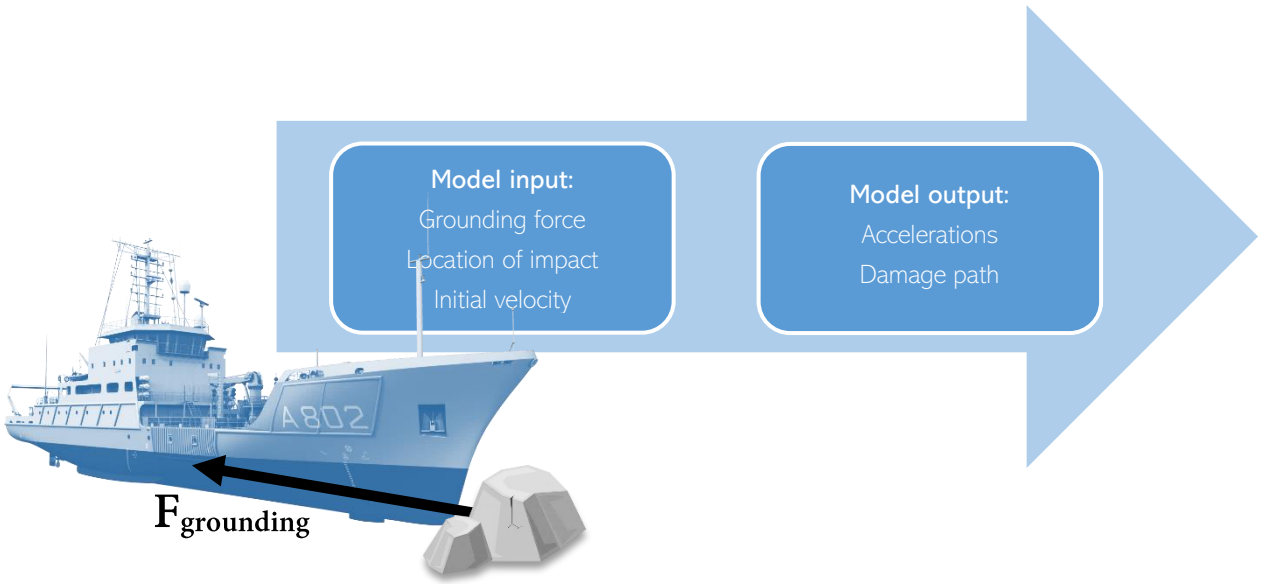

Figure 39 Visualization of the model's approach

From the literature study various methods are found intended to calculate the damage resulting from ship grounding ([2], [11], [16], [17] and [18]). The main idea behind these methods are different. As discussed in the literature study, the *why* for each researcher differs. Some methods are made in order to be used by a ship designer in order to give him a tool to make a quick assessment of his structure's resistance in an accident. Others' methods are made as to give a tool to post-process a grounding scenario. In this study, the method must be used just after the incident. This calls for a simple and quick method. Most of these methods exploit the easiness of empirical formulas in order to avoid the use of FEA. They predict a ship's hull strength in a grounding event using only hand calculation. Some of the methods are also very useful in analyses where not much information regarding the detailed ship structure is available. But for some, knowledge of the size

of the rock is still necessary. In this study's calculation model the use of detailed and time-consuming calculations must be avoided, because an assessment of the dangerous situation must be done quickly. The calculation model should work with only the ship's main dimensions and general structure.

The model is made in MathWorks' Matlab & Simulink. This program is chosen for its available functions and its very visual and understandable workflow.

4.1.1. Frame of reference

First, the degrees of freedom for the grounding model is determined. In section 3.2.4 the problem has already been looked at in one DoF. The motion which is most important for determining the raking damage when the ship is sailing normally is surge. Also, for answering this chapter's sub-question, the damage path must be found. The horizontal plane motions: surge, sway and yaw, are looked at in order to find this. For this, a constant vertical rock penetration is assumed, so no heave, roll and pitch motions will be modelled. The model is therefore looked at in 3 DoF in the horizontal plane.

The problem is modelled as a ship with certain initial speed in surge direction and impacting with a rigid rock at t = 0 at a certain point away from the ship's CoG. In order to model this the problem is viewed in a local and a global coordinate system. It is modelled this way so that both the global ship motions and the local rock contact path can be viewed clearly. The local system, xyz, is fixed to the ship's CoG. The global coordinate system's origin, XYZ, is fixed to the rock. The local coordinate system is always viewed in the global coordinate system. The coordinates of the local origin in the global system is $(X_s, Y_s) = ((x, y) = (0,0))$. The vector depicting the local displacement of the ship is $[u\ v\ \psi]^T$, with u the displacement of the ship in surge, v the displacement of the ship in sway and ψ the rotation of the ship around its vertical axis, yaw. The position vector of the local coordinate system in the global system is $[X\ Y\ \psi]^T$, where X and Y are the translations of the local system in the global system and ψ is the orientation of the local system in the global system. This is also the yaw rotation, ψ, which are the same in both coordinate systems.

Figure 40 shows a simplified representation of the local (ship's CoG) coordinate system in the global (rock) coordinate system. Here the ship is first presented before impact and then it is presented after impact with the rock. The figure depicts the ship hitting the rock off-centre (this is indicated by the distance perpendicular to CL, μ). An off-centre impact results in a yaw angle and also makes that the damage path is not straight (as it would in one DoF). The deviation of this curved damage path from a straight line at moment t is the parameter δ.

The approach uses a certain grounding force at the rock acting on the ship bottom. For this horizontal plane model only the horizontal component of the grounding force, F_G, is needed and is for now assumed constant throughout the entire grounding. From literature is found that this force is assumed to be in the opposite direction but parallel to the relative velocity between the ship and the rock in the global coordinate system [2]. In this reasoning the detailed bottom structure of the ship is neglected. It is discussed in section 3.2.2 that the rock tends to follow the path in between longitudinal stiffeners. In fact, longitudinal structural members will give resistance to the rock moving in transverse direction. This assumption will therefore make for a worst case deviation from straight damage path.

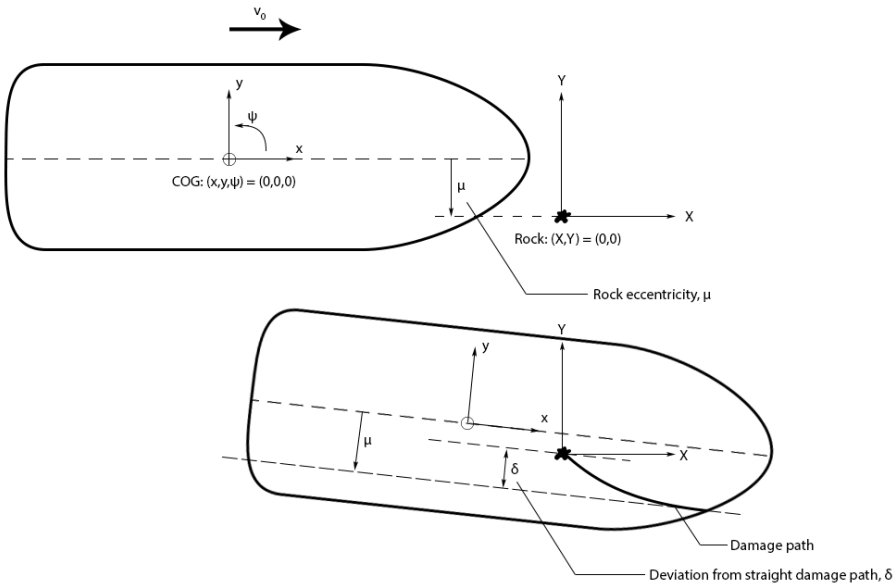

Figure 40 Representation of local (ship's CoG) in global (rock) coordinate system. Pictured just before and after grounding with the rock. (Based on Figure 7.1 in [2])

4.1.2. Equation of motion

The behaviour of the ship is modelled by using the equation of motion of a ship in water with 3 DoF: surge, sway and yaw. Because the problem is viewed in this plane, all hydrostatic restoring coefficients are zero [26]. The damping coefficients are neglected for simplicity's sake, meaning that the ship does not dissipate kinetic energy through the generation of waves. Determination of these coefficients requires detailed information on the hull. It is learned from literature that for the short duration of an event such as grounding this is negligible [21]. The internal mechanics will be ignored for now. The ship will therefore be assumed as a rigid body with general dimensions (length, beam). With this, every general dimension can be used as input, modelling any ship of any material. The external forces will amongst others consist of the rock force acting on a certain point of the ship. The equation of motion is solved in the local coordinate system at the point of the ship's CoG and is given in Equation 8 [2], [27]. Although other external forces acting on the ship are not in the equation of motion, these are cancelled out when choosing a certain grounding force.

$$\begin{bmatrix} M_{xx} & 0 & 0 \\ 0 & M_{yy} & A_{y\psi} \\ 0 & A_{\psi y} & I_{zz} \end{bmatrix} \begin{Bmatrix} \ddot{u} \\ \dot{v} \\ \dot{\psi} \end{Bmatrix} = \begin{Bmatrix} F_x \\ F_y \\ M_z \end{Bmatrix}_{ground} + \begin{Bmatrix} M_{yy}(\dot{v}\dot{\psi} + x_{gy}\dot{\psi}^2) \\ -M_{xx}\dot{u}\dot{\psi} \\ (M_{xx} - M_{yy})\dot{u}\dot{v} + x_{gy}M_{yy}\dot{u}\dot{\psi} \end{Bmatrix} \tag{8}$$

$$\begin{aligned} A_{y\psi} &= A_{\psi y} = x_{gy}M_{yy} = \int_L x\left(m(x) + \mu_y(x)\right)dx \\ M_{xx} &= M + A_{xx} = \int_L \left(m(x) + \mu_x(x)\right)dx = 1.05 \cdot M \\ M_{yy} &= M + A_{yy} = \int_L \left(m(x) + \mu_y(x)\right)dx = 1.4 \cdot M \\ I_{zz} &= I_z + A_{\psi\psi} = \int_L x^2\left(m(x) + \mu_y(x)\right)dx \end{aligned} \tag{9}$$

Inertia

The first matrix on the left-hand side of Equation 8 is the mass and added mass matrix of the equation of motion. With:

M_{xx} = ship mass plus added mass in surge [kg];
M_{yy} = ship mass plus added mass in sway [kg];
I_{zz} = moment of inertia around the ship's vertical axis and the added mass [kg m^2];
$A_{y\psi} = A_{\psi y}$ = couple term between motion in sway and yaw [kg m].

These inertias are determined using Equation 9 ([2], [21], [22], [26], [28]), with:

M = ship mass [kg];
I_z = moment of inertia of the ship [kg m^2];
A_{xx} = added mass in surge [kg];
A_{yy} = added mass in sway [kg];
$A_{\psi\psi}$ = added mass in yaw [kg m^2];
m = ship mass per unit length [kg m^{-1}];
μ_x = added mass in surge per unit length [kg m^{-1}];
μ_y = added mass in sway per unit length [kg m^{-1}].

A constant added mass of 5% of the ship mass (1.05·M) is taken as added mass in surge and a constant 40% of the ship mass (1.4·M) as added mass in sway ([21], [28]). The sway and yaw motions are coupled using the term $x_{gy}M_{yy}$ [kg·m] and is determined using Equations 9. The coupled terms in these neglect the ship's forward speed. The coupled term is when, for example, a force in y-direction is applied on the side of the ship, it will not only sway but rotate as well because the ship is not symmetrical over the y-axis: the longitudinal centre of buoyancy (LCB) is not on top of the longitudinal centre of gravity (LCG). Due to the ship's lateral symmetry (over x-axis), the surge motion is decoupled of the other motions.

Grounding force in local reference frame

The first vector on the right-hand side of the equation is the local horizontal grounding force components, F_x and F_y, and moment, M_z, around the ship's vertical axis due to the impact with the rigid rock. How these local forces relate to the given constant global grounding force F_G is shown in more detail in equation 10. The grounding force includes friction forces and other forces acting on the ship as a result of the rock colliding with the ship bottom.

Fictitious force

The second right-hand side vector in the equation of motion is applied to take into account the Coriolis and centripetal forces. The Coriolis-centripetal term is derived using an energy formulation based on the constant added mass matrix [27]. This added inertia term is formulated using Lagrangian dynamics [29]. The derivation of it is given in Appendix D.

These fictitious forces arise due to the rotation of the local (body-fixed) reference frame with respect to the global (inertial) reference frame and are treated as external loads. The use of the Coriolis-centripetal forces allow the application of Newton's laws (equation of motion) to the local rotating system. The Coriolis force is proportional to the mass of the object and the rotation rate. The centrifugal force is proportional to the mass of the object and the square of the rotation rate.

Grounding force in global reference frame

The grounding forces in the local system are derived from the components of the constant grounding force in the global system using trigonometry.

$$\begin{Bmatrix} F_x \\ F_y \\ M_z \end{Bmatrix}_{ground} = \begin{Bmatrix} F_{G,X}\cos\psi + F_{G,Y}\sin\psi \\ -F_{G,X}\sin\psi + F_{G,Y}\cos\psi \\ F_{G,X}Y_s + F_{G,Y}X_s \end{Bmatrix} \tag{10}$$

The constant grounding force, F_G, is always in the opposite direction of the ship's global relative velocity, V_{rel}, with respect to the rock. Therefore the minus sign in equations 11 and 12. This is done because the components of the global grounding forces are in the same direction as the components of V_{rel}.

$$V_{rel,X} = -\left(\dot{X}_S + Y_S\dot{\psi}\right) \tag{11}$$

$$V_{rel,y} = -\left(\dot{Y}_S + X_S\dot{\psi}\right) \tag{12}$$

$$V_{rel} = \sqrt{V_{rel,X}^2 + V_{rel,Y}^2} \tag{13}$$

Combining equations 11, 12 and 13, the components of the grounding force in the global coordinate system are then:

$$F_{G,X} = F_G\frac{V_{rel,X}}{V_{rel}} \tag{14}$$

$$F_{G,Y} = F_G\frac{V_{rel,Y}}{V_{rel}} \tag{15}$$

With these (global) grounding forces at the rock, the (local) grounding forces and moment at CoG are calculated using Equation 10. The equation is now ready to be solved for the accelerations at the ship's CoG using the initial condition: initial velocity. These local accelerations are transformed to the global accelerations using the following relations:

$$\begin{Bmatrix} \ddot{X}_s \\ \ddot{Y}_s \\ \ddot{\psi}_s \end{Bmatrix} = \begin{bmatrix} \cos\psi & -\sin\psi & 0 \\ \sin\psi & -\cos\psi & 0 \\ 0 & 0 & 1 \end{bmatrix}\begin{bmatrix} \ddot{u} \\ \ddot{v} \\ \ddot{\psi} \end{bmatrix} + \begin{bmatrix} -\sin\psi & -\cos\psi & 0 \\ \cos\psi & -\sin\psi & 0 \\ 0 & 0 & 1 \end{bmatrix}\begin{bmatrix} \dot{u}\dot{\psi} \\ \dot{v}\dot{\psi} \\ 0 \end{bmatrix}$$

$$\begin{Bmatrix} \ddot{X}_s \\ \ddot{Y}_s \\ \ddot{\psi}_s \end{Bmatrix} = \begin{Bmatrix} \ddot{u}\cos\psi - \ddot{v}\sin\psi - \dot{\psi}(\dot{u}\sin\psi + \dot{v}\cos\psi) \\ \ddot{u}\sin\psi - \ddot{v}\cos\psi - \dot{\psi}(-\dot{u}\cos\psi + \dot{v}\sin\psi) \\ \ddot{\psi} \end{Bmatrix} \tag{16}$$

From this, the velocity and position of the ship with respect to the rock as a function of time are calculated through respectively single and double time integration. This global velocity and distance of the ship with respect to the rock are used in order to calculate the relative velocity of the ship to the rock to be used for the next timestep, thus also calculating the orientation of the global constant grounding force, F_G, for the next timestep. The simulation is stopped when the relative velocity reaches zero, $V_{rel} = 0$, meaning the ship has come to a stop. At that moment no force is exerted on the ship bottom by the rock anymore, $F_G = 0$.

4.1.3. Modeling of the problem

Appendix F gives an overview of the three degrees of freedom external dynamics grounding model. The appendix also elaborates on the steps made during the simulation.

Input

During the simulation, the equation of motion is solved for the local accelerations of the ship at CoG at each time step. From this, the velocity and position of the ship as a function of time is calculated through respectively single and double integration in the time domain. Input variables for the damage calculation model are:

- Initial velocity of the ship (before grounding), v_o, [m s^{-1}];
- Rock eccentricity, μ. Orthogonal distance from CL to rock [m];
- Longitudinal first point of impact (FPOI). Measured from FPP. [m];
- Grounding force/approximated stopping distance, d_s, [m]. More about this input variable is discussed in section 4.4.

Output

The simulation yields the local and global displacement, velocities and accelerations in time. It also calculates the shape of the damage path using the global displacement information and the initial rock impact location. The parameter, δ, is used to indicate how much the damage path deviates from a straight line.

Solver

In general, Runga-Kutta integration methods are the first one should try. In MATLAB, this is the function ODE45. For solving very dynamic numerical problems like a car crash or ship collision is normally referred to as 'explicit' method. ODE45 stands for the explicit Dormand-Prince method in the Runge-Kutta explicit solver family [30]. It's a single-step solver, which means in computing $y(t_n)$, it needs only the solution at the immediately preceding time point, $y(t_{n-1})$. The first value is given by the initial velocity. The solver than uses this to iteratively compute the solution $y(t_n)$. For choosing a solver it is advised to start and identify the problem type, e.g. stiffness of the problem. A stiff equation is a differential equation for which certain numerical methods are numerically unstable unless the step size is taken to be extremely small. One can identify a stiff equation if non-stiff solvers, such as the Dormand-Prince method, are unable to solve the problem or are extremely slow. After running test simulations it is found that this is not the case, even when very small time-steps are used. After that it is to be decided on what accuracy level the problem needs to have. Compared to other solvers, the Dormand-Prince solver gives medium accuracy (fifth-order accurate solutions). For now this problem it is assumed it will be accurate enough, because the equation of motion is solved quickly during the simulation. However, verification and validation of the model will conclude if another solver will have to be used nonetheless.

4.2. Verification

A better look will be given to the individual equations in the equation of motion (equation 8). A ship with a small and simple geometry (Table 6) is used as an example for this verification. The motions are viewed in one degree of freedom to simplify the problem. The result of the simulation is compared to an analytical calculation. The parameter I_{zz} is established by the relation $k_{zz}^2 M$, with $k_{zz} = 0.25L$ [28].

Table 6 Simple ship used for verification 3 DoF model

Length between perpendiculars, L_{PP}	12.00	[m]
Longitudinal position centre of gravity, LCG (from APP)	6.00	[m]
Ship displacement, M	49.20	[t]
Ship mass and added mass in surge, M_{xx} (1.05·M)	54.66	[t]
Moment of inertia around vertical axis, I_{zz}	442.80	[t·m^2]

Surge only

First, motion in surge is regarded only. For this case, the equation of motion can be brought back to just a simple mass-system

$$M_{xx}\ddot{u} = F_{x,ground}$$

The extra inertia term from equation 8 disappears, because there is no rotation. The only grounding force is in the opposite direction of the initial ship speed, resulting in

$$F_{x,ground} = F_{G,X}\cos\psi + F_{G,Y}\sin\psi = F_G$$

The grounding force is taken as F_G = - 0.1 MN. When this grounding force is put in the system the ship speed will drop constantly from the initial speed, taken as 2 m/s, to zero. The travelled distance will therefore increase but with each timestep more slowly until the ship has stopped. The simulation yields a speed of 0 m/s after 1.02 s. The ship has travelled 1.033 m. An analytical calculation

$$\dot{u} = \dot{u}_0 + \ddot{u}t = 0\ \text{m/s} \quad \rightarrow \quad t = \frac{-\dot{u}_0}{\ddot{u}} = \frac{-\dot{u}_0}{\frac{F_G}{M_{xx}}} = \frac{-2}{-1.83} = 1.09\ \text{s}$$

yields an end time of 1.09 s until the ship has come to a stop. An analytical calculation

$$u = \dot{u}_0 t + \frac{1}{2}\ddot{u}t^2 = \dot{u}_0 t + \frac{1}{2}\frac{F_G}{M_{xx}}t^2 = 2 \cdot 1.09 - \frac{1}{2} \cdot 1.83 \cdot 1.09^2 = 1.091\ \text{m}$$

yields a travelled distance of 1.091 m. (+5.3%, numerical error).

Sway only

Secondly, only the motion in sway is viewed in a one DoF system. The equation of motion can be brought back to the same term as the one DoF model in surge

$$M_{yy}\ddot{v} = F_{y,ground}$$
$$with\ F_{y,ground} = -F_{G,X}\sin\psi + F_{G,Y}\cos\psi = F_G$$

The extra inertia term disappears again for there is no rotation. The exact same result as in the motion in surge is obtained when the same values for the mass and grounding force is used.

Rotation only

Finally, the rotation is calculated using the simplified equation of motion

$$I_{zz}\ddot{\psi} = M_{z,ground}$$

The initial angular yaw velocity is taken as 0.05 rad/s. $M_{z,ground}$ = - 10 kNm is used as the grounding moment around the local vertical axis of the ship. The simulation yields that the angular yaw velocity decreases from 0.05 rad/s to 0 rad/s in 2.11 s and a yaw angle is created of 3.17 deg. Analytically, a quick calculation of the yaw angular velocity is

$$\dot{\psi} = \dot{\psi}_0 + \ddot{\psi}t = 0 \quad \rightarrow \quad t = \frac{-\psi_0}{\ddot{\psi}} = \frac{-\psi_0}{\frac{M_{z,ground}}{I_{zz}}} = \frac{-0.05}{-0.0226} = 2.21\ s$$

yields an end time of 2.21 s until the ship has stopped. The yaw angle is

$$\psi = \frac{1}{2}(\dot{\psi}_0 - \dot{\psi})t = \frac{1}{2}(0.05 - 0)2.21$$

is 3.17 deg (+0%).

4.3. Validation against large-scale experiment

4.3.1. Input

The implemented damage calculation model is validated against the TNO-ASIS large-scale ship grounding experiment. This is done to find out if the model is able to estimate the damage length from grounding force from experimental data. Appendix C gives more information on the support ship and test-section. The required input for the grounding model is:

- The constant horizontal grounding force, F_G [N];
- The initial velocity, v_0, [m s^{-1}];
- The rock eccentricity from CL, μ [m];
- The longitudinal position of first impact of the rock (FPOI) with the ship (from FPP) [m];
- General data of the ship (amongst others dimensions, inertias, etc.).

In the experiment it was tried to hit the rock on the centre line as exact as possible. A rock eccentricity, μ, of 0.30 m, however, was observed. The initial velocity was 7 kts.

The force measured in the longitudinal direction of the ship is shown in Figure 41. It shows that the grounding begins at t = 0.5 s and ends around t = 3.3 s, where the rock hits the buffer. The average of this longitudinal force (measured in the grounding time interval) is 0.40 MN. This value is plotted in Figure 41 as a horizontally dashed line. This force does not include the impact with the buffer. Figure 38 shows that no more energy gets absorbed (blue line) when the rock passes the test-section. The wire gauge, however, continues to measure displacement until the rock collides into the buffer. The mean force derived from the cumulative absorbed energy over the test-section is 0.60 MN (= 3.3 MJ/5.5 m). In Figure 24 shows that the length of the damage path is 6.7 m.

It is expected that the higher grounding force (0.60 MN) results in a shorter simulated damage length than resulting from the lower grounding force (0.40 MN).

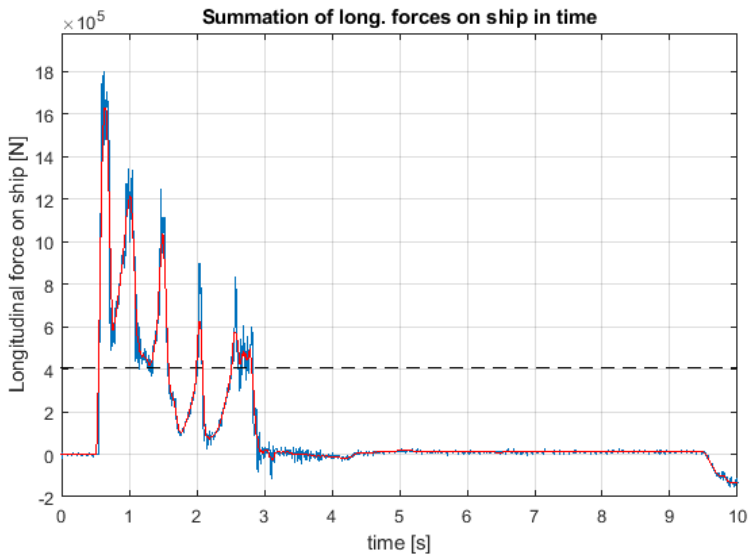

Figure 41 Sum of longitudinal forces on ship in time. Blue is raw data, red is smoothed data, black striped line is mean force during grounding (between t = 0.5 – 3.5 s)

4.3.2. Other parameters

The parameters that influence the result are: mass and added mass, x_{gy} (Equation 8 and 9), mean constant force during grounding and initial velocity. The rock eccentricity is small and therefore the moment around the vertical axis is as well. The sensitivity of the parameter x_{gy} is first investigated. This is done first because this value must be estimated for the experiment. In this validation the term x_{gy} does not have much influence on the result, because of the small angular yaw velocity (which is caused by the small rock eccentricity). This yields that x_{gy} does not have much influence on the stopping distance, ΔX_s, in longitudinal direction, the yaw angle at termination, ψ_{term}, and on the deviation from a straight line, δ. When x_{gy} increases, then ψ_{term} decreases and δ increases. When $x_{gy} = -x_{gy,0}$, then ψ_{term} and δ both increase. Increasing x_{gy} from 0 m to 6 m results in an increase in δ of 0.0004 m and a decrease of ψ_{term} of 0.018 deg. Because of its small influence and the difficulty to make a good estimation, this parameter will be set to zero.

4.3.3. Result

With this input data and the two grounding forces the simulation is performed. The simulation stops when the condition $V_{rel} = 0$ m/s is met. A summary of the results is shown in Table 7.

Table 7 Results of two simulations. Each with a different grounding force

Simulation	$F_G = 0.40$	$F_G = 0.60$	[MN]
Simulated stopping distance, ΔX_s	11.69	7.89	[m]
Yaw angle at termination, ψ_{term}	-0.21	-0.13	[deg]
Deviation from straight damage path, δ	0.06	0.04	[m]

The simulated stopping distance, ΔX_S, using the estimated force from the longitudinal load cells, $F_G = 0.40$ MN, is 11.69 m, the yaw angle at termination, ψ_{term}, is -0.21 deg and the maximum deviation from a straight damage path, δ, is 0.057 m. When using the 0.60 MN grounding force as input the damage path, ΔX_S, is 7.89 m, the yaw angle at termination, ψ_{term}, is -0.13 deg and the deviation from a straight damage path, δ, is 0.04 m.

From the results of δ is concluded that the offset of 0.30 m can be neglected because it does not have significant influence on the damage path. In this case, the grounding test can therefore be simplified to a one degree of freedom problem. The longitudinal displacement of these simulations are plotted in Figure 42. In this figure it is plotted together with the longitudinal displacement measured by the wire gauges and the longitudinal displacement derived from the surge acceleration signal. The figure shows that the wire gauges stop measuring distance when the rock collides into the buffer.

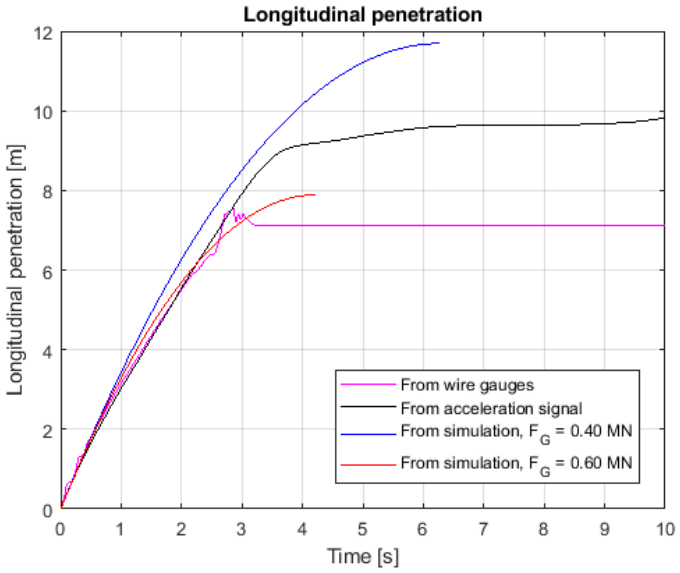

Figure 42 Longitudinal displacement of the rock

4.3.4. Comparison experimental data

The damage path which is simulated using $F_G = 0.4$ MN, derived from average force, is 5.0 m longer than the measured damage path. The damage path which is simulated using $F_G = 0.6$ MN, derived from absorbed energy, is 1.2 m longer than the measured damage path.

Increasing the grounding force will result in a shorter stopping distance. An average grounding force of 0.67 MN, results in the measured stopping distance of 6.7 m. The simulation grounding time is then 3.5 s, agreeing with the duration in the experiment.

The displacement of the 0.60 MN simulation resembles with this measured distance. This is to be expected, because this wire gauge data was used together with absorbed energy to calculate this average force. The smaller grounding force of 0.40 MN is derived from the same force, but averaged over the grounding time. Figure 42 shows that the displacement of this force's simulation shows the same trend in the first two seconds, but after that the simulated velocity is higher than in the other methods. Most importantly the figure shows that in around the first two seconds of the grounding still before impact with the buffer, the displacements of all methods closely resemble each other.

A factor that influences the simulation's results is the inertia. The total mass in surge for the experiment has been determined at 680.74 t (from the experiment's report [1]). A larger total mass results in a larger stopping distance, a decrease in a smaller stopping distance. A mass of around 410.00 t results in the damage length measured by the wire gauge in Figure 42 (7 m). Also, the duration of the grounding is using this value around 3.5 s, which coincides with the duration of the

grounding of the test. This difference in effective mass contributing in the stopping motion could be explained by the explanation given in section 3.2.3. Here is reasoned that the added mass is varying in time. Also the sloshing of the tank contents in the tanks can contribute to this time-varying inertia. The exact influence of the sloshing will not be dealt with, but the sensitivity of the inertias on the model will. This will be dealt with in chapter 5.

4.4. Validation against model from literature

The three degrees of freedom external dynamics grounding model is also validated against the example which Simonsen [2] uses in his three DoF grounding model. Also, a short case study using the validated model is carried out in order to investigate how certain parameters influence the ship motions due to grounding and the damage path.

Data of the ship Simonsen uses as an example in his model is given in Table 8. The parameter x_{gy} is determined from an estimation of the mass distribution over the length of the ship, which is shown in Figure 43. The structural mass distribution of the VLCC in this figure is determined from Figure 5.1 in [2]. The structural mass distribution is multiplied by a constant added mass coefficient. The x_{gy} from the LCG of the tanker is estimated 4 m in front of LCG (towards front ship). LCG is estimated with the rule: LCG = L/2 + 0.02L [31].

Table 8 Main particulars of VLCC

Length between perpendiculars, L_{PP}	322.70	[m]
Beam, B	58.20	[m]
Draught, T	21.00	[m]
Longitudinal position centre of gravity, LCG (from APP)	167.80	[m]
Block coefficient, C_B	0.81	[-]
Ship displacement, M	327,000.00	[t]

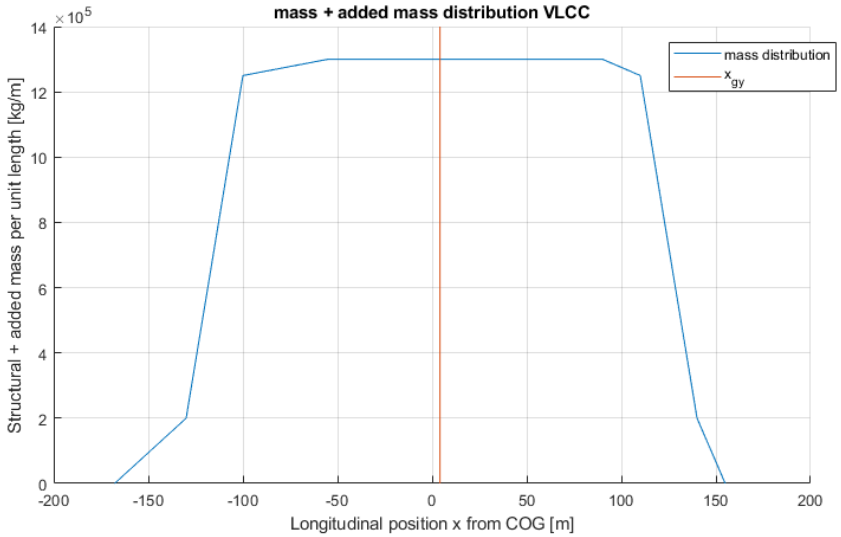

Figure 43 Structural mass and added mass in surge distribution along longitudinal axis of ship

The following input parameters will be investigated:

1. Magnitude of grounding force, F_G;
2. Initial velocity, v_0;
3. Rock eccentricity, μ;
4. First point of impact, x_r.

These parameters have a large influence on the damage path. It is investigated how large this influence is. The grounding force is determined by Equation 17 ([2], [16], [32]), where F_G is the initial kinetic energy of the ship (kinetic energy before grounding), $E_{kin,init}$, divided by a given stopping distance, d_s. This given stopping distance is one of the variables as input of the model described in 4.1.3 and Appendix F.

$$F_G = \frac{E_{kin,init}}{d_s} = \frac{\frac{1}{2} M_{xx} v_0^2}{d_s} \tag{17}$$

With:

$E_{kin,init}$ = kinetic energy of the ship before grounding [J];

d_S = given stopping distance [m];

M_{xx} = ship mass plus added mass in surge [kg];

V_0 = ship initial velocity before grounding [m s^{-1}].

In the case the ship hits the rock exactly on the centre line, the ship experiences no rotation. The simulation must then yield a simulated stopping distance, ΔX_s, equal to d_s.

The investigation into the four parameters is done on the basis of the following cases:

1. **Case 1:** The magnitude of the grounding force, F_G, is varied. This is done by letting the approximated stopping distance, d_s, vary from: 50 m, 75 m, 100 m, 125 m, 150 m, 175 m and 200 m. The initial velocity is constant (v_0 = 12 kts) and the maximum rock eccentricity, μ, is used; 26 m. At this eccentricity, the rock does not touch the hull until 12 m behind FPP. But because the maximum deviation is to be found, this will be neglected. We want to see the worst case scenario.
2. **Case 2:** The initial kinetic energy, $E_{kin,init}$, is varied by varying the initial velocity, v_0. The velocities will be varied from: 4, 8, 12 and 16 kts. This will be done at the grounding force where the maximum deflection was the biggest in the case of 1. The rock eccentricity is still maximum. Why the maximum deflection of case 1 ? Because this is the worst case scenario.
3. **Case 3:** The rock eccentricity will be varied: 0, 6.5, 13, 19.5 and 26 m. This will be done at an initial velocity of 12 kts and a force where the maximum deviation from a straight damage path is the biggest (in case 1).
4. **Case 4:** The first point of impact is varied: 0, 45, 90, 135 and 180 m (reference is from FPP, 180 m is behind midship). The initial velocity is 12 kts. The force is chosen so that the approximate stopping distance is 20 m. The offset is 13 m.

The results of the simulation are the simulated stopping distance, ΔX_s, the maximum deviation from the damage path from a straight line, δ_{max}, and the yaw angle of the ship when the grounding terminates, ψ_{term}. The validation is done on the

first two cases. For these two results of the literature model's example is known. The other two cases will be the case study, continuing the investigation into the external dynamics and the damage path.

4.4.1. Case 1

Damage path

In the first case the magnitude of the grounding force is varied. The rock eccentricity is taken at a maximum, 26 m (almost half the ship's beam). Figure 44 shows the simulated damage path along the bottom of the ship for seven different constant grounding forces. The damage path is represented as the deviation of the path from a straight line as a function of the distance from the point of first contact: 0 m means FPP. A positive deviation means that the rock contact path has moved towards CL. The graph's y-axis has a minimum of -3.1 m, this is where the damage path leaves the ship's side.

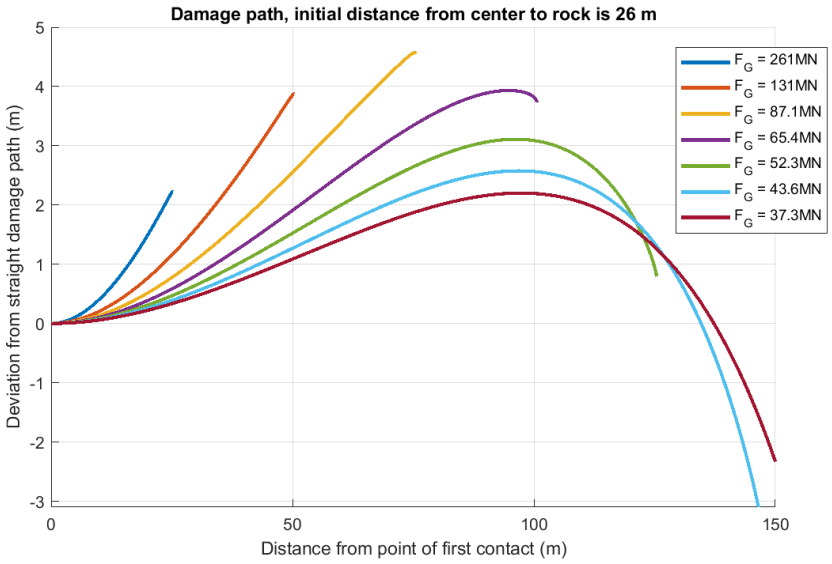

Figure 44 Damage path, varying grounding force

Figure 44 shows that when constant grounding force is decreased, the damage path length increases. Practically seen, the magnitude of the damage is smaller but the ship encounters not enough force to be stopped quickly resulting in a longer total damage length. The ship first locks onto the rock and, as it proceeds, rotates around it. This means that the damage path deviates from a straight damage path towards the ship's CL first (positive deviation). As the rock contact path is closer to LCG, the sway motion becomes larger and the ship turns away from the rock again. At that moment, the damage path starts to deviate back towards the original path and even further towards the ship's side for longer groundings.

The data from these seven simulations is given in Table 9. From left to right, the columns contain the grounding force F_G, the estimated stopping path, the simulated stopping path ΔX_S, the kinetic energy going into rotational motion, the maximum deviation from a straight damage path δ_{max} and the terminal yaw angle ψ_{term}. For the last two columns, results obtained by the literature model is also given in order to compare the results (from Table 7.1 from [2]). The term o.o.b. means that the damage path is out of bounds, the damage path has left the ship's side.

Good agreement is found between the model's and Simonsen's results. Highest deviation from Simonsen's data is -20.3% for the deviation from straight damage path (-1.00 m) and +24.6% for the final yaw angle (+3.86 deg).

Table 9 Data from simulation for varying grounding force

	F_G [MN]	$\frac{E_{kin,init}}{F_G}$ [m]	ΔX_S [m]	$\frac{E_{term}}{E_{kin,init}}$ [%]	δ_{max} [m]	δ_{max} Simonsen [m]	ψ_{term} [deg]	ψ_{term} Simonsen [deg]
1	261.0	25	25.2	-0.13%	2.23	2.15	-1.83	-1.60
2	131.0	50	50.	-0.07%	3.88	3.93	-4.09	-3.60
3	87.1	75	75.6	-0.10%	4.57	5.03	-7.11	-6.20
4	65.4	100	100.6	+0.01%	3.93	4.93	-10.87	-9.20
5	52.3	125	125.5	+0.25%	3.11	-	-15.23	-
6	43.6	150	150.0	+0.68%	o.o.b.	2.49	-19.56	-15.70
7	37.3	175	174.7	+1.19%	o.o.b.	-	-24.17	-

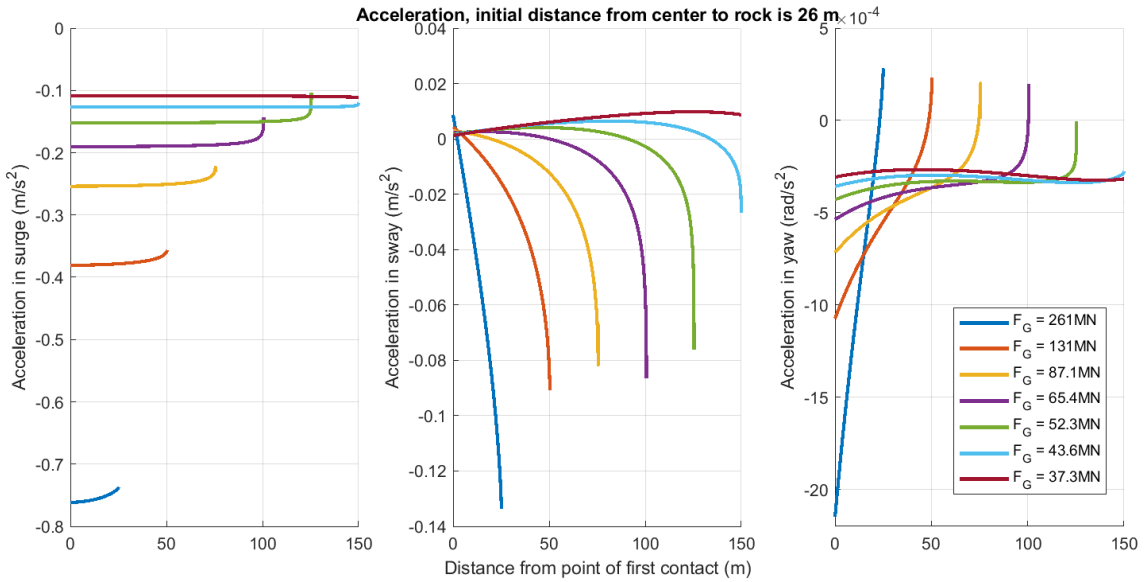

Figure 45 Accelerations in surge, sway and yaw for varying grounding force

Accelerations

The accelerations which belong to the damage paths from Figure 44 are plotted in Figure 45. Here the accelerations in surge, sway and yaw are plotted for each grounding force. The figure shows that for a larger grounding force the accelerations are higher overall, and for a smaller grounding force they are more constant and of lower magnitude (this is understandable by directly relating force to mass times acceleration).

4.4.2. Case 2

Damage path

In the second case, the initial grounding velocity, v_0, is varied. The velocities will be varied: 4, 8, 12 and 16 kts (2.06, 4.12, 6.17 and 8.23 m/s). This is done at the grounding force where the maximum deflection was the largest in Case 1. This is when the stopping distance is approximated to 75 m, giving a grounding force of 87.1 MN and a deviation of the straight damage path of around 4.6 m. For this study the rock eccentricity is kept at 26 m. The damage paths are plotted in Figure 46 and the data is summarized in Table 10.

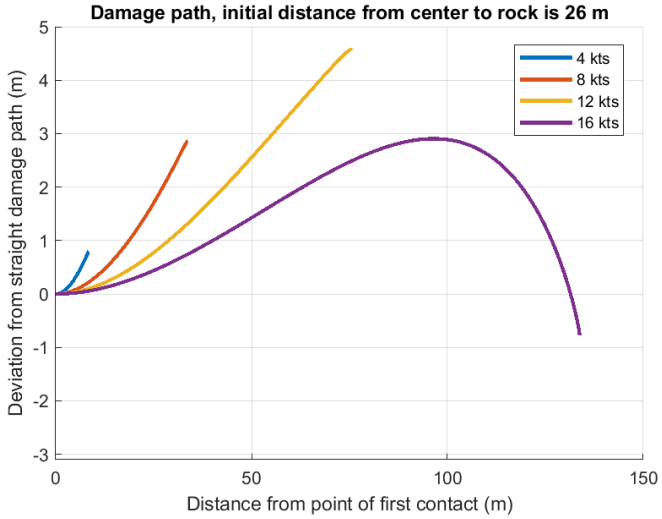

Figure 46 Damage path, varying initial velocity

The damage path at 12 kts is, of course, the same as the one for F_G = 87.1 MN in Figure 44 because they both use the exact same input. The shape of the damage paths in this case are similar to the damage path's from Case 1. This is as expected, because the only thing changed from Case 1 is actually the initial kinetic energy. This is in direct relation to the grounding force and the approximated stopping distance.

Again, the maximum deviation from a straight damage path and the yaw angle at the end of the simulation is given for both this simulation and Simonsen's (from table 7.2 from [2]). Again, good agreement is found in the results of the model and Simonsen's. Highest deviation from Simonsen's data is -9.3% for the deviation from straight damage path (-0.47 m) and +24.4% for the final yaw angle (+3.27 deg). Maximum deviation for the path of 16 kts comes across with the one in figure 7.5 of [2] (p. 107). But, the path in this simulation tends to have a negative deviation as well, while in Simonsen's simulation it does not.

Table 10 Data from simulation varying initial velocity

	v_0 [kts]	$\frac{E_{kin,init}}{F_G}$ [m]	ΔX_S [m]	$\frac{E_{term}}{E_{kin,init}}$ [%]	δ_{max} [m]	δ_{max} Simonsen [m]	ψ_{term} [deg]	ψ_{term} Simonsen [deg]
1	4	8.36	8.42	-0.04%	0.80	0.75	-0.55	-0.48
2	8	33.46	33.69	-0.03%	2.87	2.84	-2.48	-2.20
3	12	75.03	75.59	-0.09%	4.56	5.03	-7.10	-6.20
4	16	133.52	133.80	+0.43%	2.91	2.91	-16.67	-13.40

Accelerations

The acceleration signals for all four damage paths are plotted in Figure 47. The acceleration in surge declines as the ship rotates. Rotational and transverse accelerations increase as this happens.

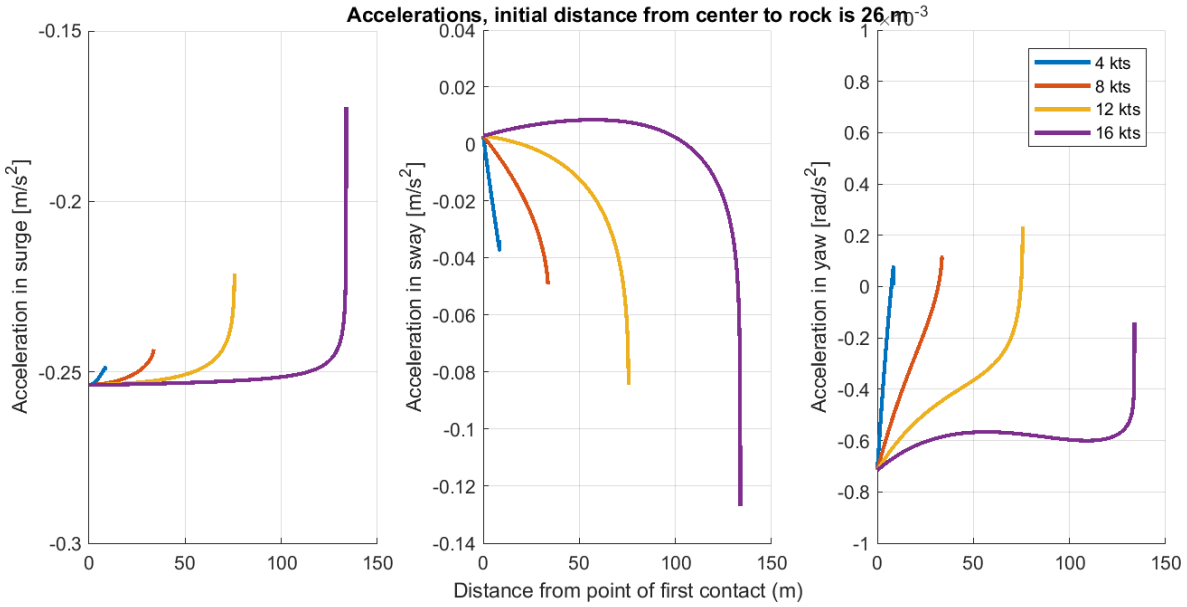

Figure 47 Accelerations in surge, sway and yaw for varying initial velocity

4.4.3. Conclusion

The agreement between the model's and Simonsen's results shows that the right parameters and values are used for the model. With values the investigation using the damage calculation model is continued in the case study.

4.5. Case study

4.5.1. Case 3

Damage path

The rock eccentricity, μ, is varied: 0, 6.5, 13, 19.5 and 26 m. This is done with an initial velocity of 12 kts and again with the same force as in Case 2, $F_G = 87.1$ MN. The main purpose of this case is to study how the damage path deviation relates to a certain moment created by the rock eccentricity.

The results of this simulation are plotted in Figure 48 and summarized in Table 11. The deviation of a straight damage path increases proportionally to the increase in rock eccentricity. For the first entry in the table it looks like part of the energy is going into a rotation (because of the non-zero percentage), but this is because of a numerical error in calculating the energy (Appendix F shows the energy calculator block).

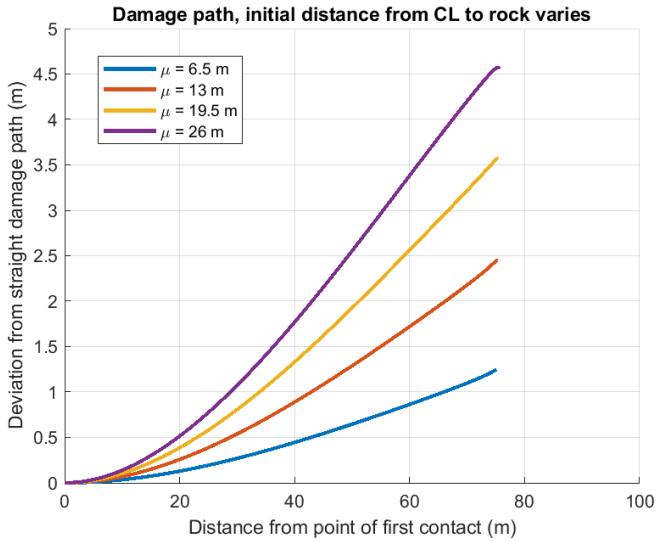

Figure 48 Damage path, varying rock eccentricity

Table 11 Data from simulation, varying rock eccentricity

	μ	ΔX_S [m]	$\frac{E_{term}}{E_{kin,init}}$ [%]	δ_{max} [m]	ψ_{term} [deg]
1	0.0	75.03	+0.01%	0.00	0.00
2	6.5	75.07	-0.01%	1.25	-1.82
3	13.0	75.19	-0.05%	2.45	-3.67
4	19.5	75.35	-0.07%	3.57	-5.39
5	26.0	75.59	-0.08%	4.57	-7.10

Accelerations

Figure 49 shows the accelerations of all simulations in surge, sway and yaw. A larger rock eccentricity gives more rotation (larger moment, thus larger accelerations), which these plots show.

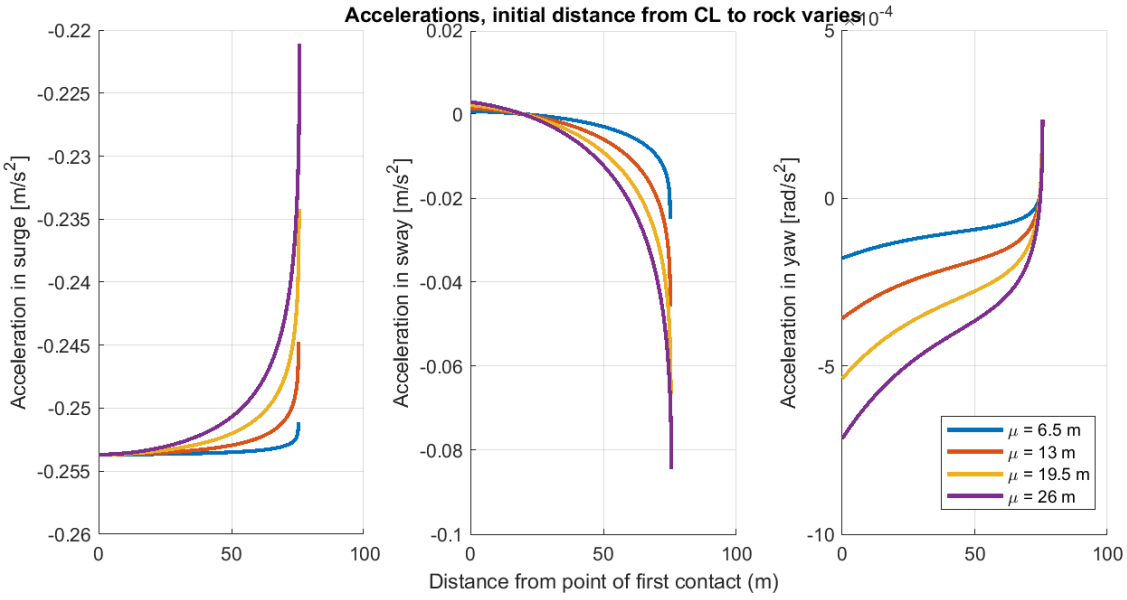

Figure 49 Accelerations in surge, sway and yaw for varying rock eccentricity

4.5.2. Case 4

Lastly, the first point of impact (FPOI) is varied. The initial velocity is 12 kts and the rock eccentricity is 13 m. This eccentricity is taken because this way the damage path has room to deviate the same distance both positively (towards CL) and negatively (towards the ship's side). The main purpose of this case is study the behavior of the damage path when the ship hits the rock more towards LCG. It will especially be looked at what the behavior is like when the first point of impact is behind LCG. Of course, the majority of grounding scenarios occur just front of midship because of the ship's forward speed [32].

This case is divided in three parts: Case 4 a, b and c. In the first the FPOI is varied for an approximated damage path, d_S, with a length of 20 m, the second with a damage path of 100 m and the last for 150 m. Different lengths are simulated as to show different effects of the longitudinal variation of the FPOI.

Damage path case 4a

In this case, the force is taken so that the approximate stopping distance is 20 m. The FPOI is varied from 0, 45, 90, 135 to 180 m. The results of this simulation is plotted in Figure 50 and summarized in Table 12.

Figure 50 shows that the damage path starting at 180 m behind FPP starts behind LCG. Because of this, it is the only damage path which deviates towards the ship's side immediately from the start of the grounding. The damage path which starts at 135 m behind FPP ends exactly at LCG. This contributes to the fact that the damage path deviates back towards CL again after some time. Also, this results in a small moment and therefore the yaw angle and maximum deviation from straight damage path is small (Table 12). The figure also shows that the maximum deviation decreases when the FPOI moves closer towards the LCG. This is explained by the fact that there is less distance(/time) to build up a yaw moment to give the ship a larger yaw angle and sway translation. Overall, the deviation from a straight damage path is small compared to its total length.

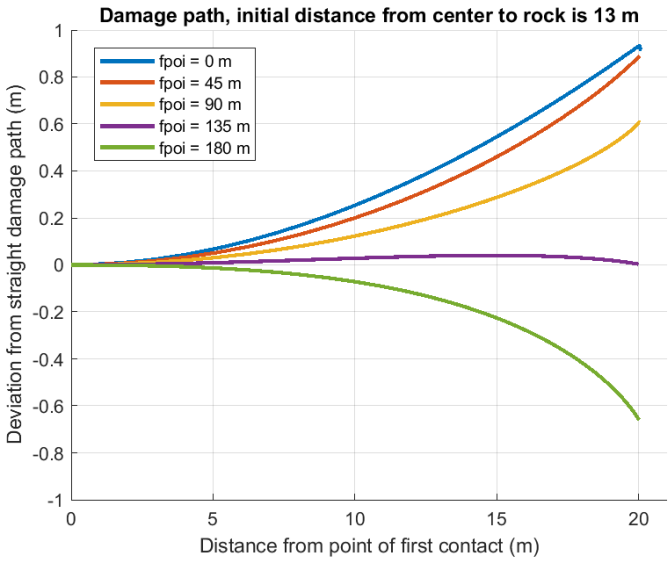

Figure 50 Damage path, varying first point of impact from FPP using a force resulting in a 20 m stopping distance

Table 12 Data from simulation Case 4a: varying first point of impact and X_s = 20 m.

	FPOI [m]	ΔX_S [m]	$\frac{E_{term}}{E_{kin,init}}$ [%]	δ_{max} [m]	ψ_{term} [deg]
1	0	20.08	-0.10%	0.93	-0.94
2	45	20.04	+0.01%	0.89	-1.01
3	90	20.04	-0.05%	0.61	-1.43
4	135	20.01	+0.04%	0.04	-1.60
5	180	20.01	+0.07%	-0.66	-1.47

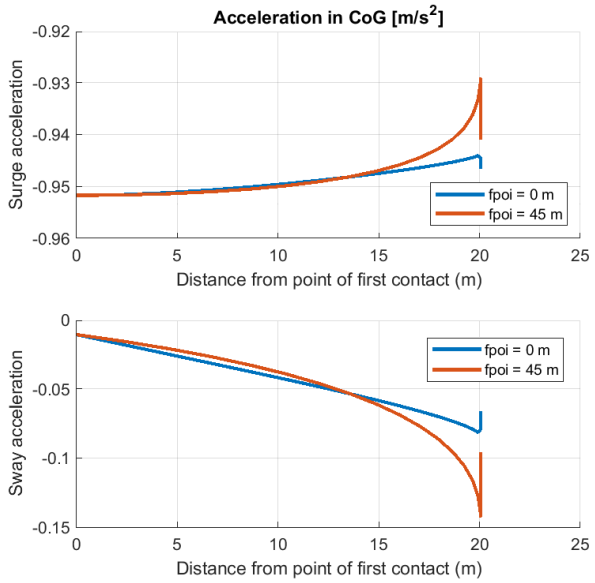

Figure 51 Accelerations of two closely resembling damage paths shapes.

Accelerations case 4a

Figure 50 shows that the shape of the damage paths with FPOI = 0 and 45 m almost coincide. The question is if their acceleration signals also resemble one another. Therefore their acceleration signals are plotted in Figure 51. The figure shows that at the end of the grounding for FPOI = 45 m, the surge deceleration decreases much faster than for the signal of FPOI = 0 m. The grounding force in sway direction is much larger for this case, explaining the more rapid decrease in surge deceleration and the increase in sway deceleration. The yaw angle at the end of the grounding for FPOI = 45 m is larger than for FPOI = 0 m (see Table 12). A larger force in sway direction of the ship indicates a larger yaw angle at the end.

Damage path case 4b

In this case, the grounding force is taken so that the approximate stopping distance is 100 m. The FPOI is varied from 0, 50, 100, 150 to 200 m. The results of this simulation are plotted in Figure 52 and summarized in Table 13. The plot is represented differently than in case 4a for a better visual representation of the damage paths along the ship bottom. The damage paths are plotted at the FPOI, but this time along the ship's longitudinal axis, at an eccentricity of 13 m. This eccentricity is set to zero. The minimum value of -16.1 m on the vertical axis of the plot indicates the ship's side. The ship's LCG is represented as a vertical black dashed line. The damage paths are plotted this way to get a better understanding of how the damage path varies along the ship bottom when the location of the rock impact in longitudinal direction is varied and how the position from the LCG has an effect on this.

The figure shows that when the FPOI is closer to LCG, it causes the damage path to start deviate towards the ship's CL less quickly. In Table 13 it is interesting to note that the damage path starting at FPOI = 50 m ends almost at LCG and the FPOI = 150 m starts here. In the first case this again means that the maximum deviation from a straight damage path is the smallest. At FPOI = 150 m, the damage path starts to leave the ship right away because of this.

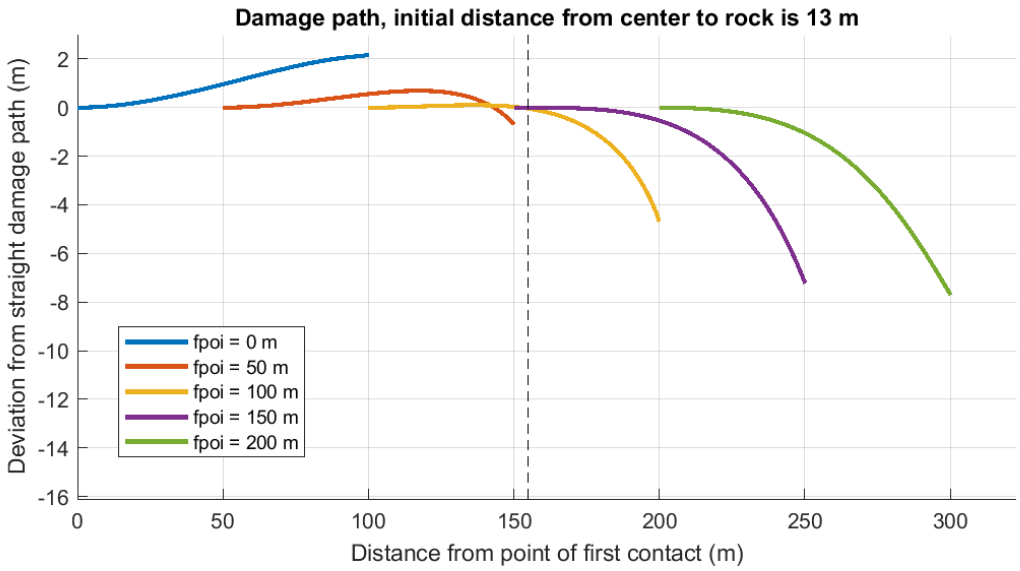

Figure 52 Damage path, varying first point of impact from FPP using a force resulting in a 100 m stopping distance. LCG in black

Table 13 Data from simulation Case 4b: varying first point of contact and X_s = 100 m

	FPOI [m]	ΔX_S [m]	$\frac{E_{term}}{E_{kin,init}}$ [%]	δ_{max} [m]	ψ_{term} [deg]
1	0	100.2	-0.02%	2.17	-5.60
2	50	100.0	0.07%	-0.70	-7.45
3	100	100.1	0.22%	-4.68	-7.79
4	150	100.2	0.30%	-7.21	-6.47
5	200	100.2	0.22%	-7.70	-4.65

Damage path case 4c

In this case, the force is taken so that the approximate stopping distance is 150 m. The FPOI is varied from 0, 50, 100 to 150 m. This case is done in order to test a longer damage path as well (and a smaller grounding force). The results of this simulation are plotted in Figure 53 and summarized in Table 14.

The figure shows that a path which started behind LCG tends to leave the ship from the start of the grounding. In Table 14 it is interesting to note that the damage path starting at FPOI = 0 m ends almost at LCG and the one starting at FPOI = 150 m starts here. In the first case this again means that the maximum deviation from a straight damage path is the smallest.

Accelerations case 4c

Figure 54 shows the acceleration signals belonging to these damage paths. The surge decelerations decrease in the case of an FPOI = 0 m. Here the deceleration of the ship is becoming smaller because of the created rotation (increase deceleration in sway and yaw). This happens rapidly near LCG, because the distance from rock to CoG in y-direction is now bigger than in x-direction. In the case of an FPOI closer to midship, the deceleration of the ship in surge is increasing in time. The yaw deceleration decreases in time, because the distance between rock and CoG decreases.

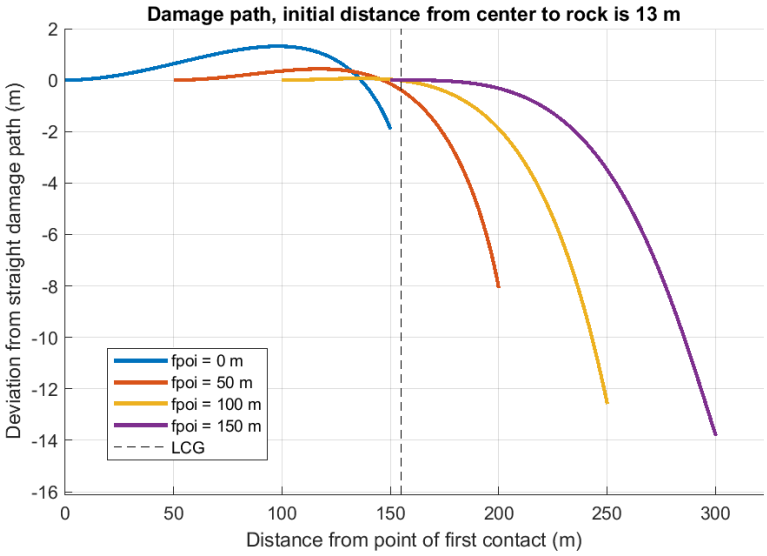

Figure 53 Damage path, varying first point of impact from FPP using a force resulting in a 150 m stopping distance

Table 14 Data from simulation Case 4c: varying first point of contact and X_s = 150 m

	FPOI [m]	ΔX_S [m]	$\frac{E_{term}}{E_{kin,init}}$ [%]	δ_{max} [m]	ψ_{term} [deg]
1	0	150.1	0.11%	-1.95	-10.53
2	50	150.0	0.37%	-8.09	-11.70
3	100	150.2	0.50%	-12.59	-10.24
4	150	150.2	0.44%	-13.83	-7.78

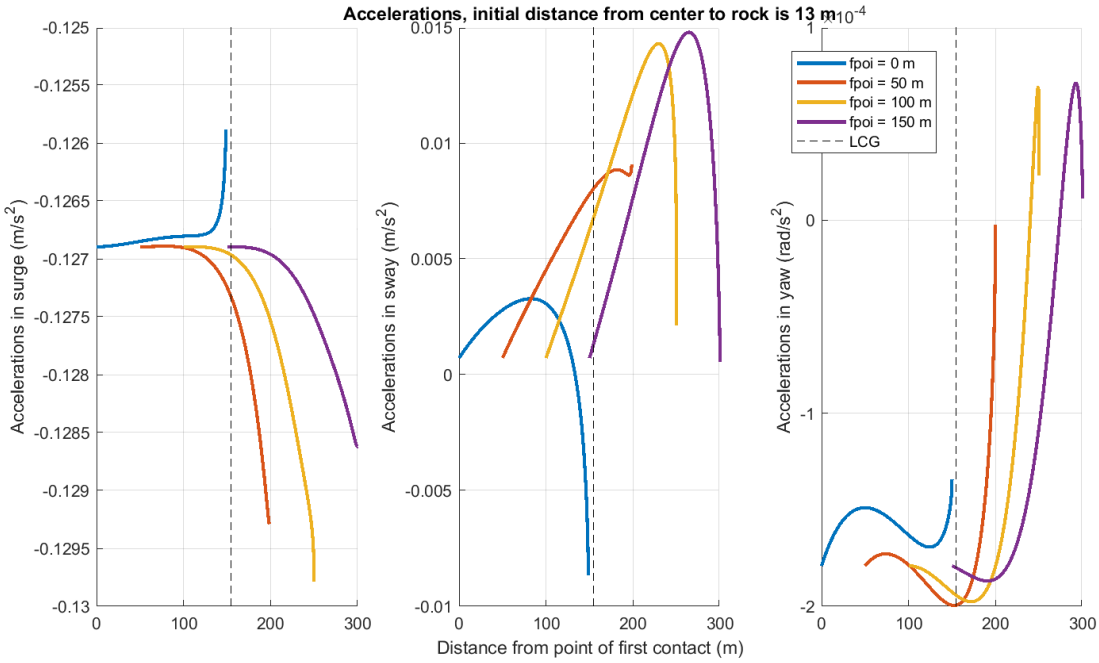

Figure 54 Accelerations in surge, sway and yaw. Plotted from FPOI over 150 m stopping path. The location of the LCG is plotted in black.

4.6. Conclusion

In this chapter the following sub-question was posed: *What is the damage path resulting from grounding force?* In order to answer this, a three degrees of freedom external dynamics grounding model was made. Using this model a small case study is performed. The damage calculation model will most importantly form the basis for the next step in the investigation.

The model is validated against the large-scale experiment first. The damage path which was simulated using F_G = 0.4 MN, derived from average force, is about 5.0 m longer than the measured damage path. The damage path which is simulated using F_G = 0.6 MN, derived from absorbed energy, is about 1.2 m longer than the measured damage path. Around the first two seconds of the grounding still before impact with the buffer, the displacements from all agree with one another. This means that the velocity determined through these methods, in the time before the buffer is hit, are comparable. A factor that influences the simulation's result is the inertia. It is observed that time-varying loads such as added mass and sloshing may be an important factor in the use of the external dynamics grounding model. Assuming constant inertias during the simulation is therefore not sufficient.

Secondly, the model is validated against the literature model of Simonsen. This validation is done in on the basis of two cases. Good agreement is found between the results of the model and those of the literature model. For the first case (varying grounding force) the highest deviations from Simonsen's results is -20.3% for the deviation from straight damage path (-1.00 m) and +24.6% for the final yaw angle (+3.86 deg). For the second case (varying grounding initial velocity) the highest deviations from Simonsen's results is -9.3% for the deviation from straight damage path (-0.47 m) and +24.4% for the final yaw angle (+3.27 deg). Differences in results between the model and the literature model become larger for longer damage paths (e.g. smaller grounding forces). These differences are, however, small compared to the total damage length. The omission of the damping term in Equation 8 explain these differences. When the rock contact forces are small, the influence of the damping forces become relatively more important.

Finally, a small case study is carried out investigating external dynamics and what the damage path looks like if the location of the first impact with the rock is varied. The cases' results show that the ship first locks on to the rock and the damage path first deviates towards the ship's CL. For longer damage paths, the damage path bends back to its original position and even tends to leave the ship's side. Also, as the FPOI is more towards LCG or behind it, the damage path tends to leave the ship right away.

4.6.1. Assumptions

Effect of the rock

The first assumptions that were made is that both the rock and the ship are rigid. Another assumption is that the rock is viewed as a point. From the literature study was learned that the relative rock size to the ship bottom structure has a strong influence on the deformation mode and magnitude [16]. Therefore it is assumed that the effects of the rock size and friction is included in the grounding force, and that varying this force means also varying rock size. Lastly it is assumed that the ship has a constant width between PP. These assumptions were made to better investigate the location of the damage path for all ship types, only based on the general dimensions.

External loads

External loads beside the grounding forces have not been taken into account in the equation of motion. The report on the grounding of the Costa Concordia [5] describes how the ship was influenced by the water's current and wind. The ship lost maneuverability and stranded once again due to its motion caused by these external loads. Also, the loads on the ship due

to waves are neglected, because the duration of the grounding is short and the investigation focusses on how the grounding forces influence the ship motions. Effects of and by the ship like resistance and propulsion are taken into account in the magnitude of the grounding force.

Only 3 DoF

The other motions: heave, pitch and roll, also have an effect on the damage path. For example, when the ship hits the rock at the bilge, the ship will tend to roll to the opposite side. Because of the assumption of only surge, sway and yaw motions, the damage paths from this model are the worst case scenarios. Because there is no heave, roll or pitch the contact between rock and ship bilge stays maximum.

4.6.2. Explanation different results

When F_G is decreasing (and the stopping distance is large), there is a larger difference between the grounding model's results and the literature model's results. An explanation for this is the omission of the damping term in the equation of motion used for this damage calculation model, while in the equation of motion used in [2] it is taken into account. The damping term for surge, sway and yaw are normally implemented using the damping coefficients in Equation 18 [26]. These exist because the ship generates waves when moving through the water. Also, in a viscous fluid, damping is also caused by the friction of the fluid past the ship. However, in order to determine the damping coefficients, details of the hull shape is required. For this model the goal was to use only the accelerations and the main dimensions of the ship. For the added mass coefficients this is also the case, but rules exist which are able to make a good estimation for these.

$$B_{jk} = \begin{bmatrix} B_{11} & 0 & 0 \\ 0 & B_{22} & B_{26} \\ 0 & B_{62} & B_{66} \end{bmatrix}, B_{26} = B_{62} \tag{18}$$

The lack of the damping term in the motion equation plays a large role in the differences between damage paths. When F_G is small, in Simonsen's equation the damping term makes good for this and stops the propagation of the damage in sway and yaw direction. But, if in the model large enough forces or short enough stopping distances are simulated, the influence is negligible. That is why, in the validation of the large-scale experiment, the omission of the damping term will not have much influence.

5

Calculation of rock contact path

The grounding of the Maersk Connector. When grounding is part of the job.

5.1. Methodology

A three degrees of freedom external dynamics grounding model was implemented and the validation results are in good agreement with the experimental data of the large-scale grounding experiment and the associated literature model [2], [12]. The sub-question is answered concerning how a prediction of the damage path can be done using information on the rock: rock grounding force on ship bottom and the location of impact with the rock is known. But, this is only a means to the goal. In a real grounding situation, there is no information on the rock. Now, the idea is to invert this method to answer the last sub-question:

Can the rock bottom contact path be derived using only accelerations?

An investigation is carried out on how a prediction can be done of the damage and the location of the damage without information on the first impact location with the rock on the ship and no knowledge about the forces acting on the ship. Instead, it is based on the acceleration measurements. In order to investigate this the implemented calculation model from the previous chapter will be inverted as is visualized in Figure 55. The reversed arrow conveys that output of the damage calculation model, visualized in Figure 39, will serve as the input for the inverse method. The inverse model's input are only be the accelerations measured on board (the output of the calculation model) and the initial velocity. The output of the model is the damage path. This output includes the shape of the damage path and the first point of impact (FPOI), the parameter that was used in the previous chapter to indicate the first location of the rock hitting the ship bottom. It is investigated if it is possible to track down the rock contact path from just the accelerations in surge, sway and yaw measured on board and the ship's initial velocity.

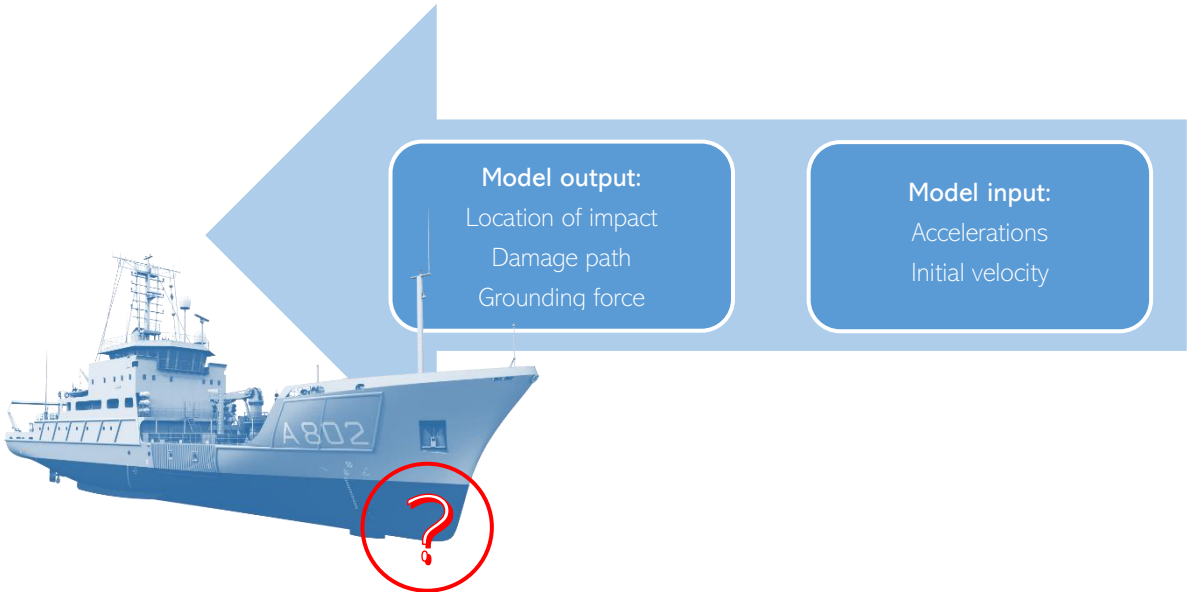

Figure 55 Visualization of research methodology

Summarizing this chapter's methodology: the damage calculation model from Chapter 4 is used as a basis. Simulations of grounding scenarios (different locations of first impact) are done and acceleration signals belonging to those scenarios are generated. It is then forgotten which signal belongs to which scenario. It is investigated if the scenarios can be found just by using the accelerations. The data is estimated (inertias) and the sensitivity of this estimation on the scenarios is investigated.

5.2. Grounding scenarios

The inverse method is implemented and subsequently tested by feeding it the output of the damage calculation model as input. The input are the acceleration signals with known FPOI from the damage calculation model from Chapter 4 and using the validated 322 m VLCC example. Three first point of impact locations in the local and global coordinate system are used to run the simulations and acquire the damage paths and respective acceleration signal in surge, sway and yaw. The constant grounding force which is used is derived from an approximated stopping distance following Equation 17. A stopping distance of 100 m and an initial velocity of 12 kts is used which results in a F_G = 65.4 MN. The simulated first point of impact locations are:

1. (x,μ) = (50,0) m
2. (x,μ) = (50,13) m
3. (x,μ) = (180,13) m

With x as the longitudinal distance from FPP [m] and μ as the transverse distance from CL to starboard [m]. The damage paths resulting from these impact locations are represented in Figure 56 (not to scale). The (50,13) m location has only a small deviation from a straight damage path of less than ±0.7 m. The (180,13) m FPOI damage path has a deviation from a straight damage path of about -7.5 m (negative sign as are used in Chapter 4 for the deviation from a straight damage, δ, path which deviates from CL). Of course, the path which starts on CL does not have any deviation.

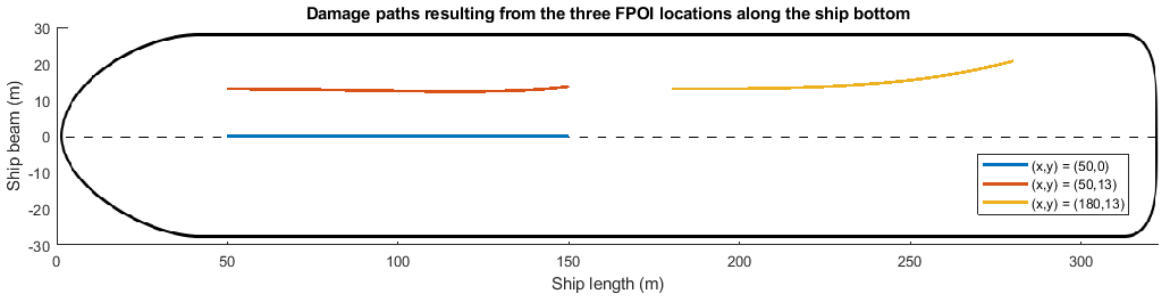

Figure 56 Damage paths presented along the ship bottom (top view)

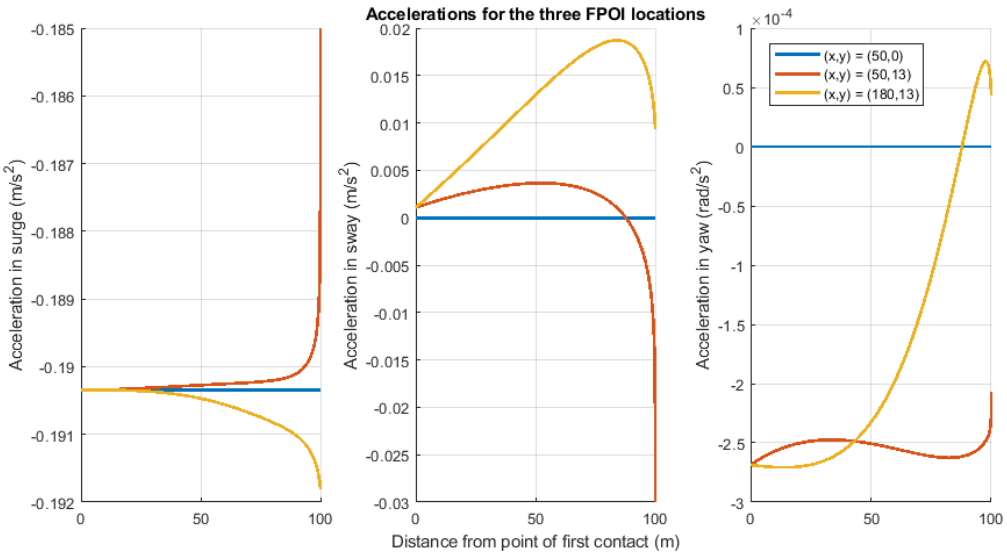

Figure 57 Accelerations in surge, sway and yaw for the three FPOI's

The acceleration signals for each damage path are plotted in Figure 57. In the situation of the first location, (x,μ) = (50,0) m, there are of course no sway and yaw accelerations measured. The acceleration in surge is constant, because of the application of a constant grounding force. The ship's speed decreases linearly to zero. For the second case, (x,μ) = (50,13), the ship first locks onto the rock and the damage path turns towards the CL. After 50 m the damage paths turns away towards the ship side again. There is more surge deceleration at the end of the grounding when the sway accelerations decreases again when the rock is near LCG. The last case, (x,μ) = (180,13), is an FPOI behind LCG, the damage path immediately starts to deviate from a straight damage path towards the bilge. Surge deceleration keeps decreasing while the surge acceleration keeps increasing up to the point where the yaw acceleration becomes positive. Typical levels of acceleration are 0.2 m/s^2 in surge and 0.020 m/s^2 in sway.

5.3. Inverse method

5.3.1. Implementing the inverse method

Now the approach of the inverse calculation method is discussed from input to output. The idea for the inverse method is to use only the measured accelerations as input, but the initial velocity must be used as additional information to make the method work. But generally the ship's velocity at any moment is known on board. Again, it is assumed that the initial velocity before grounding is purely in longitudinal direction of the ship. It is also assumed that the position of the CoG is known, at least the position of the LCG. After that the global accelerations, velocities and displacement are calculated from the local acceleration signals using the transformation equation between local and global coordinate system (Equation 16) and through (double) time integration, just as is done in the damage calculation model.

Now the equation of motion (Equation 8) are used to calculate the grounding force in the local coordinate system. These local forces, F_X and F_Y, are transformed to forces in the global coordinate system, $F_{G,X}$ and $F_{G,Y}$, using the relations in Equation 10. From this the constant grounding force, F_G, is found taking the two global grounding force vector's resultant. The method until this far is verified by checking if this constant force equals the grounding force given as input for the model (= 65.4 MN).

Section 4.1.2 states that the grounding force's resultant points in the opposite but parallel direction of the relative velocity between the ship and the rock. This relation is used to find out the global distance between the ship's CoG and the rock at every time step in both x- and y-direction: X_S and Y_S. From Equations 14 and 15 it is pointed out that the global grounding force in x- and y-direction have the same ratio as the relative velocity between ship and rock in x- and y-direction:

$$\frac{V_{rel,y}}{V_{rel,x}} = \frac{F_{G,Y}}{F_{G,X}} \tag{19}$$

Using Equation 11 and 12 and the yaw moment from Equation 10 and solving for the unknowns X_S and Y_S gives:

$$X_S = \frac{\dot{Y}_{glob} - \dot{X}_{glob}\frac{F_{G,Y}}{F_{G,X}} - M_z\dot{\psi}\frac{F_{G,Y}}{F_{G,X}^2}}{\dot{\psi}\left(1 + \frac{F_{G,Y}}{F_{G,X}}^2\right)} \tag{20}$$

$$Y_S = \frac{M_z + F_{G,Y}X_S}{F_{G,X}} \tag{21}$$

With:

X_{glob} = global longitudinal position of local coordinate system (CoG) [m];

$\dot{X}_{glob}$ = global longitudinal velocity of local coordinate system (CoG) [m s^{-1}];

Y_{glob} = global transverse position of local coordinate system (CoG) [m];

$\dot{Y}_{glob}$ = global transverse velocity of local coordinate system (CoG) [m s^{-1}];

$F_{G,X}$ = global longitudinal grounding force component [N];

$F_{G,Y}$ = global transverse grounding force component [N];

M_z = local grounding moment around CoG [N m];

$\dot{\psi}$ = yaw angular velocity [rad s^{-1}].

These parameters describe at any moment in time during the simulation the position of the ship's CoG to the global coordinate system's origin (rock). At the start of the simulation, these values present the first point of impact of the rock on the ship bottom:

$$x = (L - LCG) - X_S - X_{glob}, \text{ from FPP}$$
$$\mu = Y_S - Y_{glob}$$

With:

x = distance of first impact of the rock with the ship measured form FPP in X-direction [m];

L = length of ship [m];

LCG = longitudinal centre of gravity measured from APP [m];

μ = distance of first impact of the rock with the ship from CL in Y-direction [m];

Together with X_S and Y_S the damage path along the ship bottom can be calculated. An overview of the implemented inverse method is given in Appendix F.b and F.c.

5.3.2. Verification of the inverse method

Now the simulations for all three grounding scenarios are performed. The result of the simulations are the damage path and the acceleration signals for each scenario. At this moment it is forgotten which acceleration signal belongs to which scenario. Now, the inverse method is verified.

This is done by taking the acceleration signals and the initial velocity and taking them as input for the inverse method (as is shown in Appendix F.b). For now, the inverse method uses the same equation of motion and the same values for the parameters in it as is used for the damage calculation model. This way it is expected that, if the inverse method works, it should come up with the exact FPOI as was the input for the grounding scenario. The simulation is performed and the results are given in Table 15.

Table 15 Verification of the method

	FPOI locations		FPOI from method		check
	x	μ	x	μ	
1	50	0	NaN	NaN	✗
2	50	13	50	13	✓
3	180	13	180	13	✓

The table shows that for each grounding scenario the exact FPOI is found except for the situation where the ship hits the rock exactly on CL. In this last case the method has no way of calculating how large the forces in x- and y-direction are compared to each other, because the global force in y-direction and the global yaw moment are zero). Therefore the method cannot compute the arm of the yaw-moment and thus where along the ship's CL the grounding force acts. In order to get to know more about the FPOI in the case of impact of the rock on CL or when only surge accelerations are measured, more information should be available to make a correct estimate. For this the pitch signal of the ship can be used, but this requires a more complex calculation model. This will be looked at in more detail in section 5.6.

5.3.3. Conclusion

The inverse method is verified. Now it can be used to do a sensitivity study. In a real-life grounding scenario there is no exact determination possible of the inertias and added mass at every moment in time during the grounding. The question is if this has a large influence on the determination of the FPOI and damage path or not. Therefore, the sensitivity of the model is tested next.

5.4. Sensitivity study of the inverse method

In this paragraph the sensitivity of the inverse method is investigated. If some parameters are varied, how much will this influence the result of the method? How much deviates the prediction of the damage path from the original damage path? Next, some of these parameters are discussed.

5.4.1. Parameters

Velocity

The velocity of the ship is measured using GPS, which provides the fastest and most accurate method for mariners to navigate, measure speed, and determine location around the globe. The global average user range error (URE) of the system is ≤0.006 m/s over any three second interval, with a 95% probability. This error does not include any other factors which could influence the error outside the system's control, like satellite geometry, atmospheric conditions and receiver specifics.

The velocity of the ship is used in the method as input. Because of the reliable methods of determining the velocity of the ship at any time, any deviations from the actual velocity would be small. This makes this parameter very reliable. But nonetheless the influence of variation in this parameter on the inverse method's results is investigated.

Inertia and /loading condition

The method strongly relies on the estimation of the mass/moment of inertia and added mass of the ship during grounding. The added mass during grounding is assumed constant over time, but in reality this is not the case [22].

During the ship's lifetime its exact mass can become less clear. Also, its loading condition may be different than originally estimated when leaving port.

Sloshing, as indicated in section 3.4 and section 4.3.4, also influences the effective inertia in time used in the equation of motion. Determination of the effect of sloshing during grounding or even when in transit (filling level of tanks not accurately known) cannot be done exact.

5.4.2. Analysis and results

The sensitivity of the method on the predicted damage location is tested by varying one variable at the time for the case where the FPOI is (x,μ) = (50,13) m. The method's parameters are varied as follows:

Table 16 Variation of the parameters

Parameter	Variation	Remark
Initial forward velocity	6.17 ± 0.17 m/s	
Mass (+ added mass) in surge	1.05M ± 0.05M t	(taken so that upper bound is highest estimate of the added mass in surge = 10% of total ship mass M)
Mass (+added mass) in sway	1.40M ± 0.40M t	(taken so that the lower bound is exactly only the ship mass, no added mass)
Moment of inertia (+added mass) of yaw	3.17e+9 ± 1.05e+9 t·m^2	(lower bound is taken as the rule $I_{zz} = (0.25L)^2M$)

The results of this sensitivity study are summarized in Table 17. In the first column, the original values used for these parameters are given. In the next columns, each parameter is varied at a time. In the last column, for all the variables the lower or upper bound is taken in one simulation (varying all parameters at the same time). The results of the study are given in the lower half of the table. Here, the first and second row indicates the x-position of the FPOI from FPP and the error from the exact FPOI (x = 50 m). The third and last row indicate the y-position of the FPOI from the centre line (μ) and the error from the exact FPOI (μ = 13 m).

Table 17 FPOI prediction with variation in initial velocity and inertias. Original FPOI is (x,μ) = (50,13) m.

	VARIABLES				
M_{xx} (kg)	1.00M/1.10M	1.05M	1.05M	1.05M	1.00M/1.10M
M_{yy} (kg)	1.40M	1.00M/1.80M	1.40M	1.40M	1.00M/1.8M
I_{zz} (x10^9) (t m^2)	3.17	3.17	2.12/4.24	3.17	2.12/4.24
v_0 (m/s^2)	6.17	6.17	6.17	6.00/6.34	6.00/6.34
	RESULTS				
x (m)	50.16/49.87	49.88/47.99	49.23/50.80	63.40/36.39	61.17/36.23
Error x	+0.32%/-0.26%	-0.24%/-4.02%	-1.54%/+1.60%	+26.80%/-27.22%	+22.34%/-27.54%
μ (m)	13.53/12.50	12.17/13.72	10.35/15.75	10.52/15.66	8.353/19.51
Error μ	+4.08%/-3.85%	-6.38%/+5.54%	-20.38%/+21.15%	-19.08%/-20.46%	-35.75%/+50.08%

From Table 17 is observed that when the error is positive the FPOI shifts away from FPP to the back of the ship in longitudinal direction or away from CL in transverse direction. When the error is negative the FPOI shifts towards FPP in longitudinal direction or towards CL in transverse direction. The table also shows that when the mass in surge is decreased the FPOI slightly shifts away from FPP and away from the CL. This is because the global grounding force component in x-direction, $F_{G,X}$, is now smaller and with that $F_{G,Y}$ becomes larger. This respectively results in an FPOI further away from FPP and further away from CL. When or the mass in surge or the moment of inertia is decreased, the FPOI shifts towards the front and towards CL. This is explained by as each variable is decreased, the resulting sway or yaw angle increases. More sway means more transverse penetration by the rock, getting closer to the CL. An increasing yaw angle means more transverse displacement of the ship, resulting in the same effect. When the initial velocity is smaller the FPOI shifts towards

APP and towards CL, so more towards CoG. This is because now the damage path is estimated shorter and therefore the displacements in x- and y-direction are also estimated smaller. Lastly, when every parameter is decreased at the same time (in the fifth and last column) the FPOI shifts towards APP and CL (towards CoG). Varying the initial velocity or the moment of inertia (third and fourth column) has the largest influence on the estimation of the FPOI. In the fifth column, the largest error in x-direction (-27.5%,) is due to the higher moment of inertia and the largest error in y-direction (+50.1%) is due to a combination of a lower moment of inertia and lower initial velocity. When all variables are increased the opposite happens from when the variables are decreased. This is true for every parameter discussed, but not for the mass in sway, M_{yy}. When this parameter is increased the FPOI still moves towards FPP instead of the opposite. This is because the effect of the mass in surge is still the largest factor in the longitudinal location of the FPOI.

5.4.3. Analysis of FPOI

Some more simulations are performed, but without varying the initial velocity. Although this parameter has a large influence on the FPOI estimation, the velocity is accurately measurable on board using GPS. The simulations are carried out in the same fashion, but now the inertias are varied a fixed amount. The mass in surge and sway and the moment of inertia are varied ±20% and ±40% of its original value. The results are summarized in Table 18 and Table 19. Here, each column represents a simulation with one parameter varied a certain amount from their original value. For a better visual representation, the same results are plotted in Figure 58. This figure gives a better picture on how the location of the FPOI changes w.r.t. the actual FPOI. The actual/original FPOI is depicted with a black cross. The two dots per line are the ±20% and ±40% intervals of M_{xx}, M_{yy} and I_{zz}. Lastly, all masses are varied ±20% at the same time and ±40% at the same time. This is presented in the last column of each table.

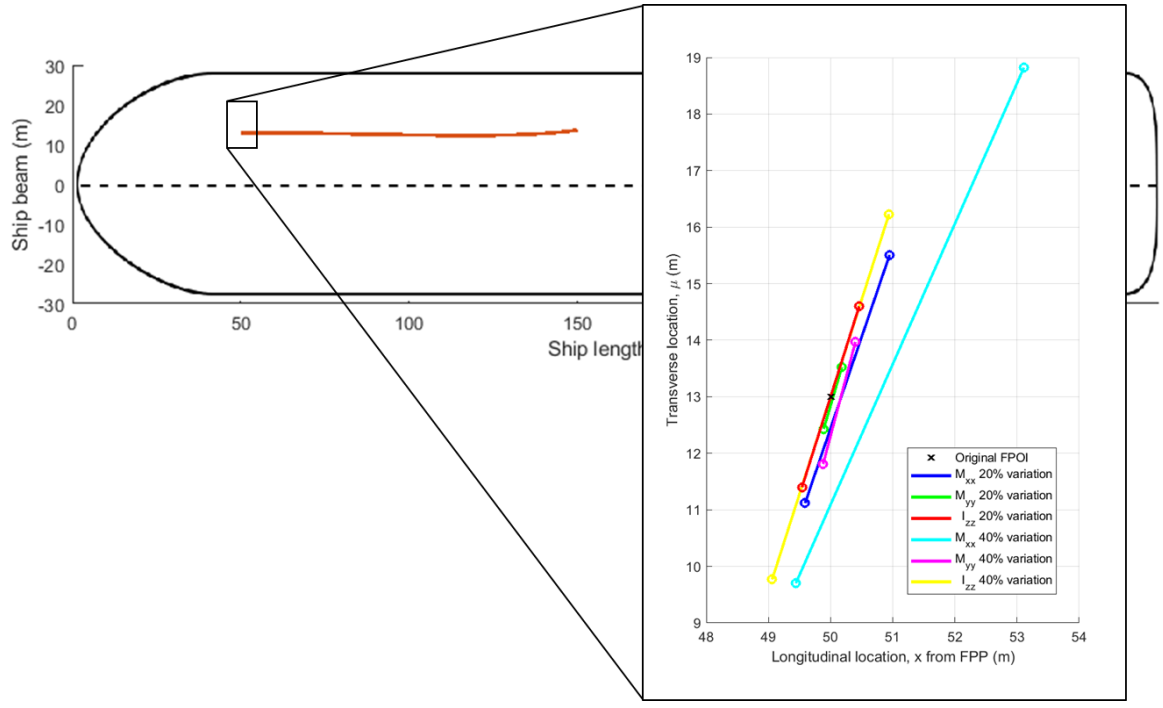

Figure 58 FPOI resulting from inertia variation

Table 18 FPOI prediction with ± 20% inertia variation

VARIABLES				
M_{xx} (kg)	-20%/+20%	$M_{xx,0}$	$M_{xx,0}$	-20%/+20%
M_{yy} (kg)	$M_{yy,0}$	-20%/+20%	$M_{yy,0}$	-20%/+20%
I_{zz} (kg·m^2)	$I_{zz,0}$	$I_{zz,0}$	-20%/+20%	-20%/+20%
RESULTS				
x (m)	50.95/49.59	49.89/50.18	49.54/50.46	50.00/50.00
Error x	+1.9%/-0.8%	-0.2%/+0.4%	-0.9%/+0.9%	0.0%/0.0%
μ (m)	15.51/11.12	12.43/13.52	11.4/14.6	13.01/12.99
Error μ	+19.3%/-14.5%	-4.4%/+4.0%	-12.3%/+12.3%	+0.1%/-0.1%

Table 19 FPOI prediction with ± 40% inertia variation

VARIABLES				
M_{xx} (kg)	-40%/+40%	$M_{xx,0}$	$M_{xx,0}$	-40%/+40%
M_{yy} (kg)	$M_{yy,0}$	-40%/+40%	$M_{yy,0}$	-40%/+40%
I_{zz} (kg·m^2)	$I_{zz,0}$	$I_{zz,0}$	-40%/+40%	-40%/+40%
RESULTS				
x (m)	53.11/49.44	49.88/50.40	49.06/50.94	50.00/50.00
Error x	+6.2%/-1.1%	-0.2%/+0.8%	-1.9%/+1.9%	0.0%/0.0%
μ (m)	18.82/9.70	11.81/13.97	9.77/16.23	12.99/13.01
Error μ	+44.8%/-25.4%	-9.2%/+7.5%	-24.9%/+24.9%	-0.1%/+0.1%

From the Table 18, Table 19 and Figure 58 it is seen that the largest influence on the FPOI in x-direction is when the parameter M_{xx} is varied. The largest influence is on the transverse location of the FPOI. Varying one parameter will cause the transverse location of the FPOI to deviate more from the actual value than the longitudinal location of the FPOI deviates from its original. In the tables this is shown by the larger deviation in percentage, but Figure 58 shows this even more clearly. The deviation in meters for the transverse location of the FPOI is larger than the deviation in meters for the longitudinal direction. The maximum positive and negative deviation from the original FPOI (μ = 13 m) in meters in transverse direction is +5.82 m and -3.30 m (varying M_{xx} ±40%). The maximum positive and negative deviation from the original FPOI (x = 50 m) in meters in longitudinal direction is +3.11 m and -0.94 m (varying respectively M_{xx} -40% and I_{zz} -40%). Of course, the largest deviations are found when looking at a higher variation percentage (±40% instead of ±20%). What is interesting to note, based on the results from the last column, is that if all parameters are varied the same amount (+xx% or -xx%) at the same time the FPOI does not deviate (or barely, ±0.1%, because of a numerical error).

5.4.4. Analysis of shape of damage path

But what influence has varying the inertias on the shape of the damage path? The inverse calculation method uses this deviating first impact location and the measured accelerations to calculate the damage path along the ship bottom. The resulting damage paths from each parameters variations are plotted along the ship bottom in Figure 59. The two lines of each colour indicate the -xx% and +xx% variation of each parameter. The original damage path starting at FPOI (x,μ) = (50,13) m is drawn in orange on the ship and in black in the plot as well.

The largest difference from the original damage path is when M_{xx} is varied ±40%. Because the most prominent motion is in surge (initial velocity), this variable yields the largest influence on the damage path. The variable which yields the second

largest influence is I_{zz}. The figure shows that as the variation of one variable becomes larger (20% to 40%), the damage path deviates more from the original. This deviation is most prominently in transverse direction.

The largest influence on the location of the damage path is, however, because of the estimation of the FPOI. The influence of the variation of each parameter on the actual shape of the damage path is discussed next.

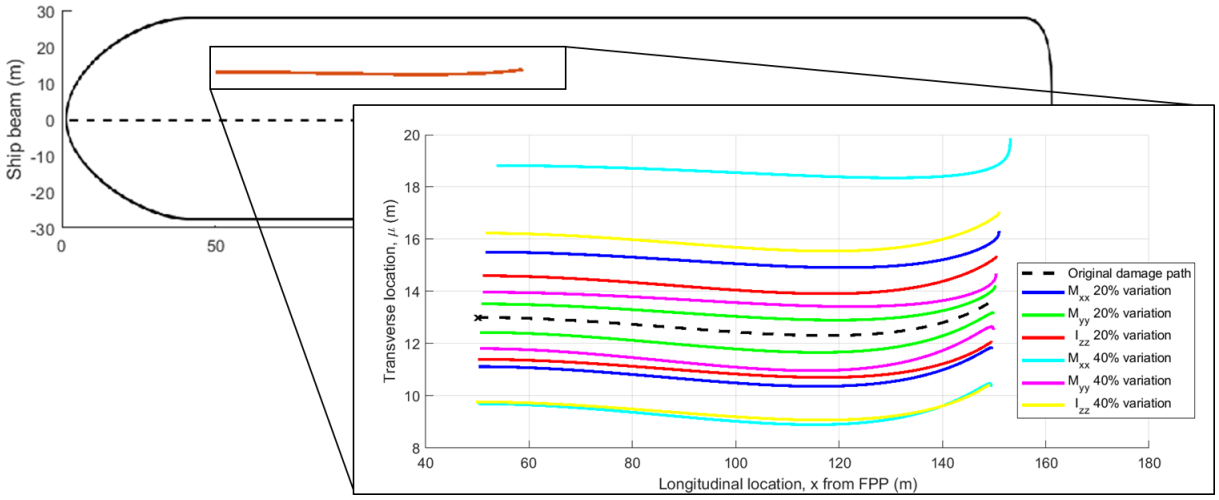

Figure 59 Damage paths resulting from mass/inertia variation

As said before, the parameters have a small influence on the actual shape of the damage path. This is because the shape of the damage path is mostly derived from the original acceleration data with the use of the *global integration block* (Appendix F.c, point 4) and not using the equation of motion, which makes use of the parameters. But, there is a small difference in between these individual damage paths because the method does still make use of the distance between the rock and the CoG at any moment during the simulation. The maximum deviation from a straight damage path, δ, for each simulation is given in Table 20. Here a negative sign of δ indicates maximum deviation towards the ship's side and a positive sign indicating maximum deviation towards CL. The original maximum deviation from straight damage path for the original damage FPOI is +0.70 m and -0.69 m. The table also gives the error in % of how the simulated δ deviates from these original values.

The table shows that δ ranges from –0.84 m (M_{yy} -40%) to +1.05 m (M_{xx} -40%). This is only -0.15 m and +0.35 m deviation from the original values. From this it is concluded that the effect of the variables on the shape of the damage path is very small.

Table 20 Maximum deviation from straight damage path for each rock contact path for each parameter's variations. Error indicates deviation in % from original maximum deviation from straight damage path.

Original maximum deviation from straight damage path, δ_0: +0.70 m and -0.69 m

	M_{xx}		M_{yy}		I_{zz}	
Variation	-20%/+20%	-40%/+40%	-20%/+20%	-40%/+40%	-20%/+20%	-40%/+40%
δ (m)	+0.80/-0.76	+1.05/-0.80	-0.77/+0.71	-0.84/+0.72	-0.69/+0.76	-0.70/+0.82
Error δ	+13.9%/+9.4%	+48.5%/+16.2%	+10.9%/+0.8%	+22.1%/+2.3%	+0.3%/+8.1%	+0.7%/+16.4%

5.5. Conclusion sensitivity study

Table 17 shows that the moment of inertia and the initial forward velocity both have a large influence on the damage path in transverse direction. The moment of inertia also has a large influence on the damage path in longitudinal direction.

Table 18, Table 19 and Figure 58 show that varying the value of the inertias has a substantial influence on the damage path. However, if the ratio between the inertias remains fixed, the damage path is not affected. If the inertia ratios remain the same to one another, so will the accelerations/forces (as is derived from the equation of motion). The method therefore strongly relies on the ratio between the measured/simulated accelerations and on the ratio between the forces.

From the sensitivity study is learned that the larger the variation of one of the inertias from their initial value, the larger the deviation from the original damage path, δ. The variation of the inertias have the largest influence on the damage path in transverse direction. The FPOI in this direction varies up to +5.8 m and -3.3 m, while the FPOI in longitudinal direction only varies up to +3.1 m and -1.0 m. The longitudinal deviation of the FPOI is very small considering a damage length of 100 m. But although this deviation is small, this could mean that the ship bottom of one compartment is actually ruptured while the prediction does not say so. This means that a small prediction error in longitudinal direction could have a large effect on the overall damage stability of the ship. The transverse deviation of the FPOI causes the predicted damage path to have a larger deviation in transverse direction. But generally tanks or compartments are from CL to SB or PS side, meaning while a bigger prediction error in transverse direction exists, this means such an error has a smaller effect on the overall damage stability of the ship than for an error in the prediction of the longitudinal location of the damage path. Summarizing: while the error of the determination of the damage path location in longitudinal direction is smaller, the risk of such an error is larger than an error in transverse direction.

From the results of Table 20 is concluded that the effect of the variation of inertia on the shape of the damage path is small.

What could help the determination of the transverse location of the damage path is the use of more data like the roll signal. This, however, would call out for a more complex external dynamics grounding model (6 DoF for example).

5.6. Estimation of damage path location in the case of impact on CL

From the simulation performed in paragraph 5.3.2 is seen that determination of the damage path when there are only surge accelerations to work with is not possible using this method. When only surge accelerations are measured, how can the damage path location still be estimated?

The estimation of the FPOI exactly on CL is investigated by looking at the ship of the large-scale grounding experiment, the Nedlloyd57, again. From the pitch signal is observed that at the moment of grounding the ship will also start to pitch. When the ship is hit in front of the LCG, the ship will start to pitch positively. When the ship is hit behind LCG, the ship will pitch negatively. This still gives a bad estimate of the impact location. But using the length of the damage path (from the measured acceleration signal) and the pitch signal it can also be found out if part of the damage path is behind LCG (from changes in pitch angle).

Figure 22 shows that the pitch increases positively when the grounding starts. Without the previous knowledge on the grounding experiment (ignoring that the test-section is not part of the ship), one can determine that the FPOI was located at least between the front of the ship and 7.0 m (length of registered damage path) in front of LCG. More information which,

as is pointed out from the analysis in Chapter 3, can be extracted from the large-scale experiment acceleration signal is the location and the number of floors. The grounding starts and a large deceleration is measured instantly which indicates that the grounding does not start gradually but the rock encounters a massive resistance immediately. This instant decelerations instead of a gradual increasing resistance therefore indicates that a structure of large resistance, like a transverse floor/bulkhead, is met, as would be expected at the front of the ship. In the case of a gradual deceleration signal, one could imagine a trimmed ship scraping the rock while the resistance force keeps increasing because vertical penetration gradually does so as well. Assuming a transverse member is hit at the beginning of the grounding, the FPOI can then be located at every transverse frame along CL between FPP and 7.0 m in front of LCG, which has a span of 36.34 m. The transverse stiffener spacing is 1.25 m, therefore there are twenty-nine points where the FPOI can be located based on this information while assuming that there are no other types of transverse members in the ship (ship will contain larger transverse members than frames like bulkheads).

5.6.1. Probability damage location

The probability of the damage location in a grounding scenario is researched by Zhu, James & Zhang [32]. Grounding damage statistics for Ro-Ro and merchant navy ship types for incidents in the period 1990–1999 are presented in the damage database of Lloyd's Register. For each incident the authors pinpoint the largest single damage extent. They observed single damages are unlikely to be greater than L/5. The total damage extent is longer than that because of multiple damaged surfaces on the ship bottom. It is found that for the larger damages the damage paths are located around the midship and midship to fore region. This is because most ships operate with a bow up trim. For establishing the location of the damage, instead of the first point the midpoint of the largest extent of the damage is indicated in Figure 60, because of the various damage lengths. The figure also shows the length of the damage relative to the ship's length used in the database.

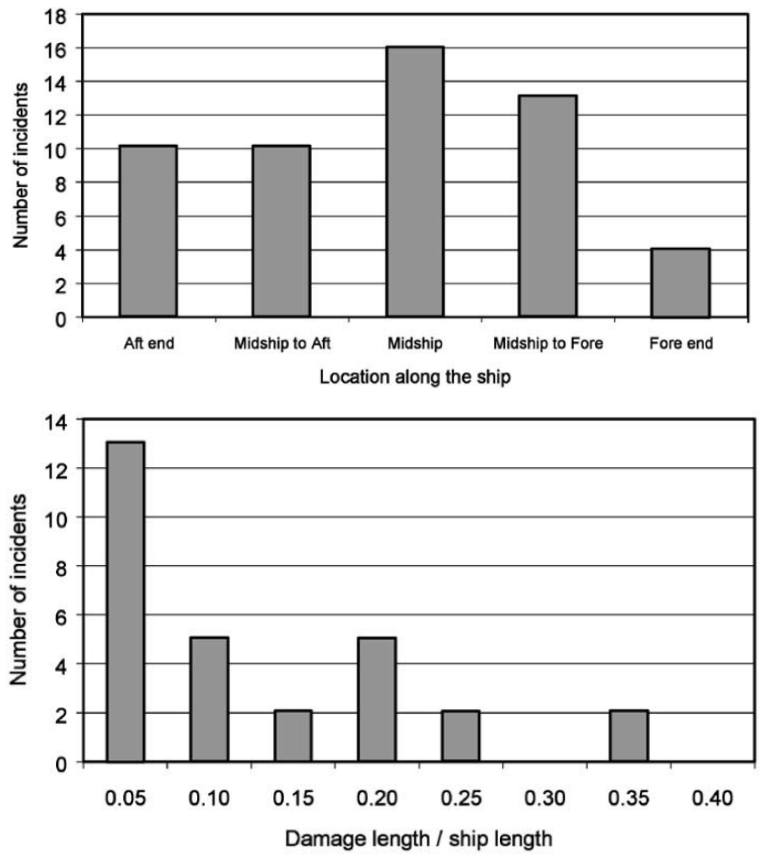

Figure 60 Damage locations and length ratios from grounding incidents (Figure 2 and 4 from [32])

The damage length/ship length ratio of the Nedlloyd57 is in the 0.10 category in Figure 60. From the data in this figure the probabilities of the location of the impact location on the Nedlloyd57 are calculated. The distances are measured form APP (0 m) to FPP (68.3 m). The frames are spaced 1.25 m from each other.

- 48.5% probability the FPOI is located at a frame in the range of 32.05 and 43.30 m (midship);
- 39.4% probability the FPOI is located at a frame in the range of 44.55 and 57.05 m (midship to fore);
- 12.1% probability the FPOI is located at a frame in the range of 58.30 m and FPP (fore end).

Using this method the most probable FPOI is located in the range from 32.05 to 43.30 m (midship region), although the actual FPOI is at FPP (which has only a 12.1% probability here).

5.6.2. Assumptions

However, based on the data from Figure 60 this estimate of the FPOI is not entirely reliable. The study gives a distorted view on the location of the damage path. In the study the extent of the damage has been investigated and the location of the damage is established by taking the midpoint of the single damage path along the observed ship's bottom. For a better illustration of the problem of using the midpoint of the damage and no further data on the length of the damage, a single hull VLCC used as an example in [32] is depicted in Figure 61. The figure shows that for the damage path on this VLCC the midpoint is in the region midship to fore, but actually the FPOI is located all the way on the fore end. Only the midpoint, however, is documented in the study and not the exact damage length. Although the Nedloyd57's damage length to ship length ratio is also in the database, there are also ships with much longer damage paths w.r.t. their length in this database which can have a distorting effect on the probability data. Without further data on the exact length of the damage per documented midpoint, Figure 60 may only be used as an estimate of the overall damage location (location is most likely towards midship to fore in the case of an all positive pitch signal), but cannot be used as an exact estimate of the FPOI.

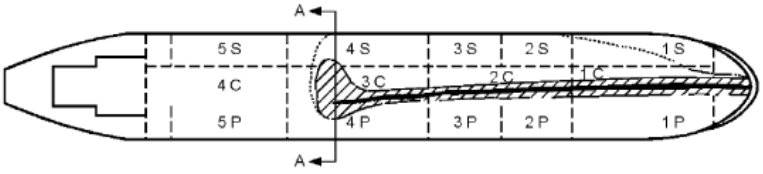

Figure 61 Grounding damage of a single hull VLCC (figure 6 from [32])

Of course the grounding scenario of the large-scale experiment was a forced scenario where the rock stood high above the waterplane in order to make a good visual evaluation of the grounding and let the ship hit it in the front on purpose. So it is not a good representation of a realistic grounding in the frame of this statistical study. Also, it is unsure how Figure 60 would look like if also grounding data of other ship types is taken. Grounding data on ship types which sail with less trim would influence the data in such a way that the probability would shift to the fore end. This also applies to ship types which mainly sail in forward direction most of the time (larger cargo ships and tankers).

5.7. Conclusion

From the investigation using the three DoF external dynamics grounding model is learned what the behaviour of the ship motions are in certain grounding scenarios. These are expressed in accelerations induced by the forces of the rock on the ship. From these accelerations the damage paths incurred by the rock on the ship can be found. But in a real grounding event the only thing known just after the event is the initial velocity just before grounding and the accelerations measured during the grounding on board. That is why the third sub-question was posed: *Can the rock bottom contact path be derived using only accelerations?*

In this chapter, an inverse calculation model is presented for finding the location of the damage using only this information. The presented method can reproduce the damage paths and the first point of impact of the rock on the ship bottom satisfactorily. But what remained was the question how reliable this method really is. The method relies most prominently on the correct estimate of the ship's inertias. From the sensitivity study it is concluded that a variation of the inertia or initial velocity does make that the estimate of the FPOI deviates from the actual position of this point. It is seen that the effect of this variation has more effect in transverse direction than in longitudinal direction, but it is reasoned that a deviation of the FPOI in longitudinal direction has more implications on the ship's damage stability than a deviation in transverse direction although this deviation is larger. However, what could help the determination of the transverse location of the damage path is the use of more data like the roll signal. This, however, would call out for a more complex external dynamics grounding model, implicating the need of a model which uses more degrees of freedom. Table 18, Table 19 and Figure 58 show that varying the value of the inertias has a substantial influence on the damage path, however, if the ratio between the inertias remains fixed the damage path is not affected. This shows that the method strongly relies on the ratio of the accelerations/forces. If the inertia ratios remain the same to one another, so will the accelerations/forces. Also, from the results of the sensitivity study is concluded that the effect of the variation of inertia on the shape of the damage path is small.

It is seen that determination of the FPOI in the case of impact of the rock on CL is not possible because there are only surge accelerations measured. However, in a real grounding an exact impact on CL does not happen. So there will always be sway accelerations to work with. But let's say that there are only surge accelerations measured and a way must be found to still come up with the longitudinal location of the damage path, more information would be needed to estimate it, for example: the measured pitch signal during the grounding.

The validity of the method could be checked more thoroughly if a large-scale grounding experiment would be performed which hits the rock off centre.

6

Discussion, conclusions & recommendations

The grounding of MV Rena. October 5, 2011. Tauranga, New Zealand.

6.1. Discussion

From the investigation into the acceleration signals measured on board the Nedlloyd57 it is found that it is possible to observe how the structure responds to the impact with the rock. This is true, however, for this particular case where the accelerometer was placed around 30 m away from the impact with the rock. The question is if this is still observable when measured on larger ships, where more space can be in between the impact location and the location of measurement. In case of lower energy grounding scenarios, the observability of this event in the acceleration signal could be lost. However, the fact that the same effects were also observed from measurements in small-scale experiments [24] and the other large-scale experiment carried out by the NSWC ([9], [10]) supports the conclusion.

The three DoF external dynamics grounding model was based on assumptions discussed in section 4.6.1. An assumption was that some parameters are constant in time. One of these parameters is the added mass in surge, sway and yaw. In the literature is found that this is not the case during a real grounding event. However, it was assumed constant for most analytical models because of the short duration of most groundings. For the damage calculation model and the inverse calculation model it would be interesting to define a time-varying added mass in each direction. Another parameter which was assumed time independent is the grounding force. A time-varying grounding force should be used if the effect observed in the large-scale experiments (TNO-ASIS and NSWC) is modeled. This would couple the external dynamics of the model from chapter 4 and 5 with the internal mechanics from the analysis from chapter 3. The coupling of both sides of the grounding problem is emphasized by Tabri [21].

The TNO-ASIS large-scale experiment and the damage prediction model both work with a single rock assumed as a point penetrating the ship. In general, a seabed topology is made up of more protruding pinnacles which could all make contact with the ship. In such a grounding scenario it would be harder to distinguish certain aspects of the grounding in the acceleration time-traces as clearly as is observed in the large-scale experiments. Consequently making it harder to make an assessment of the damage and damage location.

As discussed in chapter 4, in order to get to know more about the FPOI in the case of impact of the rock on CL, more motion data must be looked at to make a correct estimate. For a good assessment of the rock contact path location it is important to include more data such as pitch and roll. This calls for the need of a more advanced external dynamics grounding model, which includes more degrees of freedom.

6.2. Conclusions

To answer the research question three sub-questions were posed and answered in the three corresponding chapters. The main research question was:

Can the extent of the raking damage by assessed using the deceleration time-traces measured during a grounding incident?

The extent of the raking damage is categorized in the magnitude of the damage (how the local ship structure is affected by the grounding) and the location of the damage (how the grounding affects the ship globally: the same damage in different areas can have different consequences). The first is investigated by asking the sub-question: *How can acceleration time-traces be related to damage?* An analysis of the accelerations measured during the TNO-ASIS large-scale grounding experiment was performed to investigate this. It is seen that in the case of the large-scale grounding test it is possible to

observe from the acceleration time-traces how the structure responds to the contact with the rock. It is possible to observe the periodic impact with the transverse structural members in the double bottom test-section. The placement of the accelerometer around midship, around L/2 away from the impact location, does not influence this observability of this effect. The analysis shows that a double integration of the surge acceleration signal can serve as a quick assessment of the damage length.

From the absorbed energy a lot is learned about the raking damage extent. The absorbed energy was calculated from the acceleration signal in surge only and compared the absorbed energy calculated by force-path integration and to the reported damage and pitch angle. It is found that when the energy absorption rate increases, there is more deformation. Just after rupture, the energy absorption rate decreases because of lost structural integrity and resistance. It is concluded that the acceleration time-traces can be used to tell how much deformation is present at a certain moment in time relative to anywhere else in the signal, when rupture occurs and at what time and distance this happens.

Summarizing the experimental data analysis: it is possible to extract information on the damage and the location of the damage on the ship bottom from acceleration time-traces. This determination serves as an indication of how many compartments are involved in the damage.

A damage calculation model is made in Chapter 4 and 5. The sub-question that was posed was: *What is the damage path resulting from grounding force?* The model was validated against the large-scale experiment first. Using the model an estimation of the damage length can be done. A factor that influences the simulation's results is the estimated inertia. Good agreement is found in the results of the model and the literature model for smaller damage paths. Differences in results become larger for longer damage paths. These is explained by the omission of the damping term in the motion equation. However, for smaller damage paths (in the case used for the validation: damage length which are < L/3 m) the effect of the omission of damping is negligible.

It was reasoned that in a real grounding event the only thing known at the time is the initial velocity at the moment of grounding and the accelerations measured on board. Therefore the third and last sub-question was asked in Chapter 5 to tie it all together: *Can the rock bottom contact path be derived using only accelerations?* The presented inverse of the damage calculation model which only uses this information to find the location of the damage can reproduce the damage paths and the first point of impact of the rock on the ship bottom satisfactorily. The method relies most importantly on the ship's inertias. From the sensitivity study of this inverse method it is concluded that variation of the inertia or initial velocity influences the estimation of the location of the damage path. It is seen that the effect of this variation has more effect in transverse direction than in longitudinal direction. However, it is reasoned that a deviation of the location of the damage path in longitudinal direction has more implication on the ship's damage stability than a deviation in transverse direction, although this deviation is larger. What could help the determination of the transverse location of the damage path is the use of more motion data like roll and pitch. This, however, would call out for a more complex external dynamics grounding model. From the sensitivity study is also concluded that the effect of the variation of inertia on the shape of the damage path is small. When the ratio between the inertias remain fixed, the damage path is not affected. The method strongly relies on the ratio of the accelerations/forces. This calls for an accurate measurement of the acceleration on board in each DoF.

It is seen that determination of the FPOI in the case of impact of the rock on CL is not possible because there are only surge accelerations measured. However, in a real grounding an exact impact on CL does not happen. So there will always be sway accelerations to work with. But let's say that there are only surge accelerations measured and a way must be found to still come up with the longitudinal location of the damage path, more information would be needed to estimate it, for example: the measured pitch signal during the grounding.

It is noted that accelerations observed on the Nedloyd57 are a maximum of -5 m/s^2 (-0.5g) in surge and in sway and heave a maximum of 3 m/s^2 (0.3g). Typical acceleration levels determined on the VLCC do not exceed 0.2 m/s^2 (0.02 g). This implies the need for accelerometers with sufficient sensitivity. The large-scale experiment is a high energy grounding where large decelerations are measured (in de order of ±10 m/s^2). But in the case of lighter groundings, a more sensitive accelerometer is preferable (in the order of ±1 m/s^2). In future applications of the method, it would be advisable to install more accelerometers on board with each a different sensitivity.

Summarizing all conclusions the main question yields the following conclusions:

Can the extent of the raking damage by assessed using the deceleration time-traces measured during a grounding incident?

Magnitude of damage	Location of damage
From an analysis of experimental data of the large-scale grounding test can be concluded that the magnitude of the damage can be evaluated. Plastic deformation and rupture of the plate can be detected from only the acceleration time-traces.	From an investigation using an analytical calculation model can be concluded that the location of the damage path can be assessed with reasonable accuracy. Varying main parameters in the model still yields good results.

6.3. Recommendations

6.3.1. Application

This research provided a first exploratory step into developing a tool which can help assess the situation just after a grounding incident directly on the bridge. This tool will be able to assess the raking damage by using acceleration measurements. It is envisioned that the tool will be able to use this damage prediction to identify the extent of the damage and the location of the damage. Summarizing the research, it can be concluded that the tool could use the accelerations to identify the extent of the damage e.g. rupture or not. Also, the tool could use the accelerations and pitch angle time-traces to get the damage length and consequently make an assessment of the location of the damage path along the ship bottom. The assessment should follow up with a visual check of the involved compartments just after the grounding event. The assessment gives a reason to prioritize that part of the ship that was estimated to be damaged. The compartments involved in this part of the ship would be advised to check first before checking adjacent compartments and so on.

It is envisioned that the tool would have functionalities as is presented in Appendix G, which shows a concept of how the application's interface could look like. Accelerometers can be installed all over the ship because these sensors are in-expensive. These will send data to the toolbox. The toolbox would be a useful tool in the making of an assessment of the situation by the user and assist in the determination what steps to undertake or decide.

6.3.2. Further research

It is found how the raking damage can be assessed based on acceleration time-traces. However, before an application such as described in section 6.3.1 can be implemented on ships in the future, more research on this topic should be done. Several recommendations are made in this section for future research.

Expanding the model

More research is required in order to expand the damage calculation model. Adding more degrees of freedom would more realistically model a grounding event. Adding more degrees of freedom would allow for the investigation into the estimation of the vertical extent of the damage as well.

The damage calculation model can be expanded by adding time-varying added mass and time-varying grounding force. Before this can be done, more research must be performed on the topic of the added mass variation during grounding.

It is reasoned that the extent of the raking damage also includes the location of the damage. The same damage in a different part of the ship yields different consequences. This asks for a study which investigates how a certain damage on the hull influences how many compartments are hit and what this does on the ship's damage stability.

Additional experiments

It would be interesting if a large-scale grounding test which hits the rock off centre would be performed. With this experiment an investigation can be done into for example the behaviour of the ship motions under anti-symmetric grounding or the crash resistance of the double bottom in transverse direction. An idea for a grounding scenario is to hit the rock mainly at the bilge and discover how the roll motion influences both the longitudinal and the vertical extent of the damage. Staying on the topic of accelerations, with this experiment an investigation into how the acceleration time-traces can be related to the damage in case of a grounding scenario with large rock eccentricity would be interesting to carry out.

Further research into the placement of accelerometers on the ship should be done. By placing multiple accelerometers on board, not only at CoG of the ship but also for example at the bow and at the stern and in between, one could investigate how location of the sensors influence how the damage at a particular location is detected, or they could investigate how the ship structure in between measuring locations influences the recorded damage's acceleration.

Assessment of the damage and the situation on board

Another idea for how the tool can be made is by doing numerical simulations as described. The ship on which the tool will be installed on can be modeled and can be subjected to simulations like this. All sorts of rocks can be modeled and the ship will be crashed onto it at different locations. Doing a lot of these simulations will yield in a lot of acceleration signals as a result. The ship in question now has simulated acceleration signals for certain grounding scenarios ready to be used if a grounding incident occurs. The measured acceleration signal during the grounding can be compared to all the simulated signals. A signal which resembles the measured one could give an indication of the scenario in the sense of extent of the damage, rock size, impact location, grounding force, etc.

What should also be investigated before the discussed helping tool can be implemented on board is the effect of the grounding damage on the severity of the situation on board. Studies into how the damage stability of the ship can be assessed quickly because of a certain raking damage must be carried out. Such studies would proof useful if one wanted determine the severity of the situation on board in a certain grounding scenario on the bridge: is the ship safe or must the ship be abandoned.

Numerical model

It was intended to perform a numerical simulation as well in the last phase of the research. However, making a realistic model proofed more difficult in the small timeframe left for this investigation. The main goal of performing a numerical simulation was to have not only a validation of the analytical models against experimental data and against another model

from literature but also have a validation against numerical experimental data. Also it would mean more investigation into the coupling of internal mechanics and external dynamics.

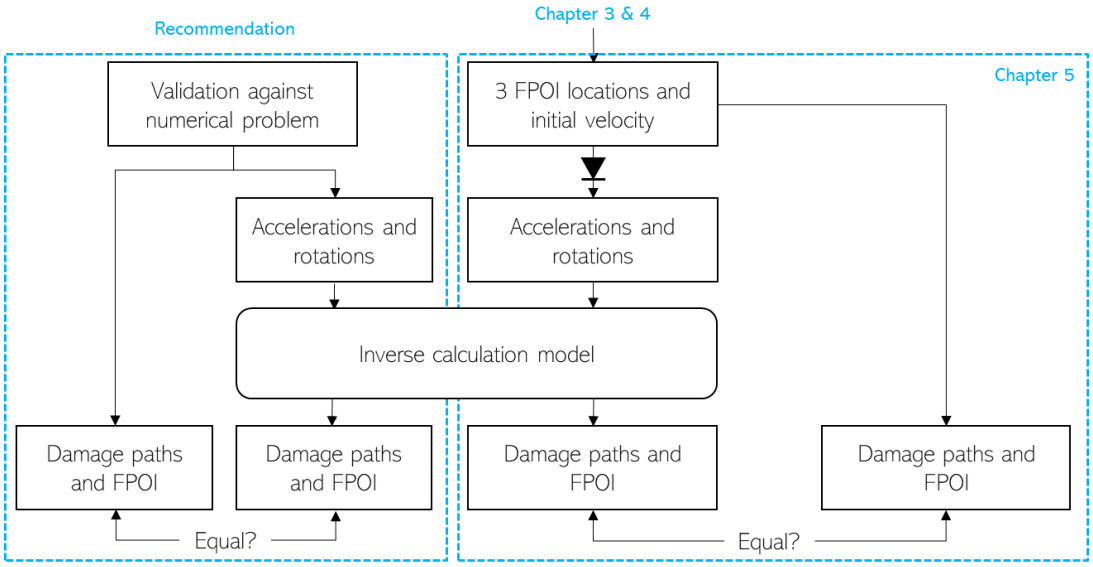

Figure 62 Visualization validation against numerical problem

The idea was to take a ship model with detailed ship structure including, most importantly for the sake of the surge acceleration pattern, transverse floors and bulkheads. The simulation will let the ship model hit a rigid rock. Trim angle is implemented so that rock gradually penetrates the ship model vertically. Give the ship model a large enough initial velocity so that the rock penetrates the ship deep enough vertically for the largest effect of the rock impacting with all three bulkheads. Run the simulation and obtain accelerations from the ship model. Use these accelerations as input for the inverse method calculation model. Calculate with the method the location of first impact and the shape of the damage path.

The proposed methodology is: simulate a couple of grounding scenarios, meaning different first impact locations, for example, the three scenarios in chapter 5, with impact on CL and impact off centre. It is also interesting to simulate the scenarios using different rock types, for example: sharp, rounded, wide and rounded, as depicted in Figure 63. With these simulations investigate what kind of difference can be observed from the acceleration signal if different rocks are hit in the same grounding scenario.

Figure 64 shows the trimmed single hull ship model and the rigid rock. The last picture in this figure shows half of the model, which more clearly shows the ship structure and the three bulkheads. The ship is restrained in vertical direction at the front and the back nodes of the model. This is done because in a first simulation, as soon as the ship hits the rock, the ship bounces up vertically and continues on that path because there are no other external loads applied to it. The ship has to be restrained in some way in order to make the rock penetrate the ship hull.

With these simulations I hoped to see a pattern as in Figure 19 in the resulting acceleration signals. The idea was to put these into the inverse calculation model and perform the same investigation into finding the correct FPOI and damage path as is done for the three grounding scenarios in chapter 5 using the inertias and dimensions of the numerical model. This would be able to validate the inverse method some more.

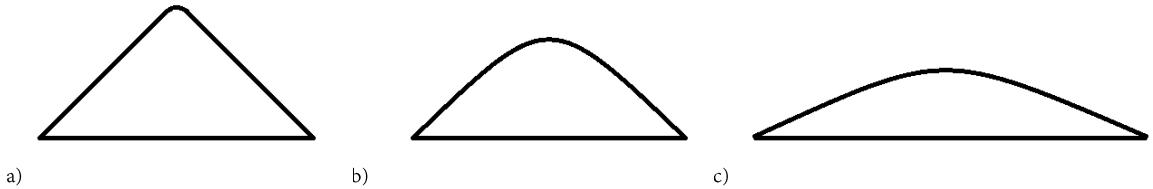

Figure 63 Rock types. a) Sharp. b) Rounded. c) Wide and rounded.

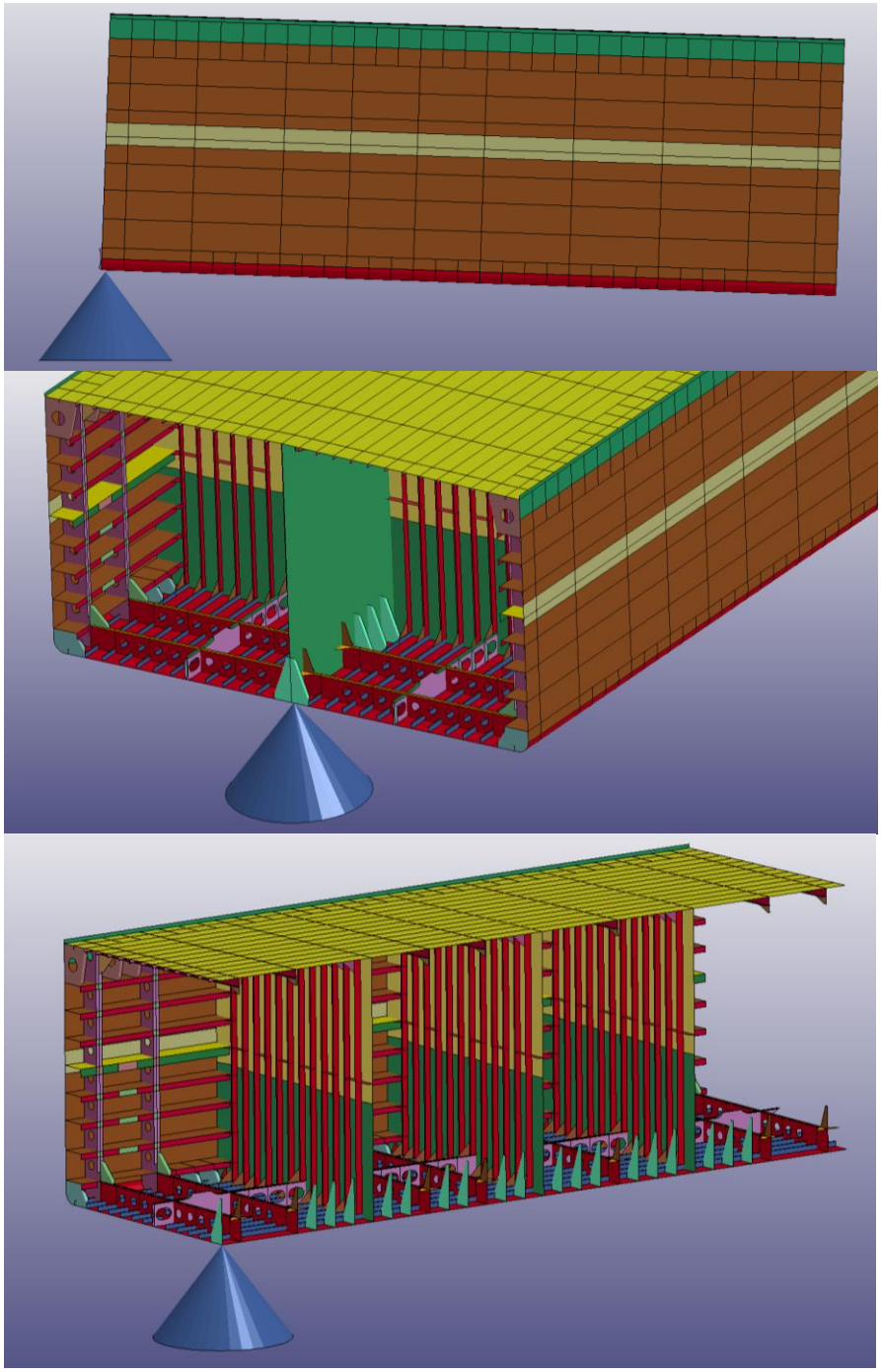

Figure 64 Sideview, 3D view of the whole and 3D view of half of the ship model and rock type a on CL in LS Pre-post

Bibliography

[1] A. Vredeveldt and L. Wevers, "ROYAL SCHELDE REPORT version 01 - Full scale ship grounding experiments with modified double hull structure," Delft, 1996.

[2] B. Simonsen, "Mechanics of Ship Grounding," DTU, Department of Naval Architecture and Offshore Engineering, Lyngby, 1997.

[3] European Maritime Safety Agency, "Evaluation of risk from raking damages due to grounding, Final report," DNV GL, 2015.

[4] G. Wang, H. Ohtsubo and D. Liu, "A Simple Method for Predicting the Grounding Strength of Ships," *Journal of Ship Research,* vol. 41, no. 3, pp. 241-247, 1997.

[5] Ministry of Infrastructures and Transports - Maritime Casualties Investigative Body, "Cruise ship Costa Concordia - Report on the safety technical investigation," Jan 2012.

[6] "NAPA Flooding Simulation," NAPA, [Online]. Available: https://www.napa.fi/Design-Solutions/NAPA-Statutory-Compliance/NAPA-Flooding-Simulation.

[7] Wärtsilä, "GMDSS (Global Maritime Distress and Safety System)," [Online]. Available: https://www.wartsila.com/encyclopedia/term/gmdss-(global-maritime-distress-and-safety-system).

[8] J. Pinkster, P. Lemmen and A. Vredeveldt, "Design analysis for grounding experiments," in *International Conference on Designs and Grounding Protection of Ships*, San Fransisco, 1996.

[9] J. Rodd and J. Sikora, "Double Hull Grounding Experiments," in *International Offshore and Polar Engineering Conference*, The Hague, 1995.

[10] L. Rodd, "Large scale tanker grounding experiments," in *International Offshore and Polar Engineering Conference*, Los Angeles, 1996.

[11] V. Minorsky, "An analysis of ship collisions with reference to protection of nuclear power plants," *Journal of Ship Research,* vol. 3, pp. 1-4, 1959.

[12] B. Simonsen and T. Wierzbicki, "Grounding Bottom Damage and Ship Motion over a Rock," *International Journal of Offshore and Polar Engineering,* vol. 6, no. 3, pp. 195-202, 1996.

[13] B. Simonsen, "Ship Grounding on Rock - I. Theory," *Elsevier,* vol. Marine Structures 10, pp. 519-562, 1998.

[14] B. Simonsen, "Ship Grounding on Rock - II. Validation and Application," *Elsevier,* vol. Marine Structures 10, pp. 563-584, 1998.

[15] H. Alsos, J. Amdahl and O. Hopperstad, "On the resistance to penetration of stiffened plates, Part II: Numerical analysis," *Elsevier,* vol. International Journal of Impact Engineering 3, pp. 875-887, 2009.

[16] M. Heinvee and K. Tabri, "A simplified method to predict grounding damage of double bottom tankers," *Elsevier,* vol. Marine structures 43, pp. 22-43, 2015.

[17] B. Simonsen, R. Törnqvist and M. Lützen, "A simplified grounding damage prediction method and its application in modern damage stability requirements," *Elsevier Marine Structures,* vol. 22, pp. 62-83, 2009.

[18] P. Pedersen and S. Zhang, "Absorbed Energy in Ship Collisions and Grounding - Revising Minorsky's Emperical Method," *Journal of Ship Research,* vol. 44, no. 2, pp. 140-154, 2000.

[19] G. Wang, K. Arita and D. Liu, "Behavior of a double hull in a variety of stranding or collision scenarios," *Elsevier Marine Structures,* vol. 13, pp. 147-187, 2000.

[20] T.-H. Nguyen, J. Amdahl, J. Leira and L. Garrè, "Understanding ship-grounding events," *Elsevier Marine Structures,* vol. 24, pp. 551-569, 2011.

[21] K. Tabri, "Dyamics of ship collisions," Aalto University, department of Applied Mechanics, Espoo, 2010.

[22] P. Pedersen and S. Zhang, "On impact mechanics in ship collisions," *Elsevier Marine Structures,* vol. 11, pp. 429-449, 1998.

[23] S. Zhang, "Plate tearing and bottom damage in ship grounding," *Elsevier,* no. Marine Structures 15, pp. 101-117, 2002.

[24] S. Haag, "Ship grounding damage - an estimate through acceleration measurements," TU Delft, marine technology, Delft, 2017.

[25] Y. Li and Z. Wang, "An Approximate Analytical Solution of Sloshing Frequencies for a Liquid in Various Shape Aqueducts," *Shock and Vibration,* vol. 2014, March 2014.

[26] N. Salvesen, E. Tuck and O. Faltinsen, "Ship Motions and Sea Loads," *SNAME,* no. 78, pp. 250-287, 1970.

[27] T. Fossen, Handbook of Marine Craft Hydrodynamics and Motion control, Trondheim: John Wiley & Sons, Ltd, 2011.

[28] J. Journée and J. Pinkster, Introduction in Ship Hydromechanics, TU Delft: College notes, 2002.

[29] S. Sagatun and T. Fossen, "Lagrangian formulation of underwater vehicles'dynamics," Trondheim, 1991.

[30] "MATLAB®," Mathworks, 2017. [Online]. Available: https://nl.mathworks.com/help/matlab/.

[31] D. Watson, Practical ship design, Oxford: Elsevier, 1998.

[32] Z. L., J. P. and Z. S., "Statistics and damage assessment of ship grounding," *Elsevier Marine Structures,* no. 15, pp. 515-530, 2002.

[33] M. Triantafyllou and F. Hover, Maneuvering and control of marine vehicles, 2003.

Internet pages

Paragraph 1.3.2, p. 16, information on NAPA, https://www.napa.fi/Design-Solutions/NAPA-Statutory-Compliance/NAPA-Flooding-Simulation

Paragraph 3.3.2, p. 54, speed of sound in structural steel, http://hyperphysics.phy-astr.gsu.edu/hbase/Sound/souspe2.html

Paragraph 5.4.1, p. 95, uncertainty of GPS systems, https://www.gps.gov/systems/gps/performance/accuracy/#speed

Images

Title page images

Chapter 1: 'The grounding of MV Benita', gCaptain, http://gcaptain.com/refloating-made-possible-dyneema/

Chapter 2: 'The grounding of the Princess May', Silodrome, https://silodrome.com/grounding-princess-may/

Chapter 3: 'The grounding of Pasha Bulker', Wikipedia, https://en.wikipedia.org/wiki/File:Pasha_Bulker04.jpg

Chapter 4: 'The grounding of the Transocean Winner', The Times, https://www.thetimes.co.uk/article/worst-case-scenario-at-grounded-oil-rig-is-52-tonne-diesel-spillage-v96ljqwrm

Chapter 5: 'The grounding of the Maersk Connector. When grounding is part of the job.', Maersk, https://www.maersk.com/stories/when-grounding-is-part-of-the-job

Chapter 6: 'The grounding of MV Rena', Wikipedia, https://en.wikipedia.org/wiki/MV_Rena

Other images

Figure 3, Damage to the Costa Concordia, Wikimedia commons

Paragraph 4.1, p. 65 and paragraph **Error! Reference source not found.**, p. **Error! Bookmark not defined.**, DAMEN

Appendices

Contents

Appendix A

Damage report

This appendix presents twelve chronologically arranged photographs taken during the TNO-ASIS grounding test. Picture 3 shows the crash of the tube mounted on the ship with the tube mounted on top of the rock. This ensures that all measurements start at the same time.

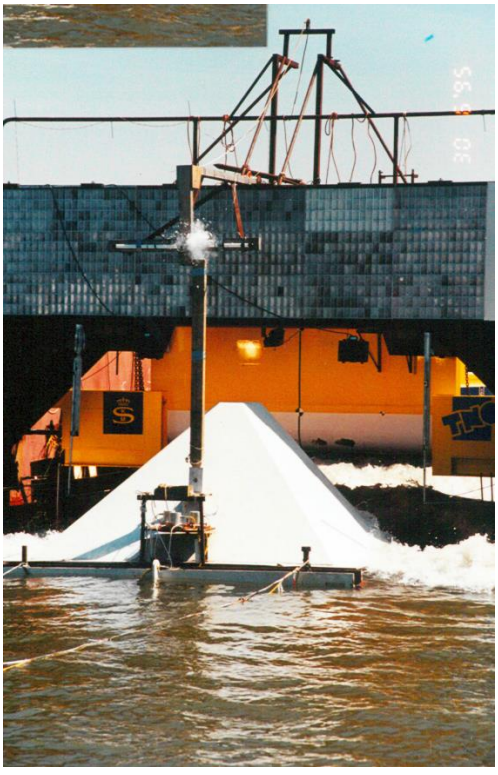

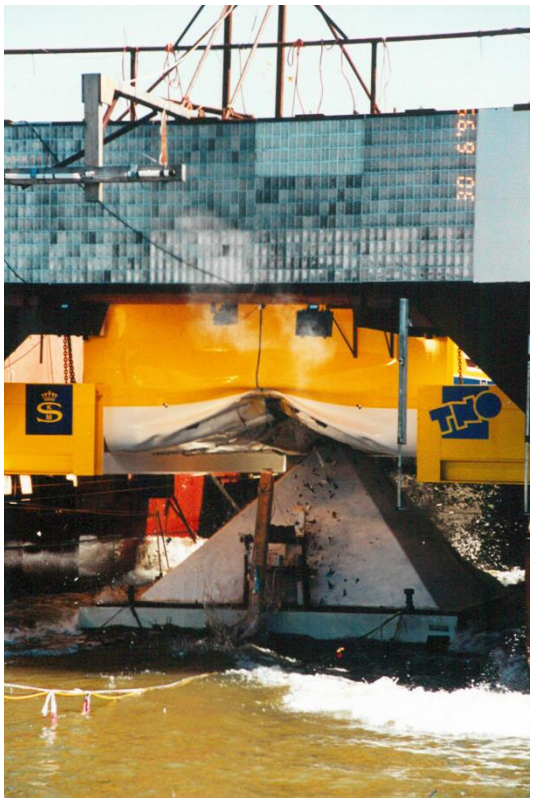

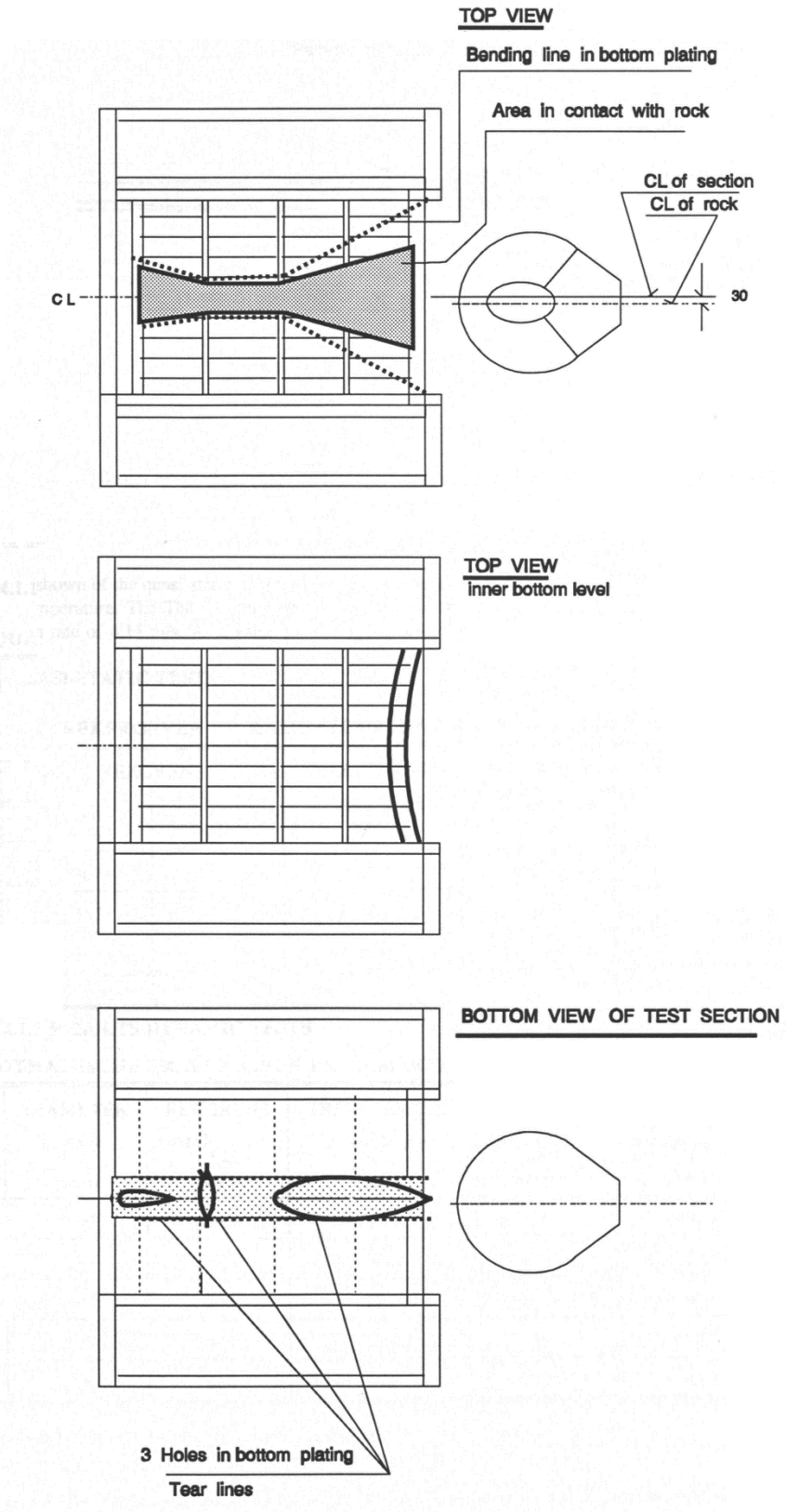

Top view and bottom view of the test-section mounted on the support ship. The left side of the test-section is the backside, the right side is the front. The top picture shows the eccentricity of the rock from the CL of the test-section and the deformation. The middle picture shows the bending of the front of the test-section. The lower picture shows the bottom view of the test-section together with the deformation and the tears in the hull.

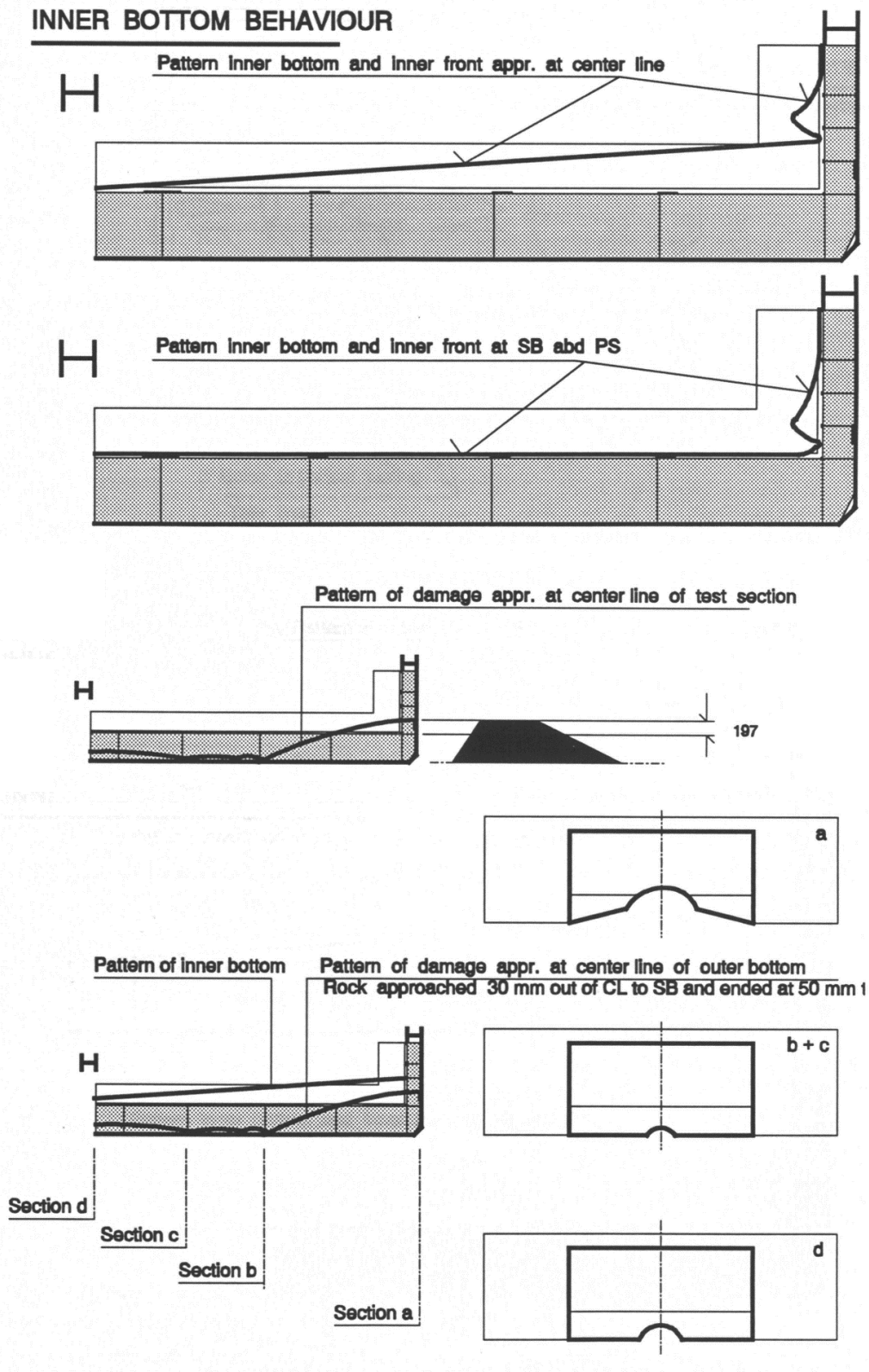

The upper picture shows the side view of the test-section. The deformation of the inner shell in the middle and at the sides are shown. The lower pictures show sections of the deformation of the test-section seen from the front.

Appendix B

Measurement systems

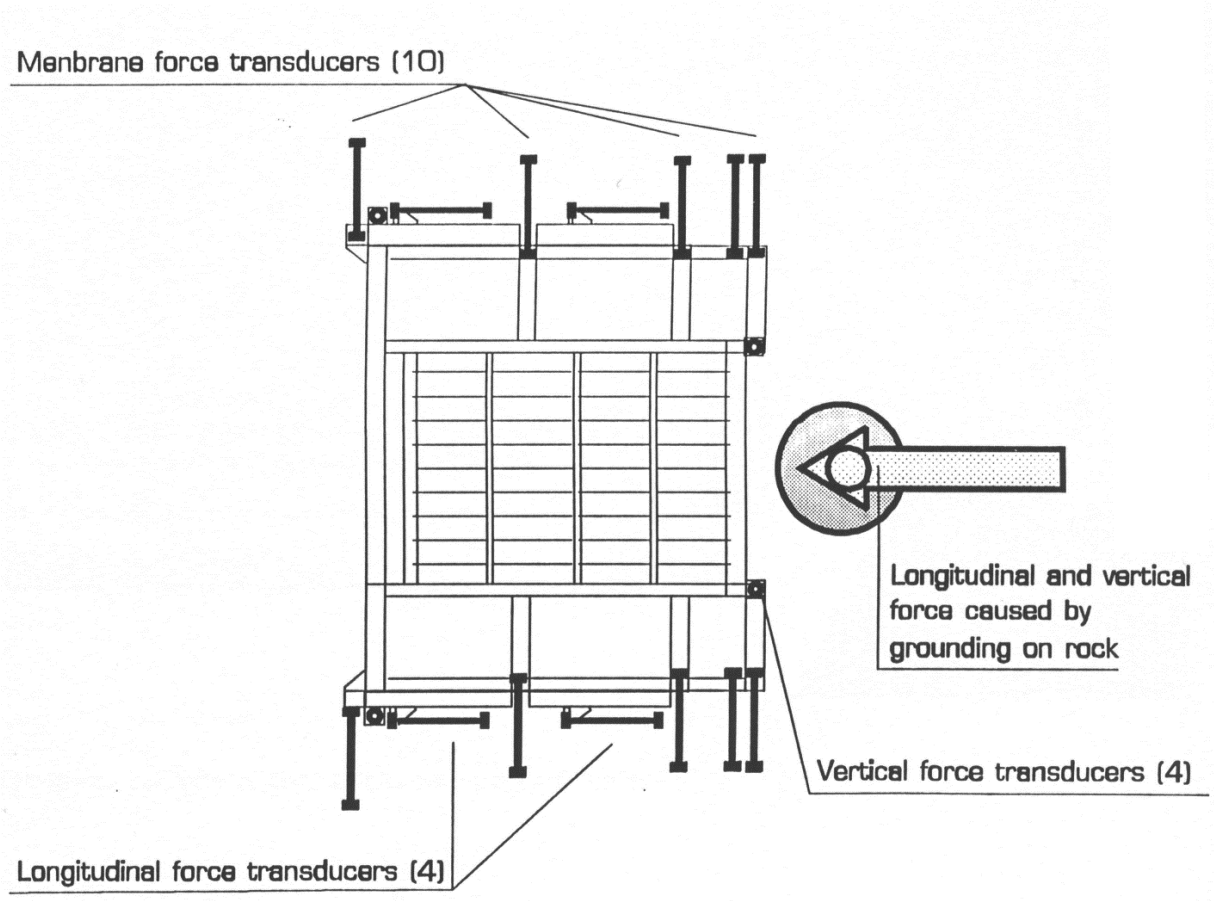

Location of the load cells on the test-section. The test-section is mounted in between the H-shaped hull of the support ship using these rods. The rock is pictured on the right side and it's resulting grounding force on the test-section is pictured on top of it.

Between rock and support structure on the pontoon 6 load cells were used, see figure 2.4.3. In this way the system was stacticaly determined.

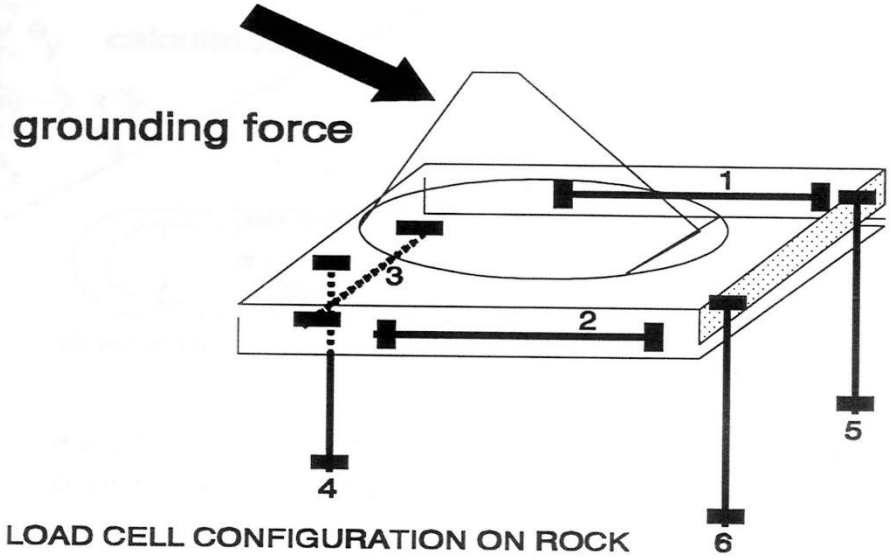

Figure 2.4.3 Load cell arrangement at the rock

Configuration:	longitudinal direction	2 (channel 1, 2)
	vertical direction	3 (channel 4,5 and 6)
	transverse direction	1 (channel 3)

As far as possible principles of symmetry were used to obtain the possibility of an extra check and also interchange of signals in case of partial failure.

2.4.1 Load cells

To measure loading forces, tensile bars with a large length / diameter ratio were used. In this way it could be made sure that only tensile forces could be measured. The transverse loadings could not be more then 1/1000 of the tensile loadings. Furthermore the bars were rather cheap to manufacture and easy to handle. A maximum of 2300 kN could be loaded. Details, dimensions and material qualities are given in figure 2.4.2.

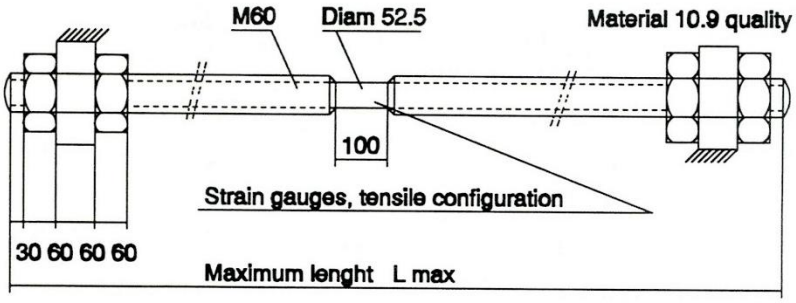

Sections	vertical: 1200		Rock	vertical: 2000
	long: 1600			long: 2000
	transv: 2000			transv: 2000

LOAD CELL MEASURES FOR TENSILE FORCE MEASUREMENTS

Figure 2.4.2 Load cell dimensions

The configuration of load cells between test section and ship is shows in Appendix A.

Amount of load cells used:	longitudinal direction	4
	vertical direction	4
	transverse direction	
	for grounding test 1, 2	10 (5 SB and 5 PS)
	for grounding test 3	4 (2 SB and 2 PS)

Material quality 10.9:	tensile strength	1000(nom)	1040(max)	N/mm^2
	vickers	320(min)	380(max)	N/mm^2
	yielding (0.2% strain)	900 (nom)	940(max)	N/mm^2
	elongation till fracture	9		%
	sharpy V test	>20		J

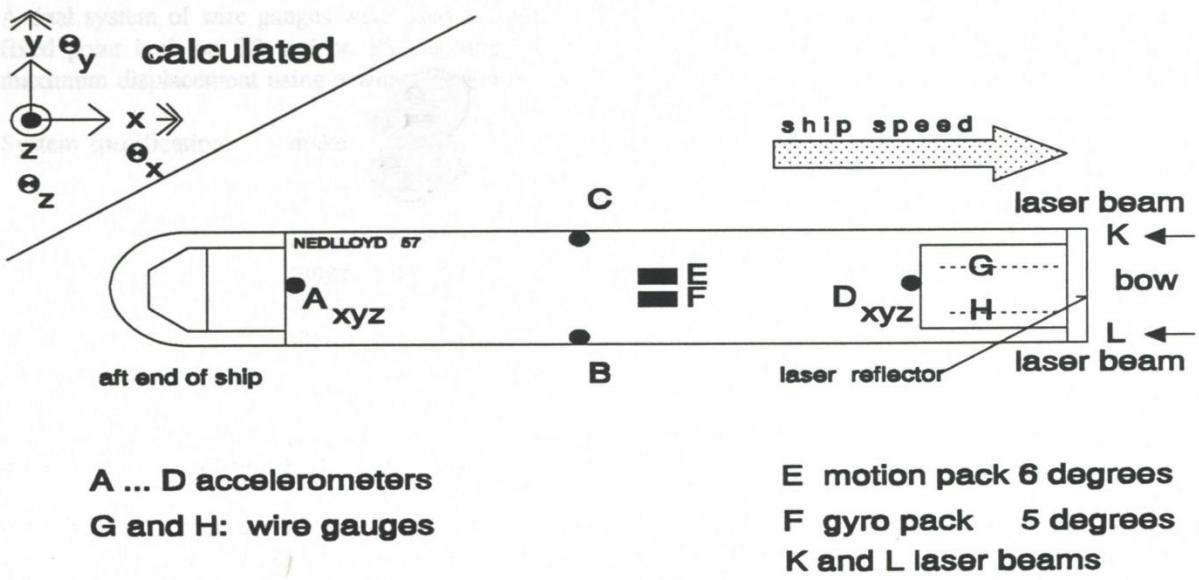

Figure 2.4.4 Location of accelerometers, wire gauges and laser reflectors on board Nedlloyd 57

System specifications

Motion pack TNO: make Systron Donner Inertial Division
model# MP1, Serial# 0167, October 31, 1994
scale factor rate channels x,y,z 25 ± 0.250 mV/°/s
scale factor acceleration x,y,z 1.50 ± 0.015 V/g

Location of accelerometers, wire gauges and laser reflectors on board of the support ship 'Nedlloyd 57'. The laser beams measure the distance between the ship and the outpost (where i.a. the measuring equipment is stored). The lasers reflect on the reflective panels in the picture (grey panels above test-section).

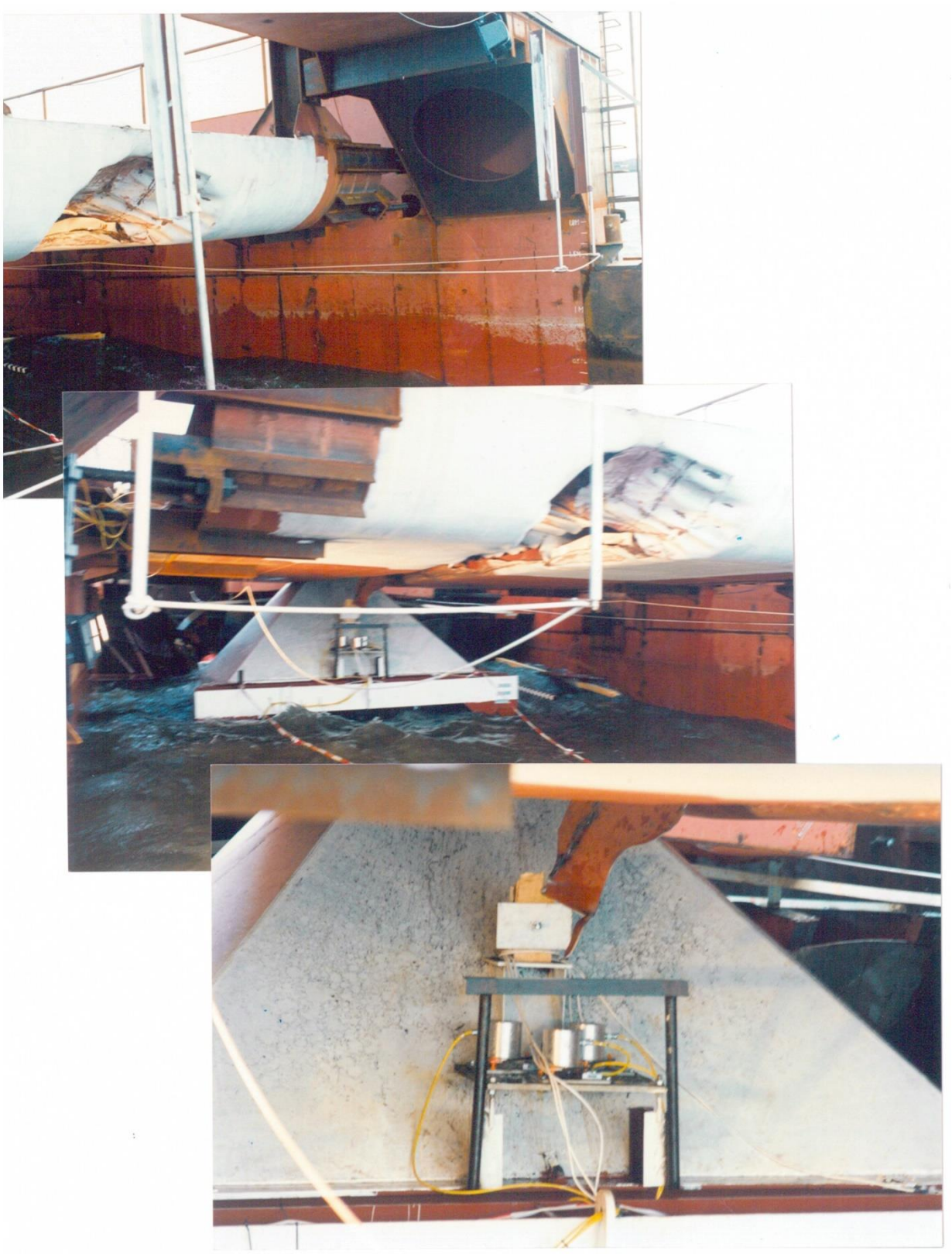

Three pictures of the wire gauge set up (from a test with another test-section, but with a similar working). When the ship closes in on the rock, a hook attached to the rock set-up pulls the wire with it. The wire in the gauge is pulled from a winch and the gauge measures how much rope is pulled from it. **Upper picture:** pulled wire visible. **Middle picture:** Just after the test, the rock is stuck inside the test-section. The stretched wire is visible in the fore- and background. **Lower picture:** Close-up of accelerometers attached to the rock base.

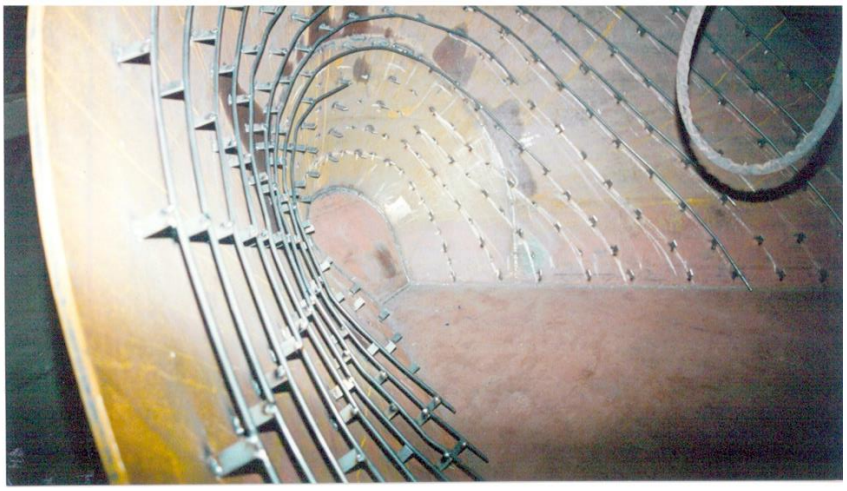

The rock is assumed to be 'rigid' in the grounding tests. The rock is made of ferroconcrete covered with a steel plate of 15 mm thickness. The rock is fitted onto a frame on a pontoon. The pontoon is fully submerged and only the rock is visible above the waterline.

Appendix C

General information on support ship 'Nedlloyd 57'

Table, main particulars of support ship (after conversion)

Length o.a.	68.30	[m]
Beam moulded	9.40	[m]
Width between 'catamaran' hulls	6.96	[m]
Approximate displacement during tests	600.00	[t]

Table, Loading condition and calculated inertia's

Surge, M_x	680.74	[t]
Sway, M_y	840.00	[t]
Yaw, I_z	174908.76	[tm^2]
Longitudinal centre of gravity, L_{cog}	24.96	[m]

Table, additional data of grounding test

Initial velocity before grounding, v_0	3.73	[m/s]
Rock offset from CL, μ	0.30	[m]
Average grounding force, F_G	0.41	[MN]
Measured stopping distance, X_s	7.00	[m]

Appendix D

Derivation of Coriolis matrix

Lagrangian mechanics [29], [33]

The development of rigid body inertial dynamics depends on the rates of change of vectors expressed in a moving frame, the local frame of the ship. An alternative approach is to use the lagrangian, wherein the dynamic behavior follows directly from consideration of the kinetic co-energy of the vehicle; the end result is exactly the same as the Newtonian approach. The core difference between Newtonian and Lagrangian mechanics is that while the former says that the forces acting on a body determine its acceleration, the latter describes the principle of least action: there is a quantity called the action, and a system takes a path that yields the minimal value of this action. The main advantage of Lagrangian dynamics is that the forces of constraints don't have to be considered and given the total kinetic and potential energies of the system some generalized coordinates can be chosen. Here, one can blindly calculate the equation of motions totally analytically unlike Newtonian case where one has to consider the constraints and the geometrical nature of the system. The method is used in the ship's equation of motion to also take into account the ship's added inertia by the ambient water. Here a derivation of this added inertia for the surge, sway and yaw model is given. Instead of the notations used in this thesis, the notations of Sagatun & Fossen [29] is used to make a more clear derivation when compared to the literature [26].

Added mass in 3DoF: surge – sway – yaw. The added mass terms follow from the coupling terms from [26].

$$M_a = -\begin{bmatrix} X_{\dot{u}} & 0 & 0 \\ 0 & Y_{\dot{v}} & Y_{\dot{r}} \\ 0 & Y_{\dot{r}} & N_{\dot{r}} \end{bmatrix}, \text{with } N_{\dot{v}} = Y_{\dot{r}}$$

With velocity vector of the body, $\boldsymbol{q} = [u, v, r]^T$, the kinetic co-energy of the fluid E_k is

$$E_k = -\frac{1}{2}\boldsymbol{q}^T M_a \boldsymbol{q}$$
$$= -\frac{1}{2}(X_{\dot{u}}u^2 + Y_{\dot{v}}v^2 + 2Y_{\dot{r}}vr + N_{\dot{r}}r^2)$$

Kirchoff's relations are derived from the lagrangian approach. This derivation is done in [33]. Summarized, it states that the lagrangian, L = E_K. Which is the kinetic co-energy minus the potential energy of the system. Since the considered motion of a body in an unbounded, homogeneous fluid, there is no potential energy, so the lagrangian is exactly the kinetic energy. Kirchoff's relations are used to derive fluid inertia terms in the body-referenced equations of motion, with **v** = [u,v,0], the velocity vector, and $\boldsymbol{\omega}$ = [0,0,r], the angular velocity vector.

$$\boldsymbol{F} = -\frac{\partial}{\partial t}\left(\frac{\partial E_k}{\partial \boldsymbol{v}}\right) - \boldsymbol{\omega} \times \frac{\partial E_k}{\partial \boldsymbol{v}}$$
$$\boldsymbol{Q} = -\frac{\partial}{\partial t}\left(\frac{\partial E_k}{\partial \boldsymbol{\omega}}\right) - \boldsymbol{\omega} \times \frac{\partial E_k}{\partial \boldsymbol{\omega}} - \boldsymbol{v} \times \frac{\partial E_k}{\partial \boldsymbol{v}}$$

With **F** = [X,Y,Z], the force vector, and Q = [K,M,N], the moment vector. Substituting E_k into **F** and **Q** gives

$$X = X_{\dot{u}}\dot{u} - Y_{\dot{v}}vr - Y_{\dot{r}}r^2$$
$$Y = Y_{\dot{v}}\dot{v} - Y_{\dot{r}}\dot{r} + X_{\dot{u}}ur$$
$$N = N_{\dot{r}}\dot{r} + Y_{\dot{r}}\dot{v} - (X_{\dot{u}} - Y_{\dot{v}})uv - Y_{\dot{r}}ur$$

The acceleration components belong to the inertia matrix as part of the added mass. The Coriolis term becomes

$$\boldsymbol{C}_A(\boldsymbol{v}) = -\boldsymbol{C}_A^T(\boldsymbol{v})$$
$$\boldsymbol{C}_A(\boldsymbol{v})\boldsymbol{v} = \begin{bmatrix} Y_{\dot{v}}vr + Y_{\dot{r}}r^2 \\ -X_{\dot{u}}ur \\ (X_{\dot{u}} - Y_{\dot{v}})uv + Y_{\dot{r}}ur \end{bmatrix}$$

Appendix E

Signal identification

A study has been performed on signal identification methods. Three methods are studied: fast Fourier transform (FFT), continuous wavelet transform (CWT) and Hilbert transform (HT).

Signals

The signals used for the analysis of these methods are depicted in Fig 1. The four types of signals are a square, triangular, sawtooth and a sine signal. The four periodic signal types are repeated ten times using a 50 Hz frequency resulting in a time span of 0.2 seconds. In the first row of Fig. 1, the signals are plotted repeatedly, in the second they decay and in the bottom row the signal is an impulse. The decaying signal is the repeated signal, but damped using the factor $e^{-t \cdot \lambda}$, using $\lambda = 25$. The impulse signal is exactly half of one period of the signal.

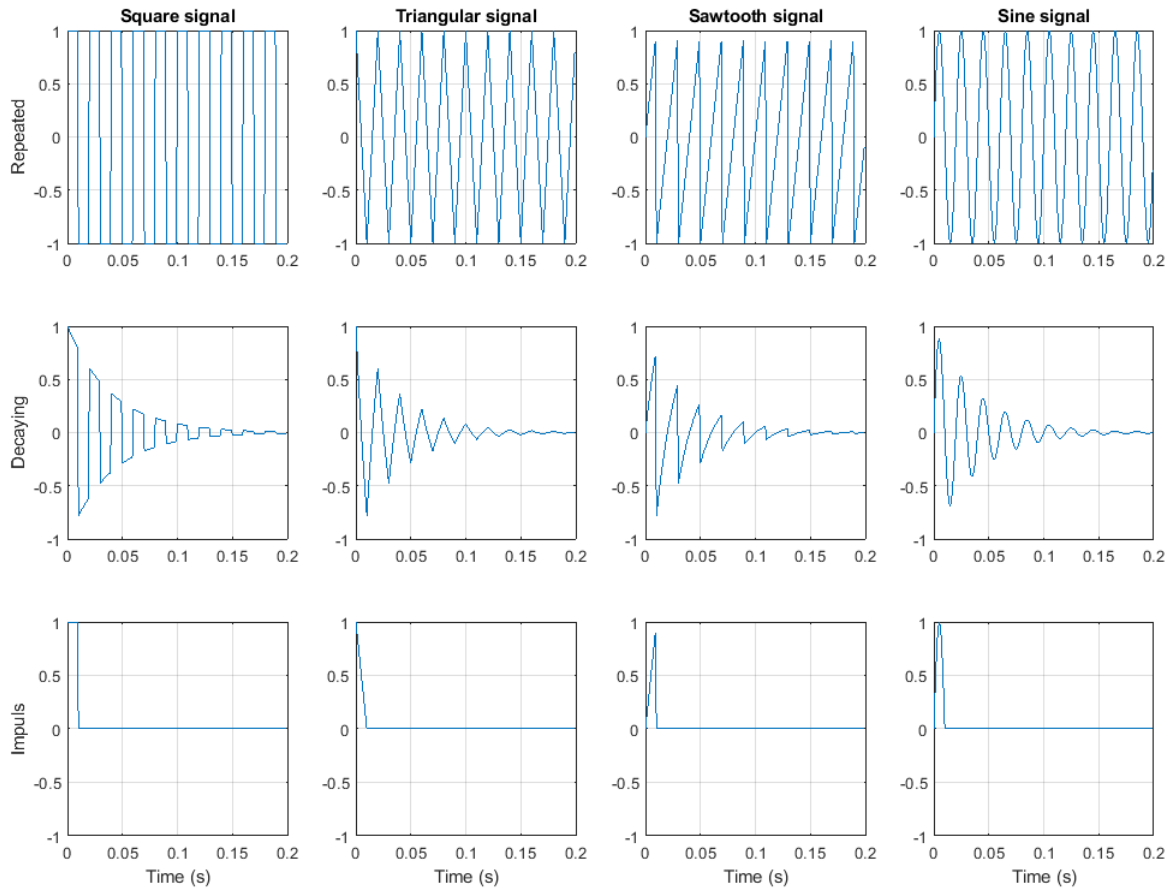

Fig. 1 Signals

Fourier transform and wavelet transform

First, the Fourier transform will be compared to another type of signal identification method: wavelet transform. In the Fourier transform, the signal is represented as a sum of sinusoids. As a matter of fact, the Fourier transform can be viewed as a type of wavelet transform. In order to explain this, the wavelet transform is now discussed.

The wavelet transform is done by choosing what is called a mother wavelet. The type of wavelet chosen as the mother wavelet has a certain effect on the outcome of the transform. The transform works with a scale factor *a*. This scale factor 'stretches' or 'compresses' the wavelet. When *a* is low, the wavelet is more contracted and the result is more detailed. When *a* is high, the wavelet is stretched out, resulting in the opposite. These scaled wavelets are the daughter wavelets of the mother wavelet. These daughter wavelets are then fitted along the signals shape in time. This is done for every scale factor, ranging from the lowest to the highest. Generally, the highest scale factor is chosen based on the time interval of the signal. A CWT plot of a signal can therefore be viewed as the time domain on the horizontal and the scale factors on the vertical axis. Consequently, the scale factors can be converted to frequencies. The vertical axis can therefore also be plotted in the frequency domain, making CWT an excellent method to identify certain frequencies in the signal and at the same time knowing when these frequencies occur in the time domain of the signal.

This explains why the Fourier transform can be viewed as a special case of the wavelet transform. In this case the mother wavelet has the form of a sinusoid. And this wavelet is scaled such that the resulting wavelet is a sinusoid with a particular frequency. The biggest difference between the two signal identification methods is that the WT is localized both in time and frequency, while the standard FT is only localized in frequency. This difference is at the same time the main advantage of WT over FT. Information on both frequency and time can be very useful in the identification of the signal. It can show when a certain event takes place during the measurement. This is important for signals which have abrupt changes, such as a beginning or end event (such as is shown in the force and acceleration time-traces of the large-scale grounding experiment). Other advantages are that WT can distinguish fine details from a signal. Using larger wavelets (large scale factor) coarser details in the signal can be found. Also, WT can be used on functions which have discontinuities and sharp peaks, or are non-periodic and non-stationary (such as the force and acceleration time-traces of the large-scale grounding experiment).

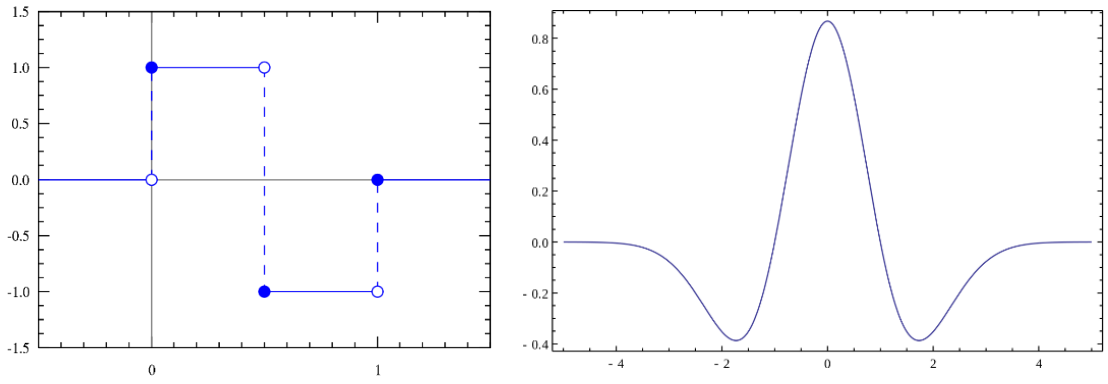

Fig. 2 Left: Haar wavelet (db1 wavelet); right: Mexican hat wavelet

The type of mother wavelet used in the transform has some influence on the result. In Fig. 2 two types of wavelets are shown, a Haar wavelet (or db1 wavelet) and a Ricker wavelet, or more generally known in programs such as MATLAB as the

Mexican hat wavelet. The effect of the type of wavelet chosen is presented in Fig. 3. Here the continuous wavelet transform is performed on the square and the sine signal, for both types of mother wavelet. The result of the CWT is presented in a scalogram. The more yellow the higher the magnitude of the frequency. When the Haar scalograms are compared to each other, it is seen that the spread of frequency for the sine signal (b) scalogram is larger than for the scalogram of the square signal (a). In (a) the frequency of 50 Hz is better observable than in (b). This is because the Haar wavelet better describes the square signal. The reverse can be said about the scalograms which used the Mexican hat wavelet, although here the effect is less prominent: (c) shows the scalogram of the square signal using a Mexican hat mother wavelet and (d) shows the scalogram of the sine signal using a Mexican hat mother wavelet. The magnitude of the 50 Hz is more pronounced in (d) than it does in (c).

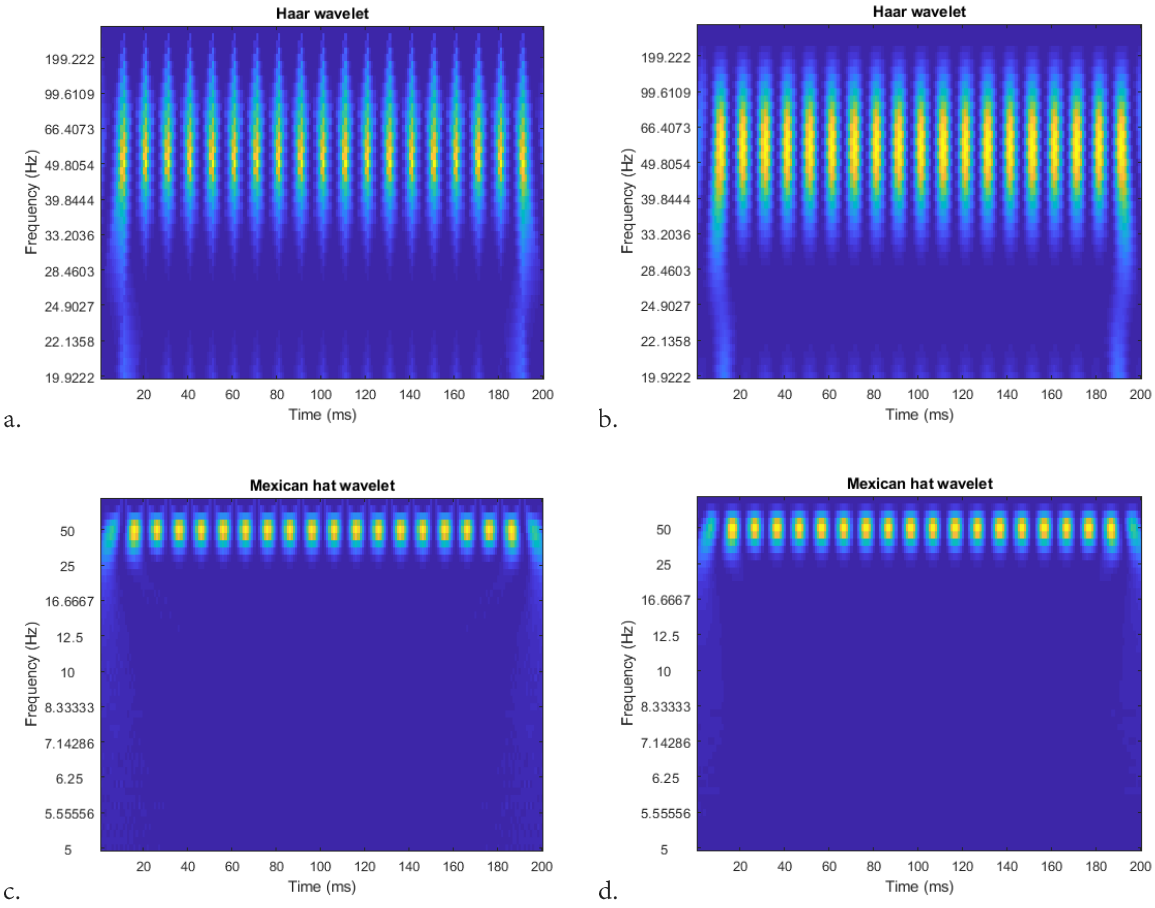

Fig. 3 Scalograms. a) Square signal with Haar wavelet; b) Sine signal with Haar wavelet; c) Square signal with Mexican hat wavelet; d) Sine signal with Mexican hat wavelet.

In Fig. 4 the FFT of the four signals is shown for each type of the signal (repeated, decaying and impulse). The first row of Fig. 4 shows that indeed a frequency of 50 Hz is found for the four signals. In the case of the square, triangular and the sawtooth signal, this frequency is aliased. The frequency of the sine signal is of course the clearest to see using FFT. In the second row, the effect of decay is introduced. This effect is more clearly shown in the FFT plot of the decaying sine signal. The 50 Hz frequency is still observed, but the transform method finds other frequencies as well, because of the less clear 50 Hz sinusoids (of non-constant amplitude) in the signal. In the last row the 50 Hz frequency cannot be detected anymore.

This is because of the impulse, which means that the remainder of the signal is zero. This is also taken into account when performing the FFT. Fig. 4 shows that FFT can find a certain frequency well, but not in the case of a transient signal.

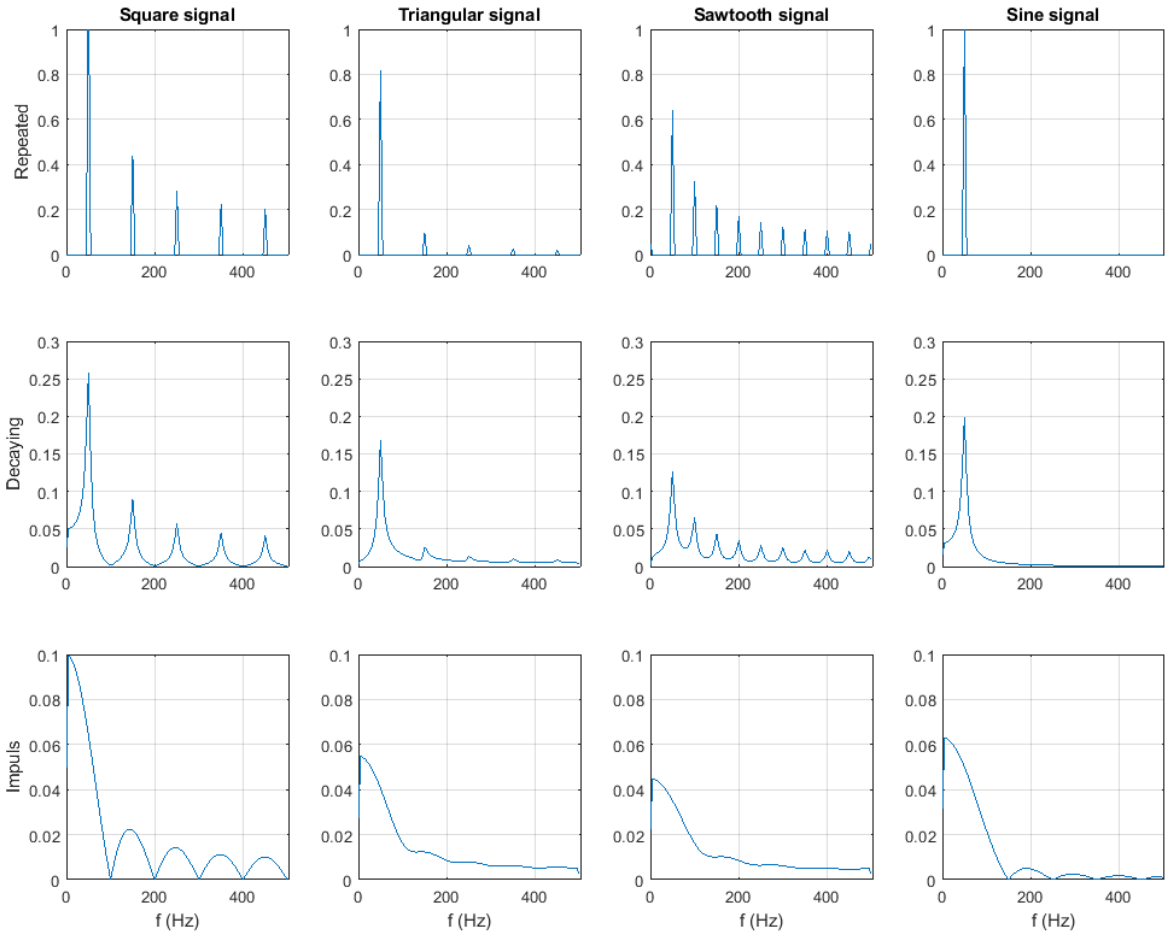

Fig. 4 Fast fourier transform

Fig. 5 shows the wavelet transform of the four signals in the columns. The standard wavelet for this MATLAB function, a morlet wavelet, was used. Now, the vertical axis shows the frequency domain. The 50 Hz frequency can be clearly observed in the first row for every signal. The CWT plot also shows the effect of the beginning and the ending of the signal. The sawtooth signal shows some other frequencies in lower resemblence with the daughter frequencies. This is probably caused by the chosen mother wavelet. The real effect of CWT with respect to FFT is shown in the performance of CWT on the decaying and impulse signals. In the second row the 50 Hz is still clearly observable, although this only happens during the first half of the signals time span. In the third row, the 50 Hz frequency is lost. There is not enough left of the signal to make a good estimate of the frequency of the impulse. That is why another method is discussed next.

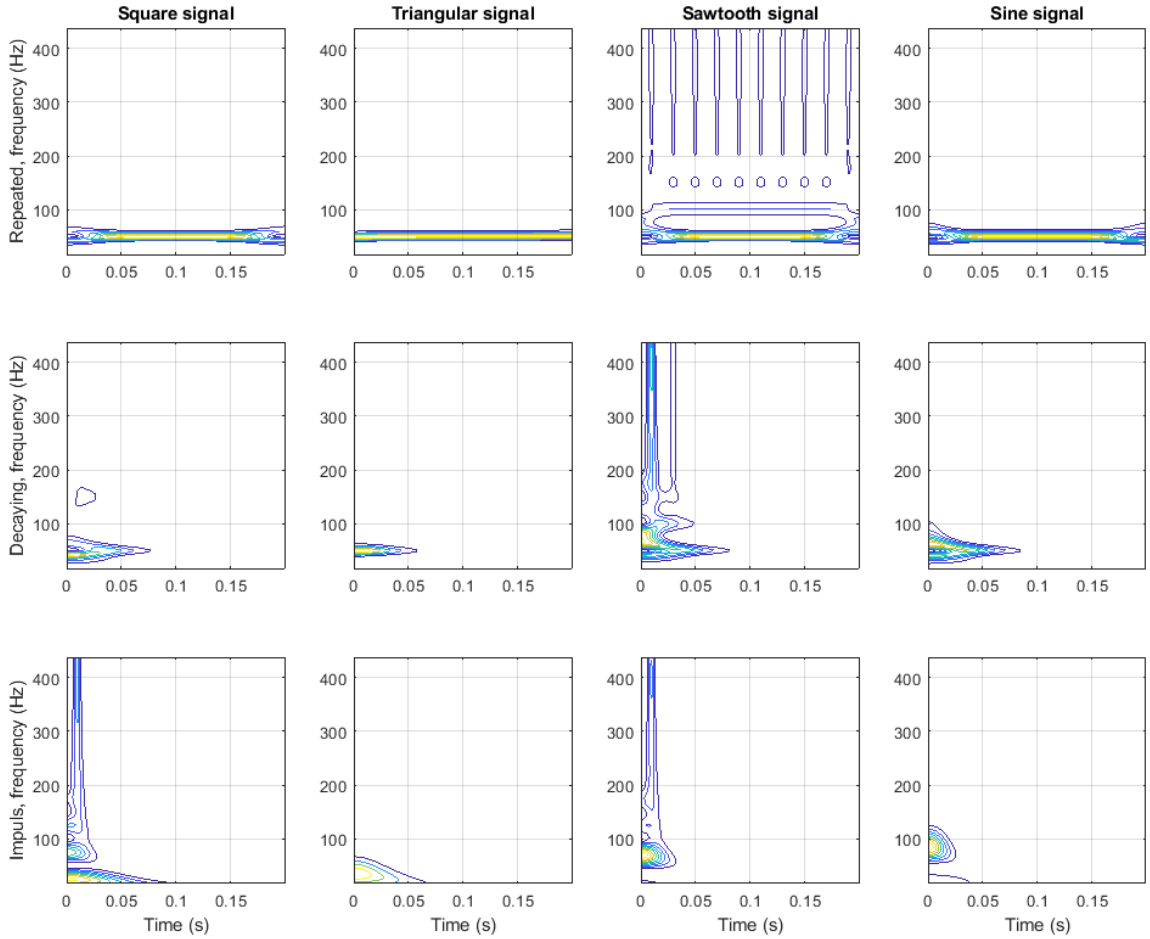

Fig. 5 Continuous wavelet transform

Hilbert transform

The Hilbert transform is related to the signal in such a way that the signal can be described with an amplitude and a phase: the *analytic signal* is computed first. The derivative of the phase results in the instantaneous frequency. Because of this property, HT is a good method to use on transient signals. Also, when dealing with a noisy signal, it is better to apply HT then FT. Another advantage of HT over FT is that it is not constrained by properties of the signal (stationarity and linearity are required for FFT). Instead, HT generates both amplitude and frequency information as a function of time. The generation of amplitude information is not shown in Fig. 5. The figure shows for each of the four signals the instantaneous frequency. In order to make recognition of the frequency easier to observe, the mean of the instantaneous frequency is plotted as well. In the first two rows, the mean is calculated over the whole time interval. But in the third row, the mean is only calculated over the part where the instantaneous frequency is not zero. The plots in the third row shows the difference in result with respect to the other two methods. Even though the impulse makes it harder to assess the frequency in the other two methods, HT shows an observable mean frequency of approximately 50 Hz.

It is interesting to note that the standard function, hilbert(), in MATLAB, used to calculate the 'analytic' signal of the signal, makes use of FFT. Essentially, the function performs both the FFT and the inverse FFT on the signal. The analytical signal contains the signal in the real part and the Hilbert transform in the imaginary part, which is a version of the original real sequence with a 90 degree phase shift.

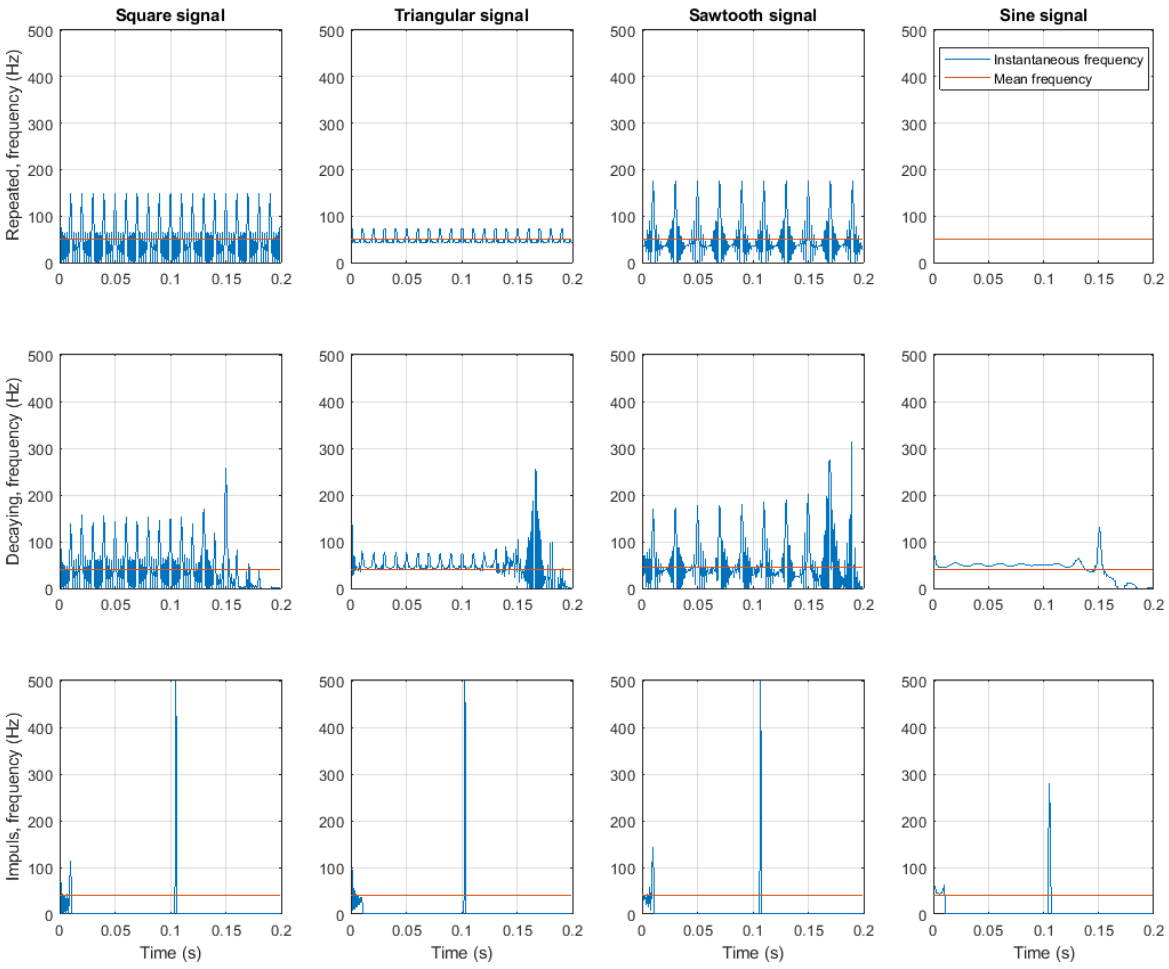

Fig. 6 Hilbert transform

Table 1 shows a comparison of the three signal identification methods discussed in this Appendix. The three methods are compared on five subjects.

Table 1 Comparison of the three signal identification methods

	Fast Fourier transform	Continuous wavelet transform	Hilbert transform
Frequency information	✓	✓	✓
Time information	✗	✓	✓
Suited for stationary signals	✓	✓	✓
Suited for transient signals	✗	✗/✓	✓
Computational time	✓	✓	✓

References

Fig. 2: https://en.wikipedia.org/wiki/Haar_wavelet
https://en.wikipedia.org/wiki/Mexican_hat_wavelet

M. Sifuzzaman, M.R. Islam & M.Z. Ali, *Application of Wavelet Transform and its Advantages Compared to Fourier Transform,* Journal of Physical Sciences, Vol. 13 (2009), p. 121-134

D. Donnelly, *The Fast Fourier and Hilbert-Huang Transforms: A Comparison,* International Journal of Computers, Communications and Control, Vol. I (2006), No. 4

Hilbert function matlab, https://nl.mathworks.com/help/signal/ref/hilbert.html

Appendix F

Calculation model

Three degrees of freedom external dynamics grounding model.

MathWorks Matlab & Simulink (R2017B)

a. Overview of the calculation model

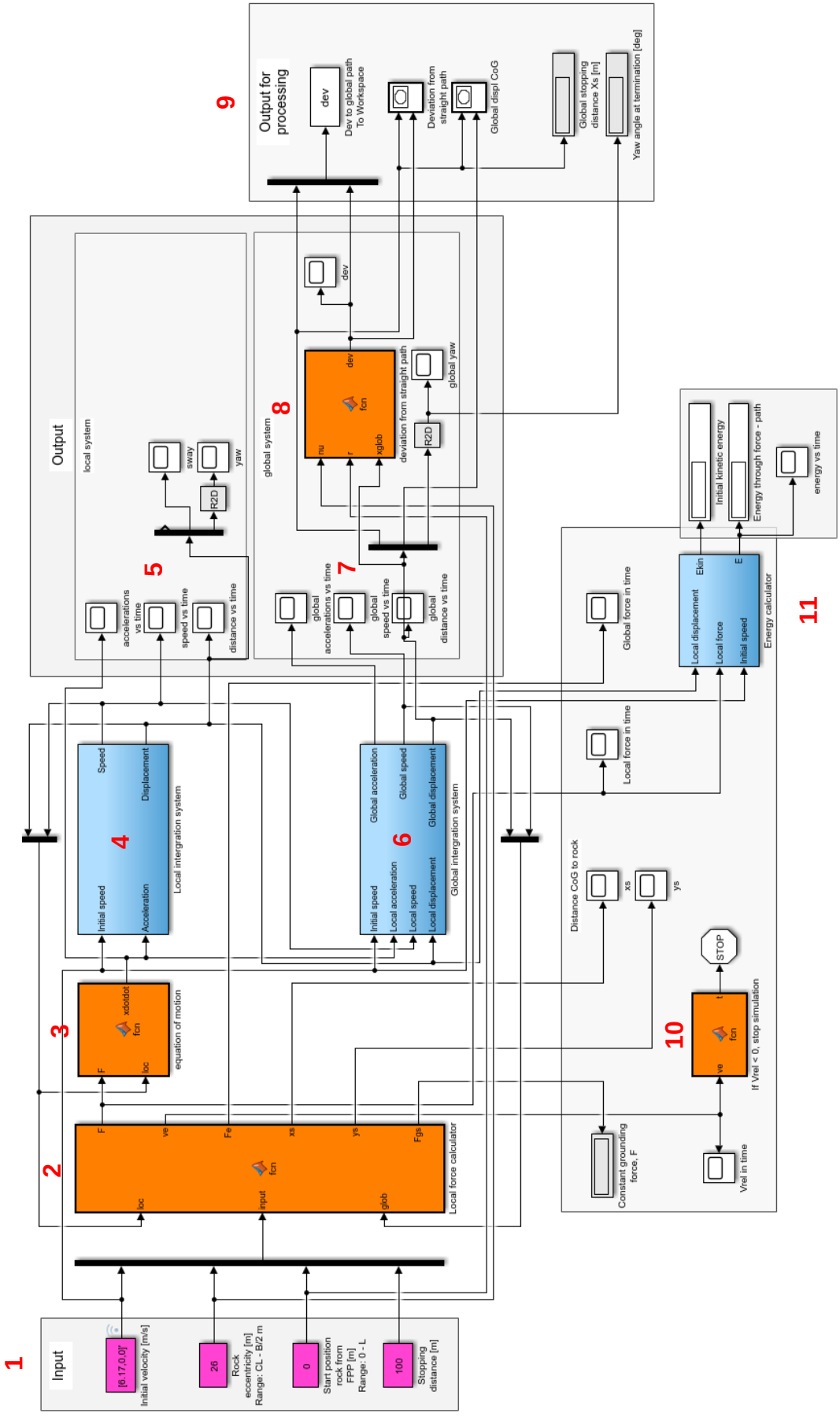

1 Here the input of the model is given: initial velocity of the ship. A vector containing: [initial velocity in surge, initial velocity in sway, initial yaw velocity].

2 The input is fed to the block *Local force calculator.* Together with information of the previous timestep (global and local velocity and displacement) the input is used to calculate the local forces acting on the ship bottom at the location of the ship's CoG. This information is ready to be used by the *equation of motion* block. The script in this block uses the methodology described in 4.1.2. Other output of this block includes the relative global velocity of the ship, the global forces, the distance of the rock to the ship's CoG (x and y data) and the constant grounding force which was used as input.

3 The equation of motion described in 4.1.2 is applied in this block. It takes the local forces and the local speed and velocity of the previous time step and calculates the local accelerations.

4 The *local integration system* block uses double time integration and the Ode45 solver and calculates both local velocity and displacement for the three DoF.

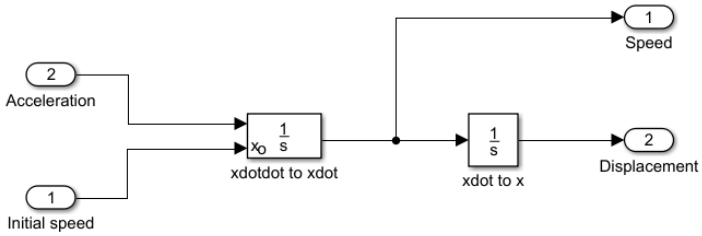

5 The *local integration system* yields three values as output: Acceleration, speed and displacement in surge, sway and yaw. Because the magnitude of displacement for the sway and yaw motion is much smaller than the displacement of the ship in surge, two scopes are used to look at the data more clearly individually.

6 In order to calculate the shape of the damage path along the ship bottom the global motion of the ship's CoG (around the rock) is necessary. This is calculated in the *global integration system* block. This is done by first transforming the local accelerations to the global reference frame. The transformation described in Equation 16 is used in the script. The integration is then performed the same way as in 4.

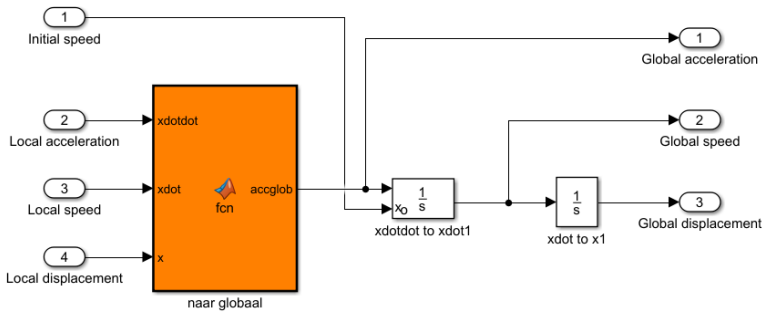

7 The *global integration system* yields three values as output: Acceleration, speed and displacement in surge, sway and yaw.

8 The shape of the damage path is calculated using trigonometry. The shape of the damage path is described by the deflection of a straight damage path parameter, δ, plotted against the length of the damage path in surge. It uses

the global displacement and heading of the ship's CoG and the first location of impact of the rock with the ship bottom.

9 Here acceleration data and damage path shape data is directed to Matlab's workspace, so that the data can be processed. Also, it includes two graphs. One plots this damage path shape data and the other plot's the movement of the ship's CoG (local frame) in the global frame. Also, the horizontal length of the damage path and the yaw angel both at termination of the simulation is displayed.

10 Using the stop command the simulation is terminated when the ship comes to a standstill (relative ship velocity reaches zero).

11 This block is used to calculate the kinetic energy from the initial velocity and the energy that goes into the rotation of the ship.

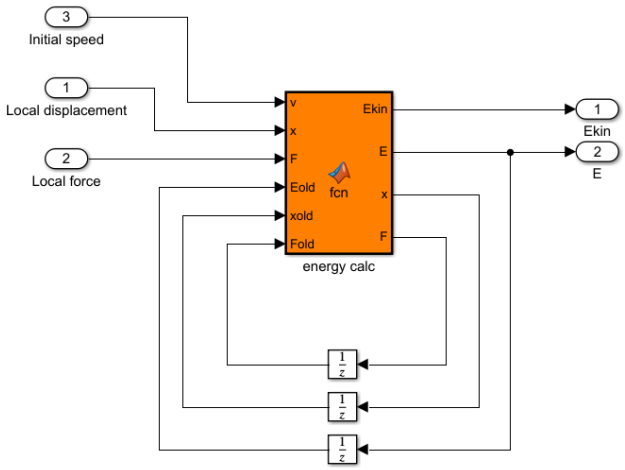

b. Overview inverse method Simulink model

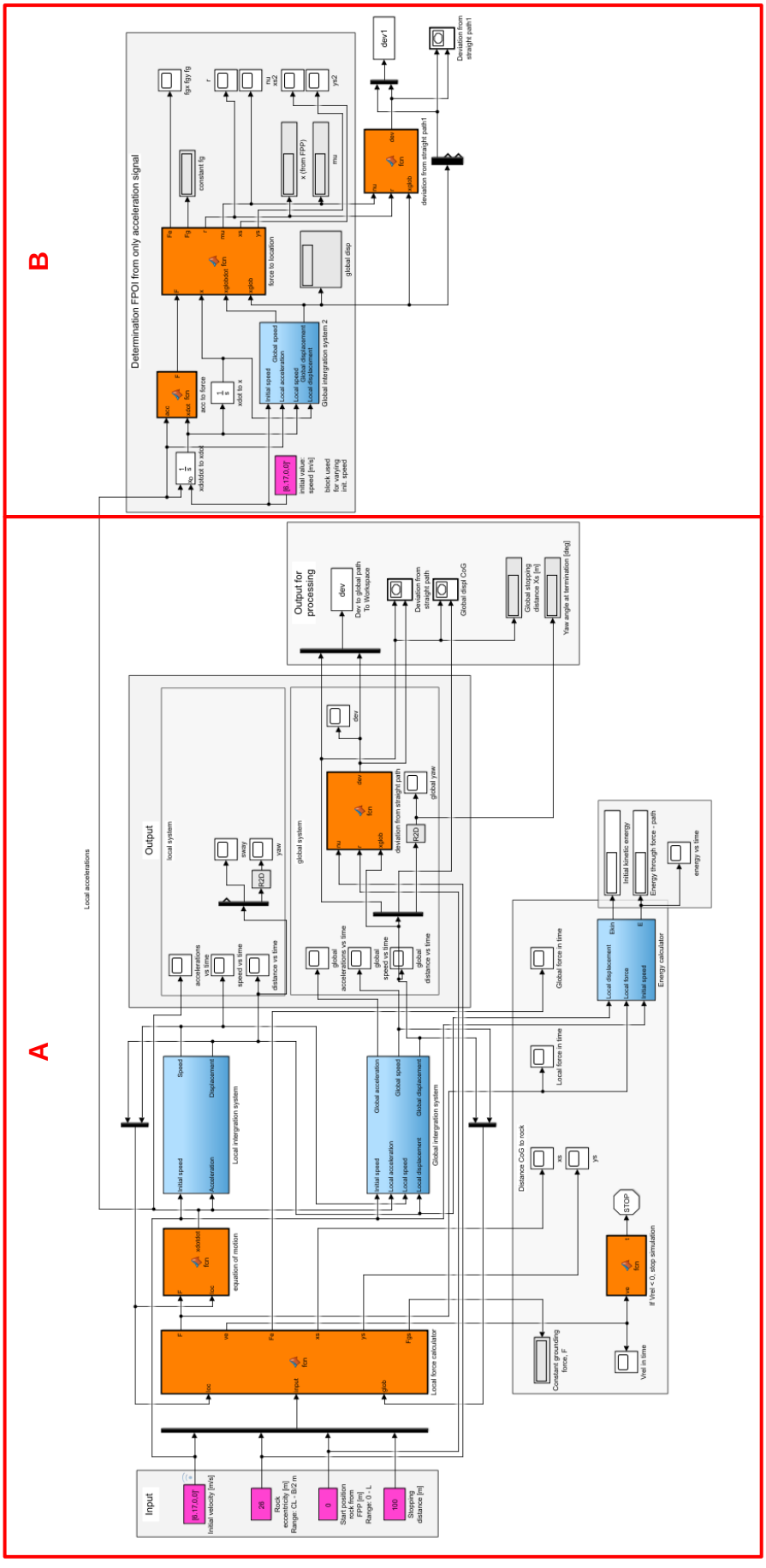

A Square A contains the calculation model as in a). The validation of the inverse method makes use of the local

B Square B contains the add-on of the calculation model: the inverse method for locating the damage path using only accelerations. A zoom-in of this part is given below.

c. Zoom-in on inverse method block

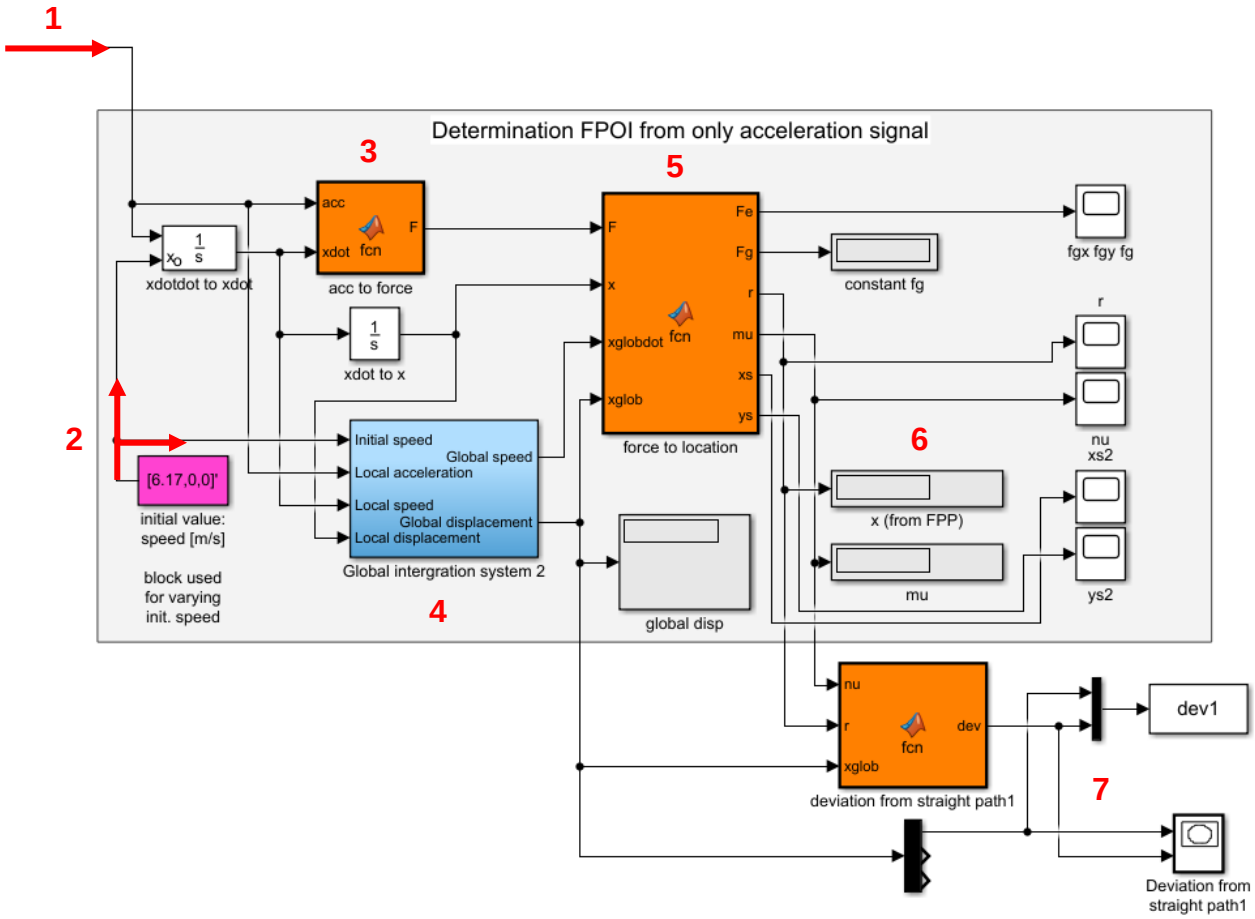

1 Local accelerations in surge (m/s^2), sway (m/s^2) and yaw (rad/s^2). As can be measured on board in CoG. These are one of the two input parameters.

2 Initial velocity of the ship in surge (m/s), sway (m/s) and yaw (rad/s). Used as initial condition for the integration block.

3 This block uses the equation of motion to calculate the external loads (grounding force) using the local accelerations and its first time integral. These local loads (acting on ship CoG) can be used for the next block.

4 This block is the same as in the calculation model in a), point 6. The local accelerations, velocities and displacements are transformed using Equation 16. The output needed is the global velocity and displacement. Because this tells something about the relative velocity and distance between CoG and rock.

5 In this block the local loads are used to calculate the path the rock followed on the ship bottom. The way this is allocated is described in paragraph 5.3. Output of this block is from top to bottom: the global loads (forces and moment at point of the rock), the constant grounding force F_G, the initial location of impact in x-direction from FPP, the initial rock eccentricity from CL μ (together these make the local coordinates of the FPOI), the global position of the ship's CoG in X-direction X_S and the global position of the ship's CoG in Y-direction Y_S.

6 These displays display the FPOI at any time. The allocation of the FPOI in 5 is iterative and therefore it varies in time.

7 This block is the same as in a), point 8. It uses the FPOI and the global displacement of the ship's CoG and calculates how the damage path deviates from a straight damage path with distance δ.

The calculation of the FPOI is summarized:

1	$\begin{Bmatrix} F_x \\ F_y \\ M_z \end{Bmatrix}_{ground}$	Use equation of motion to calculate local grounding forces and moment from input accelerations and initial velocity.
2	$\begin{Bmatrix} F_x \\ F_y \\ M_z \end{Bmatrix}_{ground} = \begin{Bmatrix} F_{G,X}\cos\psi + F_{G,Y}\sin\psi \\ -F_{G,X}\sin\psi + F_{G,Y}\cos\psi \\ F_{G,X}Y_s + F_{G,Y}X_s \end{Bmatrix}$	Grounding forces and moment in local coordinate system yields grounding forces in global system using this relation.
3	$\frac{V_{rel,y}}{V_{rel,x}} = \frac{F_{G,Y}}{F_{G,X}}$	The relation of the global grounding force to the relative velocity between rock and ship is used to estimate the orientation of these global grounding force components.
4	$V_{rel,X} = -\left(\dot{X}_S + Y_S\dot{\psi}\right)$ $V_{rel,y} = -\left(\dot{Y}_S + X_S\dot{\psi}\right)$	The relative velocity between rock and ship: $V_{rel} = V_{rock} - V_{ship} = -V_{ship}$. (Relative velocity is known from integration of the local accelerations).
5	$X_S = \frac{\dot{Y}_{glob} - \dot{X}_{glob}\frac{F_{G,Y}}{F_{G,X}} - M_z\dot{\psi}\frac{F_{G,Y}}{F_{G,X}^2}}{\dot{\psi}\left(1 + \frac{F_{G,Y}}{F_{G,X}}^2\right)}$	Now we obtain two unknowns and two equations: Y_S and X_S and formula M_z and the ratio $V_{rel} = F_G$.
6	$Y_S = \frac{M_z + F_{G,Y}X_S}{F_{G,X}}$	With X_S known, Y_S is solved next.
7	$r = L - LCG - (X_S + X_{glob})$ $\mu = Y_S - Y_{glob}$	The FPOI is then established with these relations. The method iteratively comes to this solution. r is the distance of first impact of the rock with the ship measured from FPP in X-direction. μ is the distance of first impact of the rock with the ship in Y-direction.

Appendix G

Application concept interface

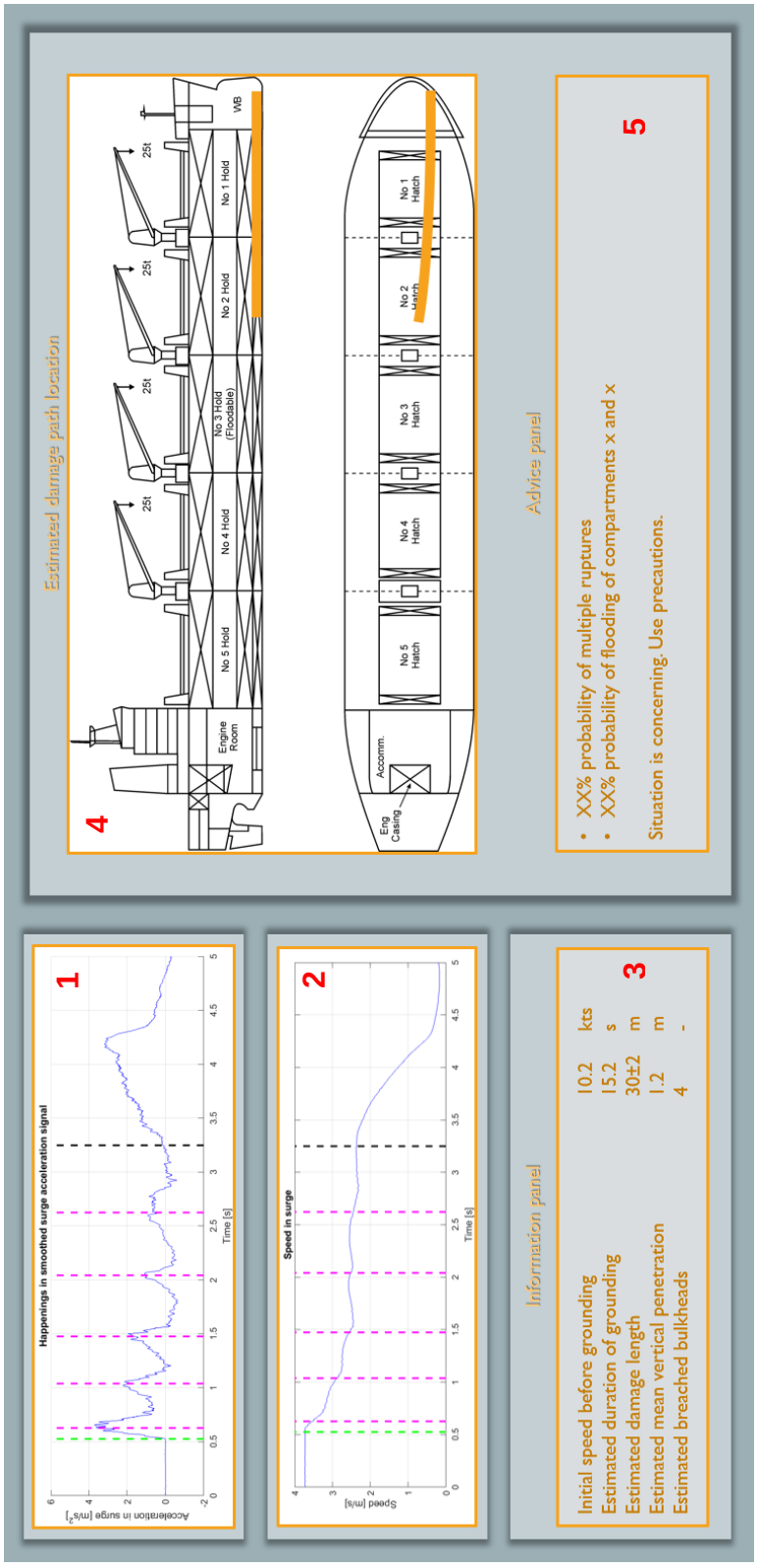

1 Display acceleration time-traces. Able to switch between signals in any direction. The tool indicates when the grounding started and ended. It also indicates when rupture is detected.

2 Display the speed. Able to switch between speed signal in any direction. It indicates the same moments in time as is detected from the acceleration signal.

3 General information panel. Gives information processed by the toolbox. It could display information on the estimated damage, vertical penetration, etc.

4 Displays a general lay-out of the ship. The lay-out shows for example the top and side view with a view of the ship structure. It shows for example the location of (watertight) compartments, the location of (watertight) bulkheads, tanks, location of engines, machinery and other essential equipment, pumps, etc. After a grounding incident the estimated damage path(s) is (are) plotted. This display could show which part of the structure is deformed, ruptured or weakened and it could show which compartment or tank is in danger of flooding.

5 Advice panel. The application could do a probability and risk analysis based on the obtained data and the information from 4. The panel could give information on the probability of a certain event. What is the probability that there may be flooding in one or more compartments? What is the probability if the inner shell is ruptured as well? The probabilities could be coupled with a risk analysis so that the application could assess the severity of the damage and of the situation. Based on this information it could inform the user on the nature of the situation (not immediately concerning, or mildly or very concerning) and advise him or her what to do in such a situation.